

Development of process control and material for micro/nano-scale electrohydrodynamic inkjet manufacturing

by

Xiao Zhang

A dissertation submitted to the graduate faculty
in partial fulfillment of the requirements for the degree of

DOCTOR OF PHILOSOPHY

Major: Industrial Engineering

Program of Study Committee:
Hantang Qin, Major Professor
Beiwen Li
Shan Jiang
Gül E. Okudan Kremer
Frank Peters
Michael Dorneich

The student author, whose presentation of the scholarship herein was approved by the program of study committee, is solely responsible for the content of this dissertation. The Graduate College will ensure this dissertation is globally accessible and will not permit alterations after a degree is conferred.

Iowa State University

Ames, Iowa

2021

Copyright © Xiao Zhang, 2021. All rights reserved.

DEDICATION

This dissertation is dedicated to my family and friends. My parents are always the inspiration and support to me throughout my life. I would like to thank my mom, Tianyin Cai, and my father, Weibai Zhang, for what they have done for me. I can't complete this dissertation without support from my family and friends.

TABLE OF CONTENTS

| | Page |
|-----------------------------------------------------------------------------------------------------------------------------------------------------------------------------------------------|-----------|
| LIST OF FIGURES | vi |
| LIST OF TABLES | x |
| NOMENCLATURE | xi |
| ACKNOWLEDGMENTS | xii |
| ABSTRACT | xiii |
| CHAPTER 1. GENERAL INTRODUCTION | 1 |
| Electrohydrodynamic inkjet printing | 4 |
| Motivation | 6 |
| Research objectives | 9 |
| Thesis organization | 10 |
| References | 11 |
| CHAPTER 2. LITERATURE REVIEW | 13 |
| Fabrication of functional devices for biomedical application | 13 |
| New material synthesis for fabricating micro/nanoscale shielding structure | 14 |
| In-situ monitoring system for electrohydrodynamic inkjet printing | 15 |
| Control of electrohydrodynamic inkjet printing process | 16 |
| References | 18 |
| CHAPTER 3. FABRICATION OF SILVER MICROSTRUCTURES VIA ELECTROHYDRODYNAMIC INKJET PRINTING AS CUSTOMIZATBLE X-RAY MARKER IN BIO-STRUCTURE FOR BIOMEDICAL DIAGNOSTIC IMAGING..... | 20 |
| Abstract..... | 20 |
| Introduction | 21 |
| Schematic of electrohydrodynamic inkjet printing & setup of X-ray imaging | 24 |
| Electrohydrodynamic inkjet (e-jet) printing..... | 24 |
| Material characterization of silver nanoink and microstructures | 26 |
| X-ray radiography imaging system | 27 |
| Results and discussion | 28 |
| Influence of printing parameters | 28 |
| X-ray imaging characterization and absorption analysis | 30 |
| Designed pattern fabrication and biomedical application | 33 |
| Conclusion | 37 |
| References | 38 |

| | |
|-----------------------------------------------------------------------------------------------------------------------------------------------------|-----|
| CHAPTER 4. FABRICATION OF MICRO-SCALE RADIATION SHIELDING STRUCTURES USING TUNGSTEN NANOINK THROUGH ELECTROHYDRODYNAMIC INKJET PRINTING | 42 |
| Abstract..... | 42 |
| Introduction | 43 |
| Methods and materials..... | 46 |
| E-jet printing system | 46 |
| Nanoink fabrication..... | 47 |
| Characterization..... | 47 |
| X-ray imaging of printed patterns | 48 |
| Results and discussion | 48 |
| Conclusion | 59 |
| References | 59 |
| CHAPTER 5. IN-SITU REAL-TIME CHARACTERIZATION OF MICRO-FILAMENTS FOR ELECTROHYDRODYNAMIC INK-JET PRINTING USING MACHINE VISION | 63 |
| Abstract..... | 63 |
| Introduction | 64 |
| Methodology..... | 67 |
| Machine vision theory | 67 |
| Experiment setup..... | 68 |
| Processing algorithm and results | 70 |
| Image analysis | 70 |
| Conclusion | 76 |
| References | 77 |
| CHAPTER 6. IN-SITU MONITORING OF ELECTROHYDRODYNAMIC INKJET PRINTING VIA SCALAR DIFFRACTION FOR PRINTED DROPLETS | 80 |
| Abstract..... | 80 |
| Introduction | 81 |
| Methodology..... | 84 |
| E-Jet printing setup..... | 84 |
| Scalar diffraction vision system | 86 |
| Image processing..... | 89 |
| Background analysis..... | 90 |
| Binarization and filtering..... | 91 |
| Cropping and combining | 92 |
| Circle finding..... | 94 |
| Results and discussion | 95 |
| Conclusion | 101 |
| References | 102 |

| | |
|--------------------------------------------------------------------------------------|-----|
| CHAPTER 7. DIMENSION PREDICTION OF ELECTROHYDRODYNAMIC INKJET PRINTED PATTERNS | 105 |
| Abstract..... | 105 |
| Introduction | 106 |
| Experiment setup | 109 |
| Mechanism of e-jet printing | 109 |
| Printing parameters and data collection | 110 |
| Experiment design..... | 111 |
| Statistical design..... | 113 |
| Results and discussion..... | 114 |
| E-jet printing results | 114 |
| Result of original data calculation..... | 117 |
| Result of fitted data | 118 |
| Multivariable e-jet printing supervision (MEPS) prediction model..... | 119 |
| Conclusion..... | 125 |
| References | 126 |
| CHAPTER 8. GENERAL CONCLUSION | 129 |
| General Conclusion | 129 |
| Future Work..... | 132 |

LIST OF FIGURES

| | Page |
|----------------------------------------------------------------------------------------------------------------------------------------------------------------------------------------------------------------------------------------------------------------------------------|------|
| Figure 1. Images of droplets generated by inkjet printing | 2 |
| Figure 2. Inkjet printing on the electronic board | 3 |
| Figure 3. (a) Images of glass microcapillary nozzle; (b) Nozzle and substrate configuration for printing; (c) Printer setup | 5 |
| Figure 4. Schematic of e-jet printing system | 13 |
| Figure 5. Microscope images and measurement of tungsten ink printed patterns on glass substrate | 15 |
| Figure 6. Feedback control framework | 16 |
| Figure 7. (a) Schematic of e-jet printing; (b) Nozzle and its reflection from the glass substrate; (c) Example of printed patterns; (d) Generated signal for printing | 26 |
| Figure 8. (a) XRD image of silver nanoink pattern and (b) SEM image of silver nanoink pattern (right) | 27 |
| Figure 9. (a) Schematic of X-ray imaging instrument; (b) Model of X-ray absorption; (c) X-ray imaging of printed single-layer silver line | 28 |
| Figure 10. Bulk silver function of grayscale <i>I/I</i> 0 with different thicknesses together with an X-ray image of those bulk silver | 31 |
| Figure 11. (a) 3D image of printed multi-layer silver patterns using nanoink; (b) X-ray imaging of multi-layer patterns from left to right: 1 layer, 10 layers, and 50 layers | 32 |
| Figure 12. (a) Spectacles pattern was printed on a glass substrate; (b) Spectacles pattern was printed with the higher voltage on a glass substrate; (c) Amplified microscope image of part of glass pattern; (d) Circuit pattern was printed on stretchable PET substrate | 34 |
| Figure 13. (a) Microscopic image of "feap" barcode fabricated by silver nanoink; (b) Binarized image of the fabricated barcode | 35 |
| Figure 14. (a) Print marker on leaf substrate (b) X-ray imaging of marker on leaf substrate | 35 |

| | |
|------------------------------------------------------------------------------------------------------------------------------------------------------------------------------------------------------------------------------------------------------------------------------------------------------------------------------------------------------------|----|
| Figure 15. (a) Print marker on leaf substrate under different voltage (b) X-ray image (c) Plotting of the greyscale value trend under the influence of different voltage values | 37 |
| Figure 16. (a) Schematic of e-jet printing. A high voltage is applied between the needle and plate electrode. (b) Voltage modality and a machine vision of e-jet printing process. (c) A typical circuit board partially covered by printed patterns for the radiation shielding concepts | 45 |
| Figure 17. Schematic of the lab-built X-ray imaging system | 48 |
| Figure 18. (a) Energy dispersive spectroscopy (EDS) and (b) Transmission electron microscopy (TEM) images of tungsten nanoparticles. (c) X-ray diffraction (XRD) results of printed tungsten dots..... | 49 |
| Figure 19. Printed tungsten dots with e-jet printing in different voltages. (a) Optical microscope image, (b) Dots area as a function of printing voltage..... | 50 |
| Figure 20. Optical microscope images of tungsten dots under different (a) Frequencies and (b) Pulse widths of high voltage; Optical microscope images of tungsten shaped lines with (c) Low and (d) Large magnification..... | 51 |
| Figure 21. Optical microscope images of tungsten patterns at different conditions: (a) DC voltage and the dashed lines were the designed pattern; (b) Large pulse width with AC voltage; (c) and (d) are non-fresh ink with normal and high voltage at the designed patterns as dashed lines in inset. The dashed lines denote designed printing path..... | 55 |
| Figure 22. (a) Optical image; (b) X-ray radiography image of printed tungsten lines with 20 layers (top) and 50 layers (bottom); (c) and (d) are magnified 2D and 3D images of the 50 layers tungsten line, respectively | 56 |
| Figure 23. Grayscale of bulk tungsten sheet as a function of its thickness. The inset is an X-ray radiography image of tungsten sheets with different layers..... | 56 |
| Figure 24. (a) Optical image of circuit board. (b) X-ray radiography image of the circuit board . (c) Printed capacitor and cover patterns on the circuit board under X-ray imaging..... | 58 |
| Figure 25. (a) Mechanism of image processing; (b) System setup; (c) Working condition; (d) Multi-layer printing; (e) Different orientations | 68 |
| Figure 26. (a) Typical image to be processed; (b) Binary image obtained using Otsu's method; (c) Edge image using Canny edge detector; (d) Typical cropped image; (e) Edge image using Canny edge detector | 70 |

| | |
|--------------------------------------------------------------------------------------------------------------------------------------------------------------------------------------------------------------------------------------------------------------------|----|
| Figure 27. Proposed algorithm for information extraction from images | 71 |
| Figure 28. (a) A typical edge image of the tilted filament; (b) Approximate edge image; (c) Diameter and tilt-angle calculations; (d) Piecewise approximate edge image..... | 71 |
| Figure 29. Representative images for different scenarios: (a) Normal printing (Scenario 1); (b) Change of filament dimensions (Scenario 2), (c) Tilted micro-filament (Scenario 3); (d) Multi-layer printing (Scenario 4) | 72 |
| Figure 30. Scenario 1-4: (a) Cropped grayscale image; (b) The mask; (c) Masked image; (d) Edge image | 73 |
| Figure 31. (a) Image of human hair; (b) The mask; (c) Masked image; (d) Edge image | 75 |
| Figure 32. (a) Schematic of e-jet printing, and (b) Printed droplet patterns | 85 |
| Figure 33. (a) Location of scalar diffraction system in e-jet printing setup, and (b) A schematic of the optical components for scalar diffraction: Laser, Step variable neutral density filter (ND), Sample, Lens-1, Lens-2, and Charge Coupled Device (CCD)..... | 86 |
| Figure 34. Intensity distribution resulting from the printed pattern in the (a) Fourier plane and (b) Image plane | 88 |
| Figure 35. (a) Singular background images with a unique disturbance (red circle) and several consistent disturbances (red square), and (b) Average of several background images | 90 |
| Figure 36. (a) The average background image described by Equation 1, (b) The sample image, and (c) The result of the subtractive process described by Equation 2..... | 91 |
| Figure 37. (a) Image binarization using a low sensitivity (0.05, assigned by the user) resulting in information loss, and (b) High sensitivity (0.55) resulting in the amplification of noise | 92 |
| Figure 38. (a) The full binarized image with the ROI identified, and (b) Full view of the ROI | 93 |
| Figure 39. (a) Combination of two ROI with its counterpart captured by (b) The microscope ... | 93 |
| Figure 40. The images with user defined circle sensitivity which was (a) Too low, and (b) Too high..... | 95 |
| Figure 41. (a) Radii comparison between the microscope and image processing algorithm, and (b) After normalization | 97 |

| | |
|---------------------------------------------------------------------------------------------------------------------------------------------------------------------------------------------------------------------------------------------------------------------------------------------------------------------------------------------------------------------------------------------|-----|
| Figure 42. Average value of (a) Binarization sensitivity (BS), and (b) Filter size (FS) comparison | 99 |
| Figure 43. Schematic of e-jet printing system setup: droplets were deposited onto the glass substrate by the electrical force | 110 |
| Figure 44. Chart of e-jet printing and data flow | 111 |
| Figure 45. E-jet printing of signal waveform..... | 115 |
| Figure 46. Leverage residual analysis considering the leverage of (a) Standoff distance, (b) Pulse width, (c) Voltage amplitude, (d) Frequency..... | 116 |
| Figure 47. Diameter mean plotting of different printing parameters: (a) Standoff distance at 52.5 μm , 61.25 μm , 70 μm , 78.75 μm (b) Pulse width at 200 μs , 250 μs , 300 μs , 350 μs , (c) Voltage amplitude at 600 V, 650 V, 700 V, 750 V, (d) Frequency at 20 Hz, 30 Hz, 40 Hz, 50 Hz..... | 118 |
| Figure 48. Least square mean plotting of different printing parameters: (a) Standoff distance at 52.5 μm , 61.25 μm , 70 μm , 78.75 μm (b) Pulse width at 200 μs , 250 μs , 300 μs , 350 μs , (c) Voltage amplitude at 600 V, 650 V, 700 V, 750 V, (d) Frequency at 20 Hz, 30 Hz, 40 Hz, 50 Hz..... | 119 |
| Figure 49. Interaction plot of pattern diameter versus different e-jet printing parameters..... | 121 |

LIST OF TABLES

| | Page |
|---------------------------------------------------------------------------------------------------------------------------------------------------------------------|------|
| Table 1. Specification of the e-jet printing process | 29 |
| Table 2. The comparison of grayscale between bulk and printed tungsten at the same thickness. | 57 |
| Table 3. Diameter and tilt-angle for scenarios 1-4 | 73 |
| Table 4. Different combinations of constants in imaging processing to test the scalar diffraction approach for identification of printed dot patterns | 96 |
| Table 5. Results of an even weight applied to the $\Delta\sigma$, $\Delta\mu$ and the number of “false alarms” for optimization of coefficients and constants..... | 98 |
| Table 6. E-jet printing parameters | 112 |
| Table 7. Effect of e-jet printing parameter on the dimension and the square value of the function..... | 121 |
| Table 8. Experiment and prediction data comparison | 123 |

NOMENCLATURE

| | |
|---------------|-----------------------------------------------------------|
| ND | step neutral density filter |
| f | focal length of the lens |
| d_0 | distance from the object to the lens center |
| d_i | distance from the lens to the resulting image |
| m_1, m_2, M | effective magnification of lens-1, lens-2, and the system |
| NA | numerical aperture of objective lens |
| R | resolution limit |
| λ | Wavelength of laser |
| $B(x, y)$ | average pixel intensity |
| $S(x, y)$ | individual pixels from light incident |
| $D(x, y)$ | resultant grayscale of sample pattern |
| FA | false alarms |
| $IPSD$ | image processing size distributions |
| $MMSD$ | microscope measured size distributions |
| μ, σ | average and standard deviation of distributions |

ACKNOWLEDGMENTS

I would like to thank my committee chair, Dr. Hantang Qin, and my committee members, Dr. Beiwen Li, Dr. Shan Jiang, Dr. Gül E. Okudan Kremer, Dr. Frank Peters, and Dr. Michael Dorneich, for their guidance and support throughout this research.

Besides, I would also like to thank my friends Sharon Lau, Eric David Weflen, Dr. Ali Baghersaghchi, Daniel Schimpf, Dr. Niechen Chen, Jakob Croghan, Cong Xu, colleagues Aditya-Rao Madhavaram, Prashant Ramkrishna Polampally, Sandeep Kumar Ravi Kumar, Benjamin Lies, Karthick Manikanda Gopalakrishnan Deivanai, Vignesh Suresh, Rahul Singh, Yiliang Chen, Bharath Melugiri-Shankaramurthy, Yi Zheng, Shaodong Wang, Yanhua Huang, Fei Liu, Xuepeng Jiang, Liangkui Jiang, Weijun Sheng, Jakob Hamilton, Samantha Sorondo, Li-Hsin Yeh, Kwangwoo Wi, Logan Beguhn, the department faculty Dr. Qing Li, Dr. Gilbert Stephen, Dr. Stone Richard, Dr. Helwig Michael, Dr. Mirka Gary, and staff Aaron Jordan, Janowicz Matthew, McDonough Deborah, Michael Renze, Kevin Brownfield, Krista Briely, and Fetty Nick for making my time at Iowa State University a wonderful experience. I want to thank Professor Xiaolei Shi from the Food Science department. I want to thank the visiting professor Dr. Hao Lyu. I want to thank Dr. Kejin Wang from the Civil department. I want to thank Dr. Zhan Zhang from the Center of Nondestructive Evaluation. I would also like to thank Dr. Iris Rivero for her support and guidance. I sincerely appreciate the support and help of Ai Shao. I want to also offer my appreciation to those who were willing to participate in my surveys and observations, without whom this thesis would not have been possible.

ABSTRACT

This dissertation introduced the development of material and control for electrohydrodynamic inkjet (e-jet) printing system. They include: 1) a method to fabricate functional devices; 2) a method to develop novel material for shielding radiation; 3) a method to monitor the e-jet printing process to reduce defects; 4) a method to predict the dimension of fabricated patterns.

Firstly, e-jet printing has been recognized as a novel micro/nano-scale direct writing manufacturing technique. Delicate patterns could be printed on various flexible substrates with conductive silver nanoink material. It is still a challenge to fabricate customized micro/nanoscale biomarkers for the application in biomedical area. Meanwhile, although the X-ray responses of bulk silver have been investigated, the characterization of silver nanoink is still unknown. Both delicate patterns and multi-layer samples were fabricated to demonstrate the robustness of fabricating the X-ray marker by e-jet printing. In this study, microstructures of silver nanoink were printed and characterized by X-ray. In the future, this effective e-jet printing method will enable the tracking of significant devices in the biomedical area such as customized drug delivery system.

Secondly, with the development of e-jet printing, more materials were explored to satisfy applications such as aerospace. Tungsten material has the capability of shielding massive X-ray. But there is no tungsten ink in the market for the fabrication of micro/nano-scale shield patterns. In aerospace, critical areas of electronics need to be protected to avoid radiation damage from space. Meanwhile, weight is one of the vital factors to be considered in this situation. Thus, it is required to develop a lightweight and effective shielding device to protect the electronics from

harmful X-ray radiation. The methods of synthesis and evaluation of new ink materials for e-jet printing system would be one of the most critical research areas in this field.

Thirdly, random defects could happen during the e-jet printing process due to the hardware system's limited performance and environmental factors. It is necessary to develop an in-situ monitoring system to detect the possible defects. Machine vision and laser scalar systems were proposed and established to monitor the printing process, and predict the dimension of printed patterns. These methods have proposed automated image processing algorithms to avoid the massive, time-consuming, and reliable measured data to monitor the e-jet printing process. It was demonstrated to be a robust and practical approach to contribute to the automation of the e-jet printing technique.

Fourthly, with the rapid evolvement of the e-jet printing system, it is required to understand the quantitative relationship between the e-jet printing parameters and the dimension of printed patterns. It has rarely been explored to print patterns by designed dimension without prior experiments. The statistical method was used and proposed for the design of experiments and the establishment of models to predict the dimension of printed patterns. This new method introduced a new perspective to predict the printing results instead of using the traditional simulation method. This research is a critical portion of the e-jet printing process when an automated e-jet printing system is used to fabricate high-resolution products in the industry's standard manufacturing.

In this dissertation, the-jet printing technique was further enhanced by establishing methods to develop new material, fabricate functional devices, monitor processes, and increase controllability. In the future, this micro/nanomanufacturing system will be used in the hybrid manufacturing system in the electronics, aerospace, and biomedical industries.

CHAPTER 1. GENERAL INTRODUCTION

Electrohydrodynamic inkjet (e-jet) printing has attracted the researcher's attention as a high-resolution micro/nano manufacturing approach to fabricate electronics on various flexible substrates. The tremendous potential application in biomedical, aerospace, and flexible electronics has been recognized by developing a growing number of high-performance materials. E-jet printing utilizes the electrical force to deposit conductive ink material on the substrate with a much smaller resolution than the glass capillary in a drop-on-demand manner. E-jet printing was proposed in the last ten years, which belongs to the category of inkjet printing. This technique's advantage over the traditional silicon-based manufacturing approach is a simple, low-cost, and flexible process. In 1951, the first practical Rayleigh break-up inkjet printing device was patented by Elmqvist of Siemens (Elmqvist 1951). The invention of this new manufacturing technology enables the deposition of ink material in a jetting manner. Although this manufacturing approach is practical for printing ink, the printing process's control is not promising. After that, Stanford University applied a pressure wave pattern to an orifice and realized the ink stream to break into droplets of uniform size and spacing (Sweet 1965). This pressure wave signal assisted the printing process in a controlled manner and resulted in fabricating high-quality patterns. However, the droplet formation process is still unknown. The droplet formation by inkjet printing was discussed and analyzed (De Gans 2004). The high-speed camera was used in our lab to capture the droplet formation process. In Figure 1, the ink started to detach from the nozzle under the electrical force. The detached ink started to generate a spherical droplet and finally deposited it on the substrate. Meanwhile, various inkjet printing technologies are based on different mechanisms to deposit droplets of ink on the substrate and form a specific pattern.

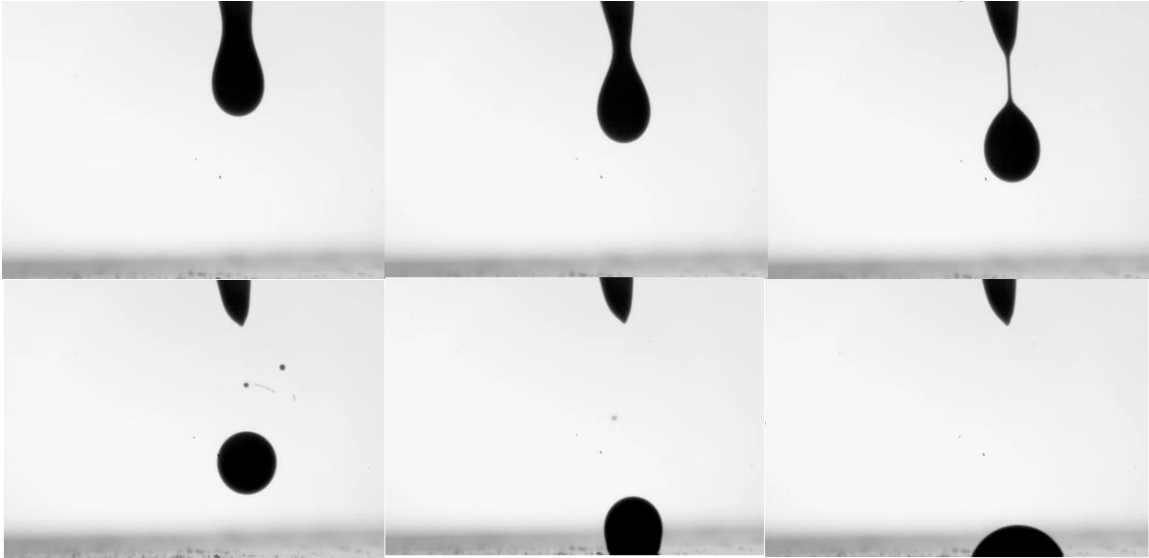


Figure 1. Images of droplets generated by inkjet printing

While continuous inkjet printing was evolving rapidly, drop-on-demand inkjet printing started attracting attention in this field. A drop-on-demand device will enable the ink to deposit on the substrate under control such that the fabrication process could happen in designed places at expected time slots. Zoltan, Kyser, and Sears have contributed to initiating drop-on-demand printers' applications (Zoltan 1974; Kyser & Sears 1976). These commercialized printers can print in a highly controlled way. The representative products of the early drop-on-demand inkjet printing systems are PT-80 serial printers from Siemens. These printers ejected the ink by the mechanical movement of the piezoelectric ceramic. With these drop-on-demand printers' development, higher requirements were proposed to address the increasing challenge regarding printer head geometry. The geometry of the piezoelectric printhead was discussed (De Jong 2006). The ink reservoir can maintain a low level of ambient pressure to prevent the ink from ejecting out of the nozzle. When the voltage signal is applied to the piezo-element, it will increase and reduce the ink channel's volume. Finally, the printer could push and hold the ink to be deposited on the substrate.

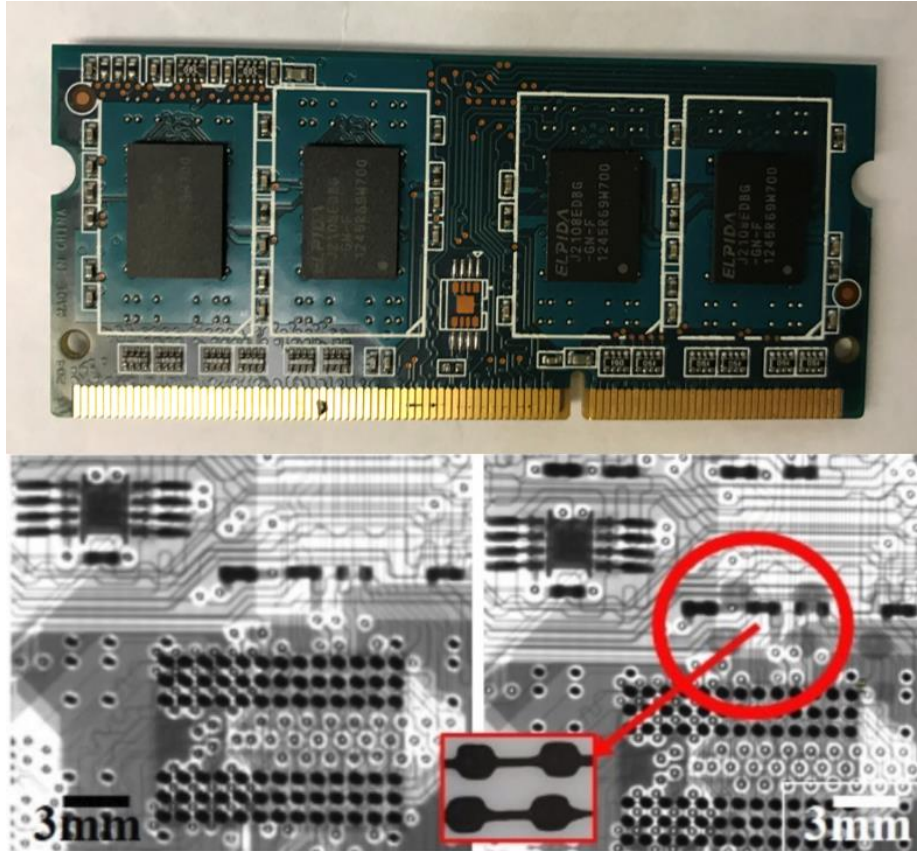


Figure 2. Inkjet printing on the electronic board

New forms of drop-on-demand printing were proposed based on different mechanisms of jetting the ink. Bubble jet printing was among these new types of drop-on-demand inkjet printing techniques. The vapor bubble is generated by rapid heating of ink in nozzles; the ink droplets is then ejected by the produced high pressure (Hara 1982). After that, more and more companies started to work on this type of printer. Canon, Xerox, Asahi Glass, Arkwright, Folex, 3M, and Imation represented the typical inkjet printing techniques in this area in late 1990 (Hue 1998).

Later on, inkjet printing started to expand in broader application areas with the development of newly recognized materials for resolving challenges in various research fields. Inkjet printing was a powerful tool in a broader range of fields such as structural ceramic, polymer electronics, protein chips, and functional material (Rirringhaus 2003). For example,

inkjet printing was used to print cells and biomaterials to allow organ printing in the laboratory (Boland 2006; Roth 2004). Inkjet was demonstrated to be helpful to address challenges in biomedical areas. Meanwhile, the electronic packaging industry has demonstrated inkjet printing technology for flexible production (Mantysalo 2007). For example, in Figure 2, the synthesized ink material was printed on a flexible substrate (transparent plastic) and used to shield the critical areas of electronics from possible severe radiation in the aerospace. The X-ray image has shown the excellent shielding performance of the printed tungsten patterns.

Electrohydrodynamic inkjet printing

E-jet printing is a high-resolution, low-cost, and flexible micro/nano-scale fabrication technique. E-jet printing uses electrical force to deposit ink, generating a resolution much smaller than the capillary glass nozzle. Over the last ten years, it has been evolving rapidly to address challenges ranging from aerospace, biomedical to electronics areas. The increasing demand for device application in electronics, biotechnology, and microelectromechanical systems proposed higher requirements for inkjet printing and resulted in the development of electrohydrodynamic inkjet printing (Park 2007). Normally e-jet printing stores the metal ink in a nozzle and ejects it through a glass capillary. In Figure 3, the ink was shown in the glass capillary. The glass capillary was manufactured in the lab. As shown in Figure 3(b), a voltage was applied between the glass capillary and substrate; the ink is dragged by electrical force and deposited on the substrate to form a uniform line pattern that is much smaller than the nozzle diameter. Figure 3(c) shows that sometimes an air pump will be used to provide gas pressure and eject ink together with the electric force. With a controlled electrical field and planned tool path, intricate conductive patterns were fabricated by the e-jet printing technique. The stage movement has a microscale resolution during the printing process. Different substrates could be used for e-jet printing, such as glass substrate, PET, and bio-tissue substrates. E-jet printing has provided a

flexible and direct-writing method to fabricate electronics on various substrates compared with the traditional silicon-based substrate. The development of alternating current (AC) in e-jet printing is a milestone for improving the printing quality. It was found that remained charged influenced the electrical field and interrupted the flow behavior of droplets. In 2014, ac-pulse modulated e-jet printing was proposed by North Carolina State University (Wei 2014). The positively charged droplets and negatively charged droplets are neutralized during the printing process, which lowers deposited droplets' instability.

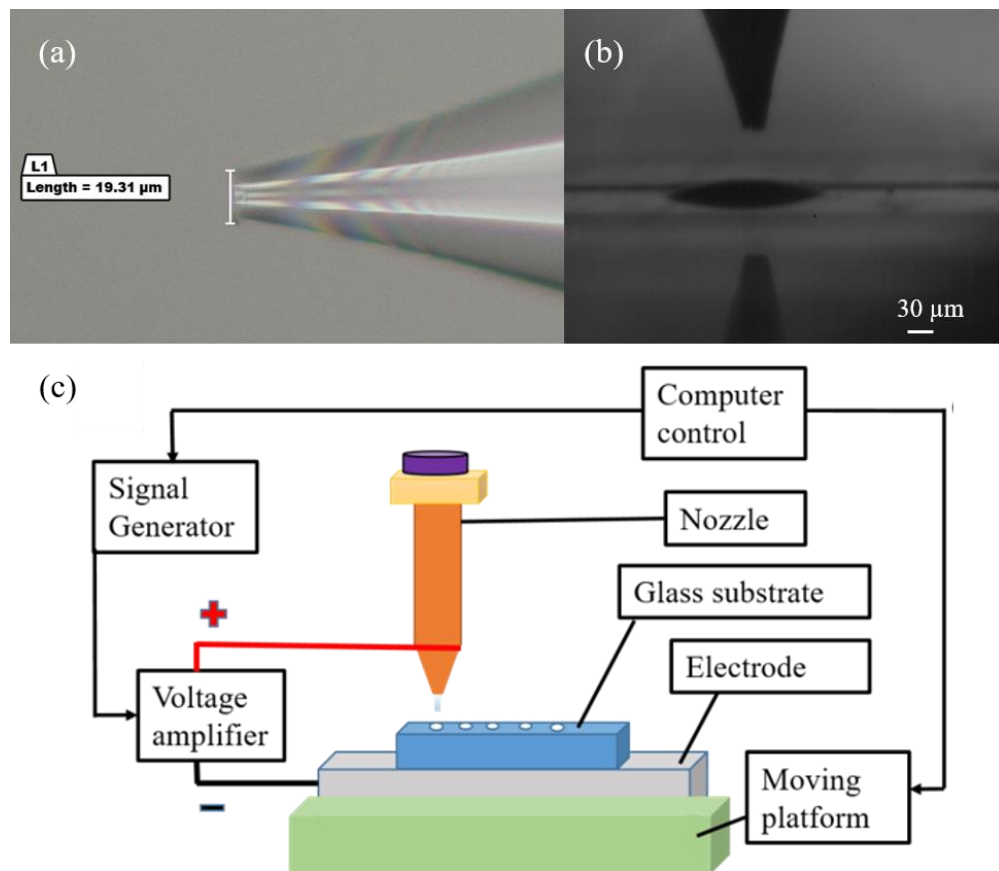


Figure 3. (a) Images of glass microcapillary nozzle; (b) Nozzle and substrate configuration for printing; (c) Printer setup

In e-jet printing, printed patterns are controlled and influenced by various printing and environmental factors. For example, the printing process was controlled by pulse frequency,

pulse width, voltage amplitude, plotting speed, and standoff distance. Pulse frequency is the number of the input signal to eject the ink in a unit of time. Pulse width is the time in one cycle. The voltage amplitude is the voltage that ejects the ink. Plotting speed is the movement speed of the platform. The standoff distance is the distance between the tip of the glass capillary and the substrate. Other environmental factors influence the e-jet printing process, such as the dust in the air, the nozzle's morphology, electrode shape, and human operation. E-jet printing was demonstrated to have enormous potential in fabricating electronics. For example, in North Carolina State University, a multi-layer capacitive touch sensor was fabricated on polyethylene terephthalate (PET) film. The metal ink was used to fabricate the touch sensor on a flexible substrate with a resolution of sub-20 μm (Qin 2017). Electrohydrodynamic inkjet printing is a high-resolution, low-cost, and flexible manufacturing approach. The promising future of fabricating electronics attracted the researcher's attention to developing e-jet printing as an option to address challenges in aerospace, biomedical, and electronic industries. Moreover, it can be developed as a hybrid micro/nano-scale manufacturing approach to revolutionize the traditional manufacturing industry.

Motivation

The e-jet printing could easily deposit nanoink materials on various substrates to fabricate delicate micro/nano-level resolution structures. These advantages enable the development of functional new materials for resolving challenges in different areas such as aerospace, biomedical, and electronic industries. However, sometimes it is required to synthesis new material to resolve problems considering the purpose of the research. Secondly, real-time monitoring methods such as machine vision and laser scalar approach could be developed to notify the possible defects during the printing process. Finally, once a defect is located or the

variation in the dimension of printed patterns is detected, the e-jet printing system will reverse the trend by knowing how printing parameters could influence the printing results.

The biomarker is used in biomedical research for tracking the position of marked devices for analysis. It is a problem to fabricate micro/nano-scale and flexible biomarkers for biomedical diagnosis. In this study, the silver nanoink was used to fabricate the biomarker by e-jet printing with an X-ray radiation instrument's assistance. The e-jet printing could easily drag the ink material and deposit various substrates to fabricate functional devices with the electrical field. However, the X-ray characterization of silver nanoink microstructures needs to be investigated to realize the tracking of silver nanoink marked devices such as drug release tablets. Thus, the X-ray characterization of silver nanoink has to be demonstrated. Functional patterns such as barcodes need to be fabricated and demonstrated to mark the device. The e-jet printed samples shall be characterized by X-ray for tracking purposes. In the future, e-jet printing could contribute to image diagnosis by fabricating micro/nano-scale microstructures on a wide range of flexible substrates in the biomedical area.

In aerospace, there is massive harmful radiation that could damage electronics in the spaceship. Tungsten material is a good solution for the protection of these electronics. However, it is known that bulk tungsten is difficult to be machined or processed by chemical reactions. It is necessary to develop a lightweight and practical device to shield the aerospace's critical electronics from damaged. The synthesis of tungsten nanoink material could fill the gap and meet the requirement. The printability has to be demonstrated by e-jet printing experiments. The X-ray characterization of printed tungsten patterns and commercial bulk tungsten experiment has to be conducted to verify the shielding efficiency. In the future, the synthesized tungsten nanoink

will contribute to the manufacturing of shielding micro structures for shielding key electronics in aerospace with extremely low weight.

Although e-jet printing has presented enormous application potential in biomedical and aerospace areas, there are still random defects during the printing process. It is necessary to develop real-time monitoring systems for the e-jet printing system. Machine vision and laser scalar are two practical approaches to conduct the monitoring process. The image processing could reduce the size of collected information during the e-jet printing process. The droplet leaves the capillary nozzle and forms the filament between the nozzle and substrate. The filament shall be uniform during the printing process when the printing parameters are constant. The dimension information has to be processed and delivered back to a central computer for processing the detected defects. Meanwhile, it is necessary to remove the substrate's printed patterns to measure the dimension after e-jet printing. A designed laser scalar system could collect images and analyze the dimension in real-time. The development of an in-situ monitoring system could support observing defects and calculating the dimension in real-time. Still, it could also contribute to establishing a digital twin system for the optimization of the e-jet printing process nondestructive evaluation of printed samples.

With the assistance of a monitoring system, both defects and dimensions could be observed during the e-jet printing process. However, once an abnormal situation (variation in the diameter of filament or difference in the dimension of printed patterns) is detected, it is required to reverse the trend by calibrating printing parameters. In sum, there are two general approaches to predict the dimension: finite element simulation and statistical analysis. The statistical analysis methods could be an ideal approach to understand how printing parameters could influence the e-jet printed patterns. The relationship between the printing parameters and the

dimension of printed patterns needs to be established and predicted. The precise control of printed patterns using printing parameters and a reliable real-time monitoring system will contribute to a highly reliable and automated micro/nano-scale e-jet printing system.

Research objectives

The requirement of using e-jet printing to address challenges in the aerospace, biomedical, and electronic area has proposed the necessity of developing new nanoink materials, in-situ monitoring systems, and control methods. This dissertation has focused on developing new approaches to address these challenges.

In sum, there are several objectives in this research, as summarized below:

(1) Develop the fabrication process and characterize biomedical devices for electrohydrodynamic inkjet printing.

Fabrication of functional devices in the biomedical area, such as biomarker, would require high-resolution and flexible control during the manufacturing process. A method needs to be developed to fabricate complex patterns such as the X-ray makers. A method needs to be proposed to characterize the X-ray responses of silver nanoink e-jet printed microstructures.

(2) Synthesis of new material for electrohydrodynamic inkjet printing to resolve radiation challenges in aerospace.

There is numerous radiation in aerospace, which could damage the electronics in the aerospace. Tungsten material could effectively absorb the radiography, but it is not easy to manufacture the bulk tungsten device. Thus a method has to be proposed to synthesize tungsten nanoink to fabricate micro/nano-scale structures for protecting the key electronics in the spaceship.

(3) Establish the machine vision system to provide *in-situ* monitoring for the electrohydrodynamic inkjet printing process.

The filament generates between the capillary nozzle and conductive substrate. The variation of the filament size could happen while a defect occurs. It is also required to reduce the size of collected images and reflect the filament information. Thus an image processing method needs to be proposed to monitor and calculate the filament diameter during the electrohydrodynamic inkjet printing process.

(4) Propose the laser scalar system to observe the dimension of electrohydrodynamic printed patterns in real-time.

Usually, the printed patterns need to be removed from the platform during the e-jet printing process to observe the dimension information. A laser scalar system needs to be designed and proposed to monitor the process and calculate the dimension with the image analysis algorithm.

(5) Predict the dimension of the electrohydrodynamic inkjet printed patterns with the proposed statistical model.

Even though an abnormal situation could be realized and reported to the central computer during the e-jet printing process, it is still unknown for the relationship between the printing parameters and dimension of printed patterns. A statistical method needs to be proposed to predict and validate the quantitative model.

Thesis organization

In Chapter 1, a general introduction about inkjet printing and e-jet printing, followed by the research motivation and objective description is presented. In Chapter 2, the literature review about the electrohydrodynamic inkjet printing process is presented. In Chapter 3, a method to fabricate and characterize biomedical devices is presented in a journal publication format. In

Chapter 4, a method to synthesis tungsten nanoink and fabricate radiation shielding devices is presented in a journal publication format. In Chapter 5, a machine vision system is introduced to capture the filament size in electrohydrodynamic inkjet printing in a journal publication format. In Chapter 6, the laser scalar system is established to monitor the printed patterns during the electrohydrodynamic inkjet printing process in a journal publication format. In Chapter 7, a prediction model is established based on electrohydrodynamic inkjet printing in a journal publication format. In Chapter 8, the summary and future work of the study in this dissertation is provided.

References

- Boland, T., Xu, T., Damon, B. & Cui, X., 2006. Application of inkjet printing to tissue engineering. *Biotechnology Journal: Healthcare Nutrition Technology*, 1(9): pp. 910-917.
- De Gans, B. J., Duineveld, P. C. & Schubert, U. S., 2004. Inkjet printing of polymers: state of the art and future developments. *Advanced materials*, 16(3), pp. 203-213.
- De Jong, J., De Bruin, G., Reinten, H., Van Den Berg, M., Wijshoff, H., Versluis, M. & Lohse, D., 2006. Air entrapment in piezo-driven inkjet printheads. *The Journal of the Acoustical Society of America*, 120(3): pp. 1257-1265.
- Elmqvist, R., Measuring instrument of the recording type, U.S. Patent 2566443.
- Hara, T. & Endo, I., 1982. Bubble Jet Recording. *J. Inst. Image Electron. Engrs. Jpn*, 11, pp. 66-71.
- Kyser, E. L. & Sears, S. B., 1976. Method and apparatus for recording with writing fluids and drop projection means therefore, U.S. Patent 3946398.
- Le, H. P., 1998. Progress and trends in ink-jet printing technology. *Journal of Imaging Science and Technology*, 42(1): pp. 49-62.
- Mantysalo, M., Mansikkamaki, P., Miettinen, J., Kaija, K., Pienimaa, S., Ronkka, R., Hashizume, K., Kamigori, A., Matsuba, Y., Oyama, K. & Terada, N., 2007. Evaluation of inkjet technology for electronic packaging and system integration. *Proceedings 57th Electronic Components and Technology Conference*, pp. 89-94.
- Park, J. U., Hardy, M., Kang, S. J., Barton, K., Adair, K., Kishore Mukhopadhyay, D., Lee, C. Y., Strano, M. S., Alleyne, A. G., Georgiadis, J. G. & Ferreira, P. M., 2007. High-resolution electrohydrodynamic jet printing. *Nature materials*, 6(10): pp. 782-789.

- Qin, H., Cai, Y., Dong, J. & Lee, Y. S., 2017. Direct printing of capacitive touch sensors on flexible substrates by additive E-jet printing with silver nanoinks. *Journal of Manufacturing Science and Engineering*, 139(3).
- Roth, E. A., Xu, T., Das, M., Gregory, C., Hickman, J. J. & Boland, T., 2004. Inkjet printing for high-throughput cell patterning. *Biomaterials*, 25(17): pp. 3707-3715.
- Sirringhaus, H. & Shimoda, T., 2003. Inkjet printing of functional materials. *MRS bulletin*, 28(11): pp. 802-806.
- Sweet, R. G., 1965. High frequency recording with electrostatically deflected ink-jets. *Rev. Sci. Instrum*, 36, pp. 131.
- Wei, C., Qin, H., Ramirez-Iglesias, N. A., Chiu, C. P., Lee, Y. S. & Dong, J., 2014. High-resolution ac-pulse modulated electrohydrodynamic jet printing on highly insulating substrates. *Journal of Micromechanics and Microengineering*, 24(4): pp. 045010.
- Zoltan, S. L., 1974. Pulse droplet ejection system, U.S. Patent 3683212.

CHAPTER 2. LITERATURE REVIEW

Fabrication of functional devices for biomedical application

Electrohydrodynamic inkjet printing is a high-resolution, low-cost, flexible, and direct-write technique. It is shown that the e-jet printing system consists of gas supply, voltage supply, translation stage, substrate, ink chamber, and computer control subsystems (Barton 2010). The gas supply is a supplementary approach to eject the ink for e-jet printing. The amount of ejected material is controlled by the pressure regulator. The ink is prepared in the ink chamber. The ink will be stored in the chamber if there is either no air pressure or electrical force. The gas pressure or electrical force will eject the ink out. The extracted material will be deposited on the prepared substrate. The substrate is usually a reflective and flat surface object such as glass slides. The movement of the X/Y/Z stage determined the formation and morphology of printed patterns. The schematic of e-jet printing is shown in Figure 4.

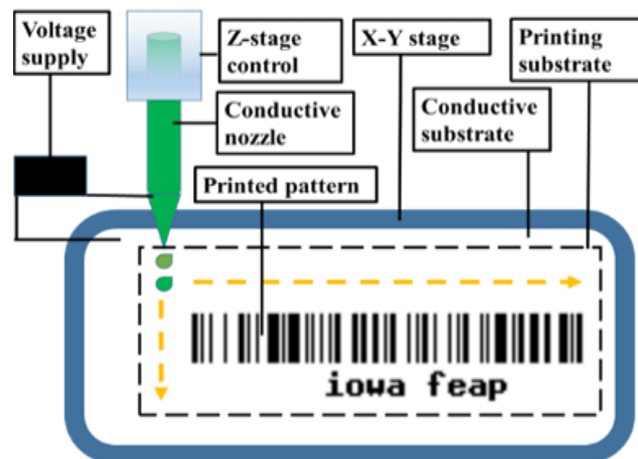


Figure 4. Schematic of e-jet printing system

Ink printing ejects solve ink material onto the substrate and forms 2D or 3D structures. Schwann cells were mixed with alginate solvent. The cells were then ejected inside the scaffold for peripheral nerve tissue regeneration (Ghilan 2020). Inspired by the bioink application in

tissue regeneration, bioelectronics was designed and fabricated by the e-jet printing technique. The flexible, thin-film nitric oxide sensor was fabricated to monitor macrophage depolarization events (Ryan 2019). In the research field of cancer, e-jet printing was used to fabricate implantable magnetocaloric mats. This device was developed as a cancer treatment approach by providing heat for localized hyperthermia cancer therapy (Yang 2017). Meanwhile, e-jet printed scaffold is one of the critical biomedical application areas. High-resolution 3D polymeric scaffolds were fabricated by the e-jet printing technique for tissue engineering (Wei 2013).

Meanwhile, the fabrication of biomarker by e-jet printing received limited attention. In the biomedical system, a marker needs to enable the communication between the implanted device and the external instrument (Boute 1986). In this dissertation, the silver nanoink was e-jet printed as a biomarker. It was detected and recognized by an X-ray radiation instrument. Although there existed the research of X-ray characterization of bulk silver (Barrie 1976), it is still necessary to study the X-ray response of silver nanoink printed microstructures. The fabrication on bio-substrate by e-jet printing also needs to be further explored to demonstrate this novel manufacturing approach's robustness and feasibility.

New material synthesis for fabricating micro/nanoscale shielding structure

Bioink material supports the development of biomedical applications. The development of new ink material strengthens e-jet printing as an alternative micro/nanomanufacturing technique. In aerospace, critical portions of electronics can be damaged by overexposure to radiation. Tungsten material has been evaluated as a useful shielding material in many areas such as the nuclear medicine field. It was found to have a high potential to replace lead as new radiation shielding material (Kobayashi, 1997). The tungsten has shown the outstanding performance of shielding material such as chemical and physical durability. However, it is difficult to manufacture this material into designed morphology.

The synthesis of tungsten ink is an option for the micro/nanoscale manufacturing of shielding structures for the protection purpose of aerospace electronics. Although there are tungsten oxide inks such as WO₃ in inkjet printing (Vidmar 2014), tungsten powder ink does not appear in the current research field. In the successful fabrication of tungsten oxide on PET/ITO substrate inspired the synthesis of tungsten ink material (Costa 2012). In the presented research work, the thickness of the printed film could be around 100 nm. In this dissertation, commercial tungsten powder was mixed with a designed solvent to enable the e-jet printing of micro/nano shielding structures. Figure 5 presented printed samples of synthesized tungsten ink. Solvent materials are critical for the tungsten ink. The different solvent materials percentage will decide the printability, uniformity, viscosity, dragging efficiency, and X-ray absorption rate of the synthesized ink.

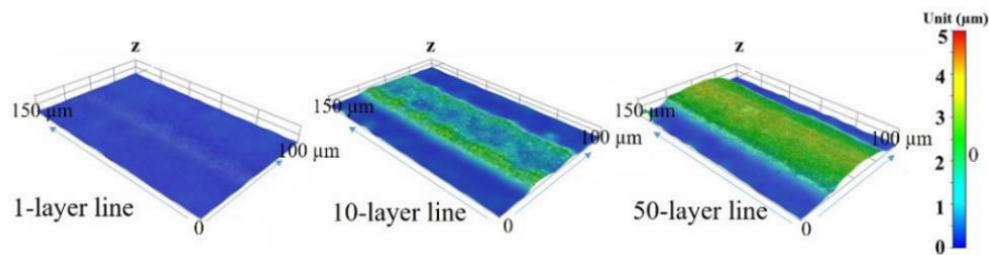


Figure 5. Microscope images and measurement of tungsten ink printed patterns on glass substrate

In-situ monitoring system for electrohydrodynamic inkjet printing

As one of the arising and alternative micro/nanomanufacturing approaches, unexpected defects occur during the e-jet printing process. There are various reasons for the generation of defects: the resolution/stability of the moving platform, the substrate, particles in the air, electrode setup, wave generator issue, the bubble in ink, and variation of the standoff distance. It is necessary to monitor the printing process and detect possible defects. Now there is little research working on monitoring the e-jet printing process. An electrical force controls E-jet

printing. A current sensor is installed to measure the current change during the printing process (Mishara 2010). It is assumed that a charged droplet is released from the nozzle when a small current is generated. It is demonstrated that the size of the droplet is proportional to the peak of the current value, according to research from the University of Illinois Urbana-Champaign. Figure 6 presented a feedback control framework of the e-jet printing system. Similar research work is presented in Rensselaer Polytechnic Institute (Carter 2014). The current signal is detected as a feedback signal to be sent to the model used to present the droplet's shape. Based on the mapping of ink properties, voltage, and droplet dimension, a voltage calibration will be sent to calibrate and input a new voltage signal to print.

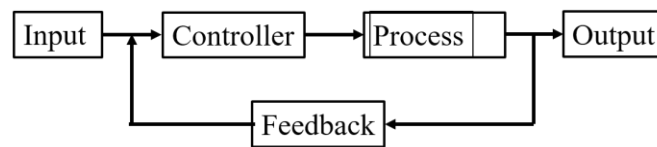


Figure 6. Feedback control framework

Control of electrohydrodynamic inkjet printing process

Once it is accessible to monitor and detect defects during the e-jet printing process, the control of printing parameters to calibrate the system back to normal is a problem. There are several printing parameters: plotting speed, voltage amplitude, pulse width, standoff distance, printing frequency, which could influence the dimension of deposited patterns. There are two approaches to predicting the printing results: finite element analysis and statistical model prediction. The finite element analysis method is based on the fluid mechanical calculation, and the results will be predicted and presented from theoretical calculation or simulation results. There are three stages for the formation of droplets: ejection, droplet formation, droplet steady. Starting from 0 ms, the ink is charged and ready to be ejected. Droplet formation started as a Taylor Cone shape and then elongated. Once the droplet detached from the nozzle, it started to

turn into a steady-state and deposit on the substrate (Chen 2006). The statistical model is based on analyzing the physical phenomenon and determining influential factors to establish a mathematical model to predict the dimension of printed results. These models take comprehensive consideration of influential factors and quantify these factors into a statistical model and predict the dimension without involving the systematic inkjet theory. These models provide another perspective view to support error-free e-jet manufacturing. The droplet heights and diameters were predicted by theoretical calculation (Cater 2014). The average prediction errors for droplets' diameter and height are 10.35% and 12.5%, respectively. But it has to be mentioned that before applying the correction factor in the equation, the average prediction errors for the diameter and height are 28.8% and 30.8%. The variation of environmental conditions was claimed to be the main reason.

However, the theoretical method of predicting the dimension could not always be the best option. Environment factors influence it, and the simulation could be challenging if all the influential factors are considered in the model. Even now, the simulation software could not provide a promising solution for all e-jet printing scenarios. Experiments were designed and conducted to predict the diameter of printed silver nanoink dots pattern (Laurila 2017). A total number four variables were considered in the research: printing frequency, standoff distance, maximum voltage, and bias voltage. A total number of 54 groups of experiments were done, and the claimed prediction accuracy of 94.2% was demonstrated. The morphology of the dot and times of experiments are not perfect in this situation. However, it has explored to predict the dimension in a statistical manner.

References

- AbuAlRoos, N. J., Azman, M. N., Amin, N. A. & Zainon, R., 2020. Tungsten-based material as promising new lead-free gamma radiation shielding material in nuclear medicine. *Physica Medica.*, 78: pp. 48-57.
- Barrie, A. & Christensen, N. E., 1976. High-resolution X-ray photoemission spectra of silver. *Physical Review B*, 14(6): pp. 2442.
- Barton, K., Mishra, S., Shorter, K. A., Alleyne, A., Ferreira, P. & Rogers, J. A., 2010. Desktop electrohydrodynamic jet printing system. *Mechatronics*, 20(5): pp. 611-616.
- Boute, W., Stoop, G., Van Arragon, G. W. & Mensink, K. A., 1986. Biomedical system with improved marker channel means and method. United States patent US 4,601,291.
- Carter, W., Popell, G. C., Samuel, J. & Mishra, S., 2014. A Fundamental Study and Modeling of the Micro-Droplet Formation Process in Near-Field Electrohydrodynamic Jet Printing. *Journal of Micro and Nano-Manufacturing*, 2(2).
- Chen, C. H., Saville, D. A. & Aksay, I. A., 2006. Scaling laws for pulsed electrohydrodynamic drop formation. *Applied Physics Letters*, 89(12): pp. 124103.
- Costa, C., Pinheiro, C., Henriques, I. & Laia, C. A., 2012. Inkjet printing of sol-gel synthesized hydrated tungsten oxide nanoparticles for flexible electrochromic devices. *ACS applied materials & interfaces*, 4(3): pp. 1330-1340.
- Ghilan, A., Chiriac, A. P., Nita, L. E., Rusu, A. G., Neamtu, I. & Chiriac, V. M., 2020. Trends in 3D Printing Processes for Biomedical Field: Opportunities and Challenges. *Journal of Polymers and the Environment*, pp. 1-23.
- Kobayashi, S., Hosoda, N. & Takashima, R., 1997. Tungsten alloys as radiation protection materials. *Nuclear Instruments and Methods in Physics Research Section A: Accelerators, Spectrometers, Detectors and Associated Equipment*, 390(3): pp. 426-430.
- Laurila, M. M., Khorramdel, B., Dastpak, A. & Mäntysalo, M., 2017. Statistical analysis of E-jet print parameter effects on Ag-nanoparticle ink droplet size. *Journal of Micromechanics and Microengineering*, 27(9): pp. 095005.
- Mishra, S., Barton, K. & Alleyne A., 2010. Control of high-resolution electrohydrodynamic jet printing. In *Proceedings of the 2010 American Control Conference*, pp. 6537-6542.
- Myers, R., T. & Ayers, J., 2019. A nitric oxide sensor fabricated through e-jet printing towards use in bioelectronics interfaces. *Journal of Applied Electrochemistry*, 49(2): pp. 229-239.
- Vidmar, T., Topič, M., Dzik, P., & Krašovec, U. O., 2014. Inkjet printing of sol-gel derived tungsten oxide inks. *Solar energy materials and solar cells*, 125: pp. 87-95.

Wei, C. & Dong, J., 2013. Direct fabrication of high-resolution three-dimensional polymeric scaffolds using electrohydrodynamic hot jet plotting. *Journal of Micromechanics and Microengineering*, 23(2): pp. 025017.

Yang, Y., Tong, C., Zhong, J., Huang, R., Tan, W. & Tan, Z., 2018. An effective thermal therapy against cancer using an E-jet 3D-printing method to prepare implantable magnetocaloric mats. *Journal of Biomedical Materials Research Part B: Applied Biomaterials*, 106(5): pp. 1827-1841.

CHAPTER 3. FABRICATION OF SILVER MICROSTRUCTURES VIA ELECTROHYDRODYNAMIC INKJET PRINTING AS CUSTOMIZATBLE X-RAY MARKER IN BIO-STRUCTURE FOR BIOMEDICAL DIAGNOSTIC IMAGING

Authors and Affiliations

Modified from a manuscript to be published in International Journal of Advanced Manufacturing Technology. This research work is published by Xiao Zhang, Xuepeng Jiang, Zhan Zhang, and Hantang Qin in the Int J Adv Manuf Technol (2021).

Xiao Zhang, Xuepeng Jiang, Hantang Qin are from the Industrial and Manufacturing Systems Engineering Department at Iowa State University.

Zhan Zhang is from the Center for Nondestructive Evaluation.

Xuepeng Jiang has contributed to the X-ray data collection, image analysis of the leaf's printed patterns. Zhan Zhang has provided the X-ray equipment, theoretical analysis of X-ray imaging, and review for this paper. I want to acknowledge my advisor, Dr. Hantang Qin's support for accomplishing this research work.

Abstract

X-ray markers have been applied for diagnostic purposes in the medical imaging field. However, they were not flexible enough to accommodate the fast evolution of biomedical applications leading to a considerable performance gap. EHD-Inkjet printing technique as a high-resolution, low-cost, and flexible approach was used to fabricate a silver X-ray marker to fill the gap in the biomedical field. Even though X-ray characterization of bulk silver had been studied, silver nanoink has presented a different X-ray absorption response. To understand the X-ray characterization of silver microstructures, multiple samples were fabricated. The EHD-Inkjet printing system was applied to fabricate silver microstructures under optimized printing parameters, including voltage amplitude, pulse width, frequency, and printing speed. To understand X-ray characteristic differences between bulk silver and nanoink silver, experiments

were designed to print a single layer and multiple layers of silver nanoink lines. Microstructures, which were e-jet printed by silver nanoink, presented different X-ray absorption rate to the bulk silver under the same radiation condition and thickness. Sub-30 μm microstructures of silver nanoink were achieved by e-jet printing; part of them will serve as the X-ray marker in bio-scaffold. This research proposed a method to bridge the e-jet printing technique with a customizable X-ray marker in bio-scaffold, which could effectively resolve the problem of flexibility, improve the resolution, and reduce the cost of manufacturing. Moreover, it supported the development of biomedical products that were fabricated by silver nanoink material, such as in-vivo embedded bio-sensors in computed tomography applications.

Introduction

X-ray imaging of bulk silver has been investigated and successfully adopted in a wide range of radiographic applications such as calibration of X-ray radiography equipment (Bearden 1967; Mao 1978). In recent years, silver nanoink has been widely used in micro/nanoscale manufacturing for biomedical sensors (Kim 2014; Gniatek 2011), electronic components (Qin 2017; Yeo 2016), anti-bacteria agents (Vimala 2009; Lee 2017), etc. However, rare research has been conducted to understand the X-ray characteristics of functional silver nanoink microstructures. Due to differences in the properties of bulk silver and silver nanoink (usually composed of silver nanoparticles or nanowires), radiographic performances of silver microstructures made by the two different forms of silver are expected to be different. X-ray characterization of silver microstructures fabricated using silver nanoink could contribute to the inspection of electronics, computed tomography (C.T.) scanning of biomedical sensors, etc. For example, silver nanowire has been applied in observing physical and chemical reactions with the help of X-ray knowledge (Sun 2011). Silver-based crystals were embedded in bacteria with transmission X-ray microscopy, and this technique could be used for organic-metal fabrication in

the thin film (Klaus 1999). Reed et al. conducted X-ray absorption studies with synchrotron radiation to measure inter-nuclear distances in iron-sulfur proteins (Reed 1977). X-ray absorption data has been reported to prove the atomic origin of the electrophilic oxygen on the catalyst surface in experiments (Bukhtiyarov 2011). X-ray photoelectron spectroscopy was used to observe the silver nanoparticle on cotton fabric as an antibacterial textile finish (Zhang 2009).

In general, silver nanoink is used to fabricate functional components in micro/nanoscale (Perelaer 2006; Ahn 2009; Lee 2005). To understand radiographic performance and characterize the X-ray effect of silver nanoink, high-quality micro/nanoscale patterns need to be fabricated first. In our previous works, we used silver nanoink to print touch sensors on a flexible substrate and showed high-resolution printing of different patterns with good conductivity and sensitivity (Qin 2017). It could also be applied to sensing applications such as eye and skin sensor, and pressure detector on a soft substrate (e.g., PDMS) (Prieto 2000; Moqrich 2005). The fabrication of micro and sub-micron scale patterns is still a challenge in the field if the resolution, cost, accessibility, quality, functionality, and time factors are all considered.

Traditional approaches such as lithography and etching for fabricating the patterns on chips may result in high costs and pollution (Wendel 1994; Park 2007). The fabrication cost could be extremely high if electronics or sensors were fabricated in small batches. Moreover, traditional, clean-room based fabrication processes have to be finished on top of the silicon substrate (Schift 2008). On the other hand, these methods are too complicated for the rapid prototyping of sensors, especially when a micro-level functional electronic device is needed (Levinson 1999; Ye 2004). E-jet printing technique has provided a promising solution, which is both simple and cheap. E-jet printing is a low-cost, high-resolution, fast speed, flexible printing approach to fabricate electronics or sensors in normal lab environments instead of requiring

high-level cleanroom environments (Mishra 2010; Han 2018). Remarkable physical properties and high-resolution patterns are the most outstanding performances of the e-jet printing technique. Our previous work used an amplified A.C. voltage signal to fabricate a micro silver track with a width of sub-20 μm , and this conductive line was demonstrated to have a resistivity 3.16 times than bulk silver for the first time (Qin 2014). Han fabricated a high aspect-ratio 3D structure with a sub-10 μm resolution (Han 2014). After that, a functional touch sensor with high sensitivity was fabricated using e-jet printing with silver nano ink (Park 2014). Park used AC-pulsed voltage to fabricate a transparent electrode. These researches discussed the influence of a single parameter for solving their engineering problem. However, the intrinsic properties of radiographic performance were not discussed for silver nanoink patterns.

Printing parameters such as voltage amplitude, printing speed, standoff distance, pulse width, and frequency could impact the pattern quality in e-jet printing (Onses 2015). A high-resolution three-axis movement stage was used for the printing of different patterns on the substrate. The resolution of the movement was micro/nanoscale, which enabled the accurate control of the printing of the pattern. A micro-level nozzle was fixed on the z-axis for controlling an optimal standoff distance between the conductive substrate and conductive nozzle (Park 2014). High voltage was applied between the conductive substrate and conductive nozzle, and conductive ink material was then driven by an electrical force. Dong used AC-pulsed voltage to fabricate electrical features and connectors to avoid the charge accumulation problem on the highly insulated substrate (Wei 2014; Wei 2015). Other than the electrical force, air gas was sometimes used to overcome the surface tension at the tip of the nozzle. Lee used a novel gas pump system alignment method to control the flow of the ink to realize a highly aligned and patterned silver nanowire (Lee 2014). Not only were different approaches applied to improve the

printing quality by controlling the relevant printing parameters, but e-jet printing has also been studied for simulations, device fabrication, and system integration on various substrates. Han used the FEA method and experiment to observe the droplet formation and settlement phenomenon during the e-jet printing process (Han 2015). Moreover, the printing could be applied to different substrates such as PDMS and PET films (Coppola 2011; Yang 2016).

Fabrication of silver X-ray marker in bio-scaffold via e-jet printing presented application potential in the biomedical research area. Flexibility to print on various substrates and high-resolution down to sub-30 μm are among the significant advantages of e-jet printing for providing a solution to fill the technical gap. Silver microstructures were achieved by e-jet printing under the control of parameters of voltage amplitude, pulse width, printing speed, and frequency. Understanding the X-ray characteristic of silver nanoink was another challenge that could help to reflect the silver pattern after radiography. Commercial bulk silver samples were scanned for comparison and demonstration of the difference to silver nanoink, which further supports the necessity of quantitative X-ray characterization. Through the platform of e-jet printing, a high-resolution customized silver X-ray marker in bio-scaffold was provided for medical diagnosis applications. Moreover, it contributed to the detection of sensors or electronics, which was fabricated by silver nanoink material such as embedded in-vivo biosensors.

Schematic of electrohydrodynamic inkjet printing & setup of X-ray imaging

Electrohydrodynamic inkjet (e-jet) printing

The schematic of e-jet printing was shown in Figure 7(a). This system included a nanopositioning three-axis stage, a waveform signal generator, a voltage amplifier, a pneumatic air supply system, and a syringe holder system. The three-axis stage in this study has a minimum resolution of 50 nm. The printing speed could vary from 0.01 mm/s to 15 mm/s. Waveform

signal generator could provide different signals such as D.C., step signal, sine signal, and triangle signal.

Before the printing process, droplets were charged and then jetted on the substrate. If all the charged droplets have the same polar, the electrical field between nozzle and substrate could be changed, resulting in defects in the pattern. So direct current (D.C.) voltage was substituted by alternating current (A.C.) voltage to generate the electrical field to jet silver nanoink material in this research. A voltage amplifier was installed to amplify the signal generated from the signal generator. In the study, the pulsed A.C. signal was applied to control the printing, as shown in Figure 7(d). A designed holder system was used to hold a syringe of different sizes on the z-axis movement motor. Before the printing, the silver nanoink was supplied into the nozzle. Between the conductive nozzle and substrate, the electrical field was applied by the high voltage amplifier to overcome the surface tension and jet the conductive ink out of the nozzle tip. As shown in Figure 7 (b), the upper part of the nozzle was the syringe. The lower part (highlighted as the triangle) was the Taylor cone. The bottom of the image computed reflected the upper nozzle and printing on the reflective substrate. The diameter of this nozzle was $19.2\mu\text{m}$, and the standoff distance between the conductive nozzle and substrate was $50\mu\text{m}$. Taylor cone was generated, and silver nanoink was deposited on the substrate. Figure 7 (c) demonstrated a pad pattern (RFID sensor) fabricated on a glass substrate using silver nanoink material. The average width of the conductive silver tracks was $15\mu\text{m}$.

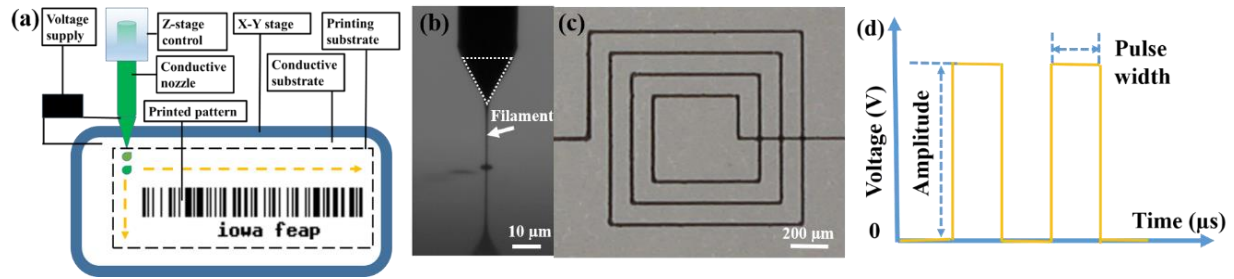


Figure 7. (a) Schematic of e-jet printing; (b) Nozzle and its reflection from the glass substrate; (c) Example of printed patterns; (d) Generated signal for printing

Material characterization of silver nanoink and microstructures

The deposited silver nanoink pattern was investigated by X-ray Powder Diffraction (XRD) equipment to characterize the composition of printed products. According to the XRD standard (PXRD, Ref. No. 01-087-0718), the XRD image demonstrated that the peaks with (111)(200)(220)(311)(331) had high intensity. Among them, the highest growth orientation of silver nanoink pattern was fixed at (111) direction. The peak values match with silver, which supported that printed patterns were silver without oxidation. This finding will support the X-ray absorption rate analysis in the following part. Figure 8 (b) presented an SEM image of a silver nanoink. This silver nanoink was a nanoscale commercial silver ink from Sigma-Aldrich (50 wt % dispersion in tripropylene glycol monomethyl ether with a viscosity of 24 cP). From this SEM image, the single-particle of silver nanoink could be observed as sub-50 nm, and particles tend to aggregate together to form relatively stable nanostructures, which vary from 500 nm to 1000 nm.

X-ray radiography imaging system

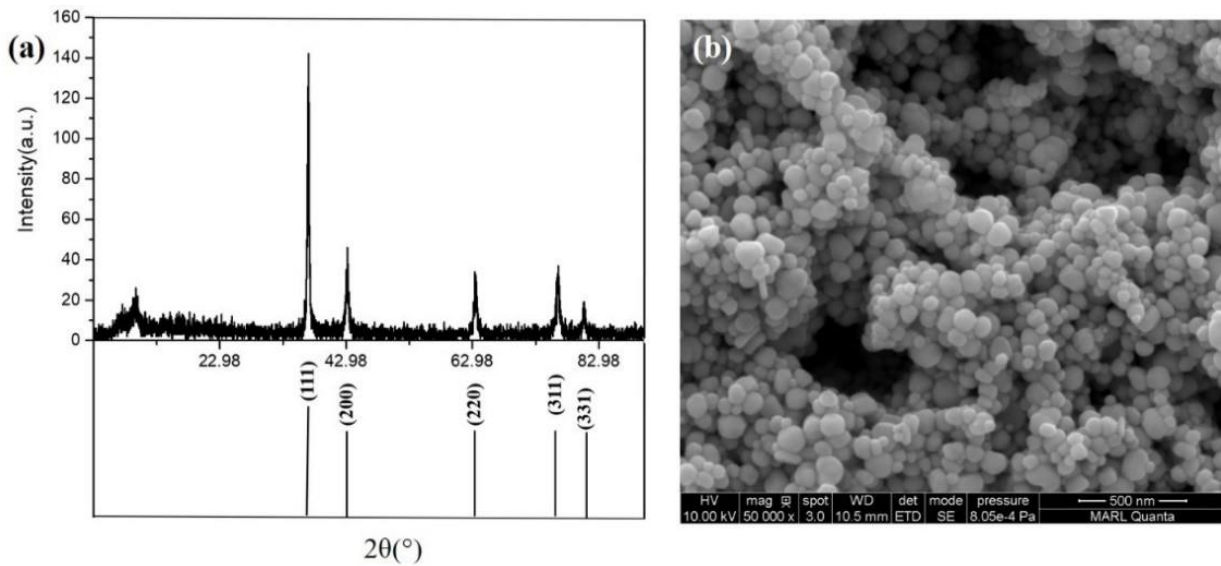


Figure 8. (a) XRD image of silver nanoink pattern and (b) SEM image of silver nanoink pattern (right)

Figure 8(a) demonstrated the X-ray radiography equipment used to characterize the radiographic performance of the sample. This equipment included a microfocus X-ray source, three-axis movement stage, sample platform, and flat-panel detector. The three-axis sample stage holder mounted the sample between the X-ray source and the detector. The P.C. computer could control the stage movement and the intensity of the emitted X-ray to take the radiography image. The X-ray source could generate a cone beam X-ray up to 225KeV. The X-ray photons with different energy could penetrate the sample with a different probability, according to Beer-Lambert law (Bunker 2010). Meanwhile, different materials with a different thickness along the ray path have different X-ray absorption coefficients. After attenuation, the X-ray signal detected through a ray path could reflect this variation with greyscale value. 2D radiography images of samples could be acquired with the position information of each pixel.

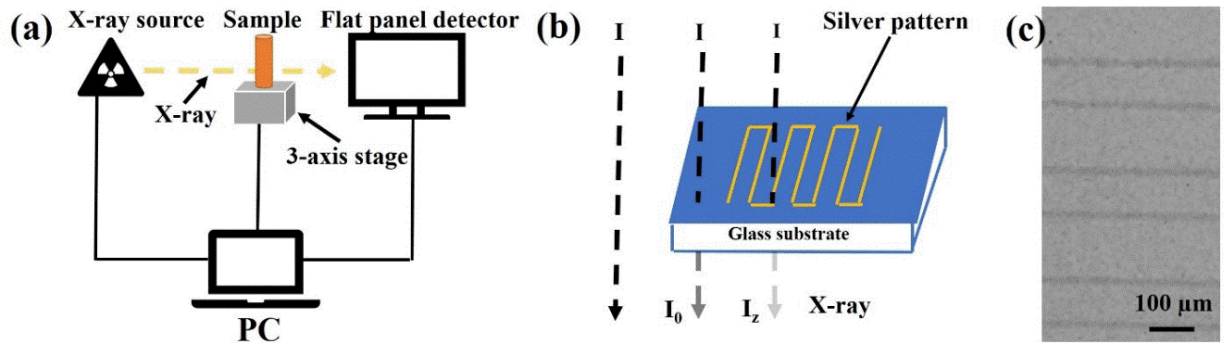


Figure 9. (a) Schematic of X-ray imaging instrument; (b) Model of X-ray absorption; (c) X-ray imaging of printed single-layer silver line

Inside the flat panel detector, scintillator cesium iodides (CsI) convert X-ray photons to visible light photons, then CMOS electronics convert them into electrical signals (represented by greyscale), which was proportional to the X-ray beam intensity arrive at this pixel. Figure 9(b) presented the X-ray absorption model, and it explained three different situations during X-ray imaging experiment: X-ray went to flat panel detector without any blocking; X-ray went to the detector with blocking by glass substrate; X-ray went to the detector with blocking by a glass substrate and pattern of silver nanoink. Figure 9(c) showed the X-ray image of a silver pattern on a 1 mm thick glass substrate with X-ray radiography parameters: voltage 30 kV, current 1000 μA , and exposure time 6500 milliseconds. This image was an average of 8 images taken under the same parameters for reducing the white noise.

Results and discussion

Influence of printing parameters

The needle was fabricated from a glass puller, and the manufactured needle diameter varied from 10 μm to 100 μm . The glass needle will be mounted on the metal needle, under electrical filed the silver nanoink will form a Tylor Cone on needle tip and finally be dragged on a reflective glass substrate. Surface tension $\gamma = F/d$, where F is the electrical force at the

nozzle, and d is the length along the force direction, which equals to the diameter of the nozzle. The equation could determine the minimum force (related to the voltage applied) required to drive a continuous jetting during the EHD-Inkjet printing process.

A.C. voltage alternatively provided negative and positive voltage during the printing process. Pulse width is a parameter that allows some amount of time of voltage applied during one signal cycle. Low amplitude of voltage could not generate a strong enough electrical field to propel the ink out of the nozzle. The high amplitude of voltage would result in unstable droplets and Taylor cone, which could reduce the quality of the pattern. In this research, the optimal voltage range, which could drive silver nanoink out of nozzle and print stable microstructures, was investigated. At the beginning, 800V A.C. voltage was applied to jet material. After that, droplets were printed on the substrate under calibration of reducing the voltage by 30V each time. This operation could help to explore the optimal voltage amplitude. From Figure 9(a), voltages were applied as 450V, 500V, 550V, 600V, and a growing line width could be seen to grow from 10 μ m to 30 μ m.

Table 1. Specification of the e-jet printing process

| | Pulse width (μ s) | Voltage amplitude (V) | Voltage frequency (Hz) | Standoff distance (μ m) | Printing speed (mm/s) | Layer number | Needle diameter (μ m) |
|---------|------------------------|-----------------------|------------------------|------------------------------|-----------------------|--------------|----------------------------|
| Group1 | 200 | 450, 500 550, 600 | 200 | 30 | 1 | 1 | 20 |
| Group 2 | 160,180 200, 220 | 550 | 200 | 30 | 1 | 1 | 20 |
| Group 3 | 200 | 550 | 50, 100 200, 300 | 30 | 1 | 1 | 20 |
| Group 4 | 200 | 550 | 200 | 30 | 1, 2 4, 8 | 1 | 20 |

From Figure 9(b), when the pulse width was increased, the line width grew from $7\mu\text{m}$ under $160\mu\text{s}$ to $27\mu\text{m}$ under $180\mu\text{s}$. Although the diameter decreased from $38\mu\text{m}$ under $220\mu\text{s}$ to $48\mu\text{m}$ under $200\mu\text{s}$, the line printed under $200\mu\text{s}$ pulse width was printed at the beginning, so the material flow condition may be changed in this period, which could explain the sudden linewidth decrease. A.C. voltage was applied in this printing process, and frequency could be controlled to generate designated droplets. The higher frequency could contribute to larger droplets, as shown in Figure 9(c), line width went from $13\mu\text{m}$ (50Hz) voltage to $38\mu\text{m}$ (300Hz). As more droplets fell in the same place, the line width increased. As the printing speed started to increase, the line width will decrease due to fewer droplets could be placed in the same place. Line width dropped from $48\mu\text{m}$ to $8\mu\text{m}$, as presented in Figure 9(d). Detailed parameters for the printed samples were shown in Table 1.

X-ray imaging characterization and absorption analysis

This research would conduct and design experiments to characterize the X-ray absorption rate of silver nanoink printed microstructure. To provide the audience with a reference, commercial bulk silver samples were tested under X-ray radiography. Commercial bulk silver has a stable thickness, and it has been used for the calibration of X-ray radiation. A commercial bulk silver sheet is 10 cm by 10 cm square, while the thickness of this sheet was $25\mu\text{m}$. This bulk sheet was sliced into 16 pieces of the same size: 2.5 cm by 2.5 cm square. Thus, the different bulk silver thickness was tested under X-ray radiography to provide the greyscale value, as shown in Figure 10. This curve has characterized the X-ray absorption rate of bulk silver from the thickness of $75\mu\text{m}$ to $225\mu\text{m}$. Based on this graph, we could compare the X-ray shielding capability of bulk silver and silver nanoink fabricated structure under the same thickness.

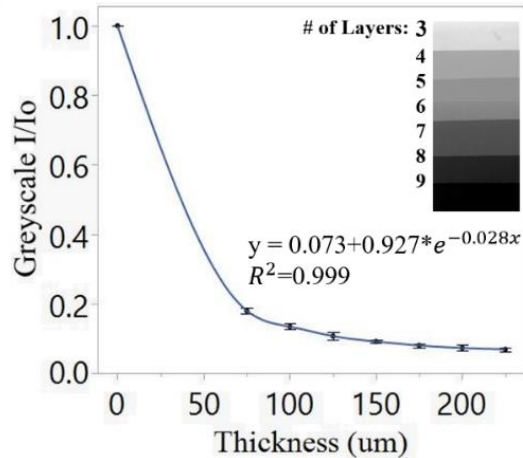


Figure 10. Bulk silver function of greyscale I/I_0 with different thicknesses together with an X-ray image of those bulk silver

Experiments were conducted to fabricate silver nanoink microstructures with different thicknesses: multi-layer patterns with layer numbers: 1, 10, 50 were printed, with different thickness values. Optical microscopy with a 3D reconstruction function was used to measure the thickness of different samples. The measured results were presented in Figure 6. After that, these samples were scanned by X-ray radiography.

From the X-ray imaging results, it was expected to predict the correlation between thickness and greyscale value. As shown in the above description, I_0 was X-ray intensity captured without blocking material along the X-ray path, I_z was X-ray intensity with ink pattern. For intensity evaluation, multiple greyscale scale values were randomly chosen for each sample pattern. The intensity I was calculated by averaging the greyscale value of those pixel points.

As shown in Figure 10, I_0 was the value of the pure greyscale value without blocking material along the X-ray path. I_z represented the greyscale value with the silver material. It can be found from the curve that as the growth of the thickness of the bulk silver sheet or silver nanoink, the X-ray absorption amount was higher. From Equation 1, the detected data of bulk

silver could be fed and fitted into a function shown in Figure 10, and the R^2 value presented an excellent fitting.

It was assumed that the greyscale value would be 1 when the thickness of the material is 0. Taking all these data points into consideration, the equation in Figure 10 was achieved by using the Exponential 3P function to fit in JMP software. For the silver nanoink pattern, fifty layers thickness was around $4\mu\text{m}$, and this I_z/I_0 value was 0.97. It indicated that nearly 3% of X-ray radiation could be absorbed by the printed silver pattern. With the same thickness, I_z/I_0 value calculated from the equation in Figure 5 was 0.88.

Thus, the printed silver line can absorb more X-ray radiation than the bulk silver at the same thickness, exhibiting high X-ray radiation shielding property. This phenomenon was convincible and easily explained since a thicker sample could block more X-ray s. The X-ray shielding efficiency was determined by the structure density and thickness. At the same thickness, higher density structures have much more atoms at the direction X-ray passed through, resulting in better absorption ability. The next attempts of our work are building several grating masks and print silver nanoink into these grating gaps to generate high aspect ratio and high thickness lines and films.

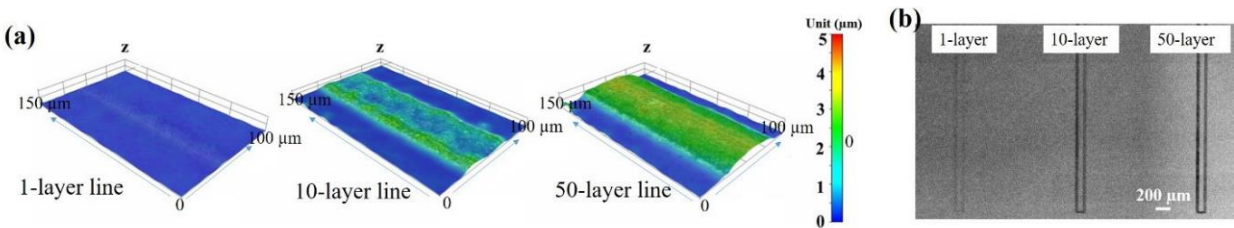


Figure 11. (a) 3D image of printed multi-layer silver patterns using nanoink; (b) X-ray imaging of multi-layer patterns from left to right: 1 layer, 10 layers, and 50 layers

Designed pattern fabrication and biomedical application

Spectacles pattern was printed under different voltage, as shown in Figure 12(a) and (b). In Figure 12(a), parameters were printed out, which indicate the robustness of this printing technique. With voltage control during the printing process, the sunglass pattern could be achieved in Figure 12(b). The enlarged part of the spectacle presented a fine printing of the curve in Figure 12(c). The curves were uniform, dense, and highly conductive. The circuit pattern was printed on a PET substrate, shown in Figure 12(d). It was demonstrated that a delicate pattern could be fabricated using e-jet printing techniques on multiple substrates with high resolution for sensing. After the fabrication of silver structures and application of X-ray characterization of silver microstructure, components in medical applications such as X-ray marker could be detected by radiography equipment.

The silver nanoink pattern of our lab's logo barcode was fabricated to verify the effectiveness of this approach to fabricate the X-ray marker. A 30 μ m nozzle was used to print this pattern with the dropping frequency of 100Hz on the glass substrate. The standoff distance was 50 μ m, and the printing speed was 2 mm/s. Each width of the printed line was constant by controlling the voltage amplitude and standoff distance. Though the printed lines were not perfect, such as the void portion on one line and bumpy part on some lines, this marker pattern could still be scanned to show the "feap" letter, representing the flexible electronics and printing lab. The fabrication of this pattern proved the precise controllability of the e-jet printing approach.

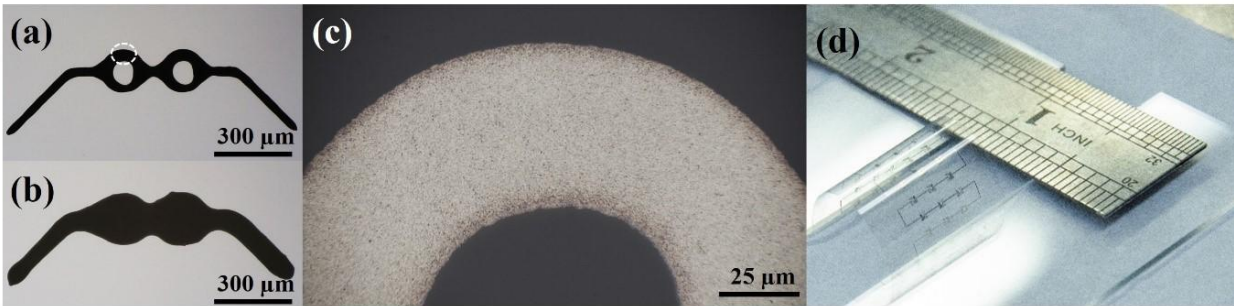


Figure 12. (a) Spectacles pattern was printed on a glass substrate; (b) Spectacles pattern was printed with the higher voltage on a glass substrate; (c) Amplified microscope image of part of glass pattern; (d) Circuit pattern was printed on stretchable PET substrate

Due to the function of the barcode, it could be used to represent a unique object for differentiation purposes. Thus, it promises to realize the diagnostic through images and contribute to the X-ray marker's application in the medical area.

To verify the effectiveness of marking on bio-tissue, the leaf was selected for attaching marker. There are two approaches to fabricate markers for leaf: directly printing on the leaf substrate and printing on a flexible substrate attached to the leaf. The second fabrication approach is to fabricate a pattern on a transparent and thin flexible substrate, and then the printed pattern will be attached with leaf for marking. EHD-Inkjet printing is typically conducted on a reflective and flat substrate, which would allow the operator to locate the position of the needle and program the printed patterns. It is challenging to print on leaf substrate due to the curved nature of the substrate.

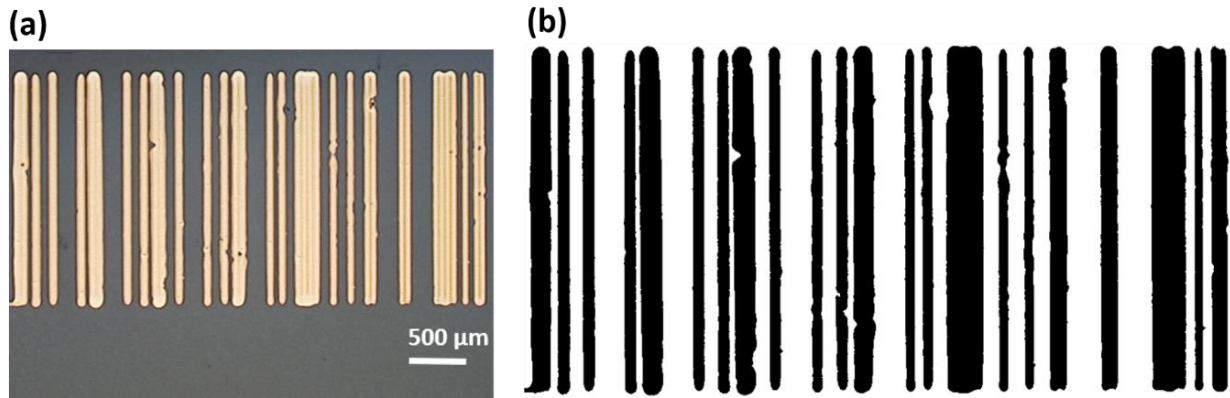


Figure 13. (a) Microscopic image of "feap" barcode fabricated by silver nanoink; (b) Binarized image of the fabricated barcode

Meanwhile, it is impossible to watch the location of the needle to accurately controlling the movement. Thus, the standoff distance was kept at a relatively large value, which is around 5 mm. It was shown in Figure 14(a) of printing on leaf substrate and Figure 14(b) of X-ray scanning result.

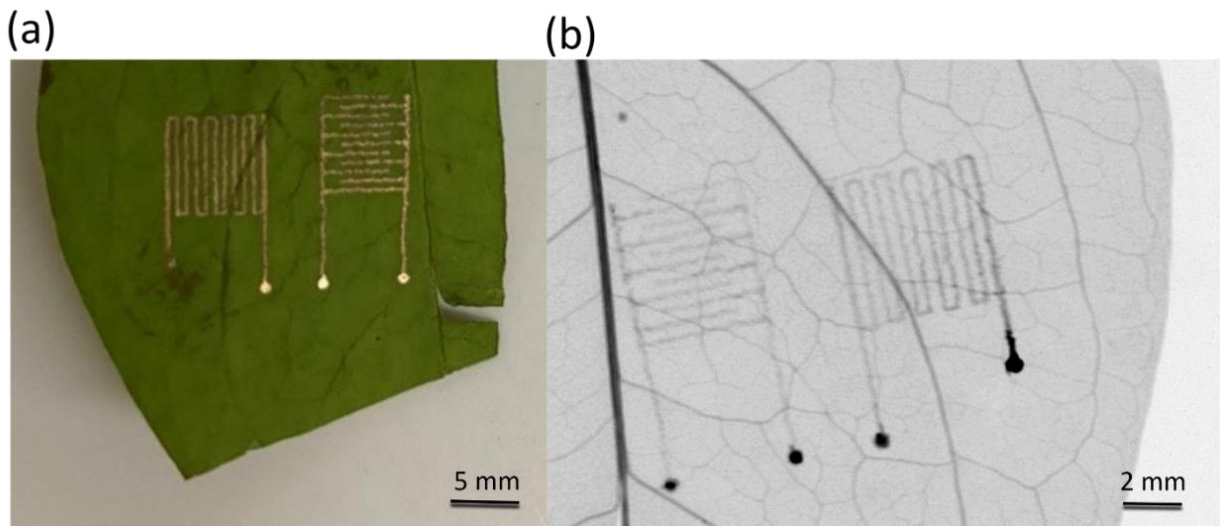


Figure 14. (a) Print marker on leaf substrate (b) X-ray imaging of marker on leaf substrate

To understand the voltage influence on the X-ray imaging greyscale value, experiments were conducted under different voltage values, as shown in Figure 15. Each voltage parameter

setting was used to print three filaments on the leaf for repeatability purposes. Voltage (D.C. signal) range included from 1500V, 1600V, 1700V, and 1800V. From the results, it could be seen that the greyscale value decrease with the growth of voltage value. The higher voltage could generate a more robust electrical field, thus drags more ink onto the leaf substrate. With a thicker printed silver nanoink microstructure, X-ray was absorbed more, which resulted in a smaller greyscale value.

In this research, the X-ray characteristic of silver nanoink fabricated microstructure was investigated to provide the instruction of micro/nanoscale marker manufacture by the EHD Inkjet printing technique. Bulk silver has been researched over the years and applied to the X-ray marker area. It could serve as a reference to compare the X-ray characteristic with the silver nanoink fabricated microstructure that was assumed to behave in a different X-ray absorption rate. Thus, the commercial silver sheet was bought to calculate and calibrate the X-ray absorption rate versus thickness. However, the silver nanoink printed micro-structure was assumed to behave in a different X-ray absorption rate. To verify this assumption, different layers of silver nanoink micro-structure were fabricated by EHD Inkjet printing with micro-scale resolution. It was demonstrated that silver nanoink fabricated structure has a different X-ray absorption rate with the same material thickness. These results further impede the development of applications in industries such as barcode and biomarkers. The barcode was fabricated and X-ray scanned in this manuscript, which could be recognized by a barcode scanner. These high-resolution, low-cost, and flexible characteristics of EHD Inkjet printing combined with reported X-ray responses of silver nanoink microstructure could contribute to the marking and detection in the packaging industry. The following experiments were also successfully printed on the living leaf substrate, and X-ray scanned the precise structure of the printed silver nanoink

marker. It paves the way for the development of marking bio-tissue and using X-ray to accurately locating the tissue in medical research.

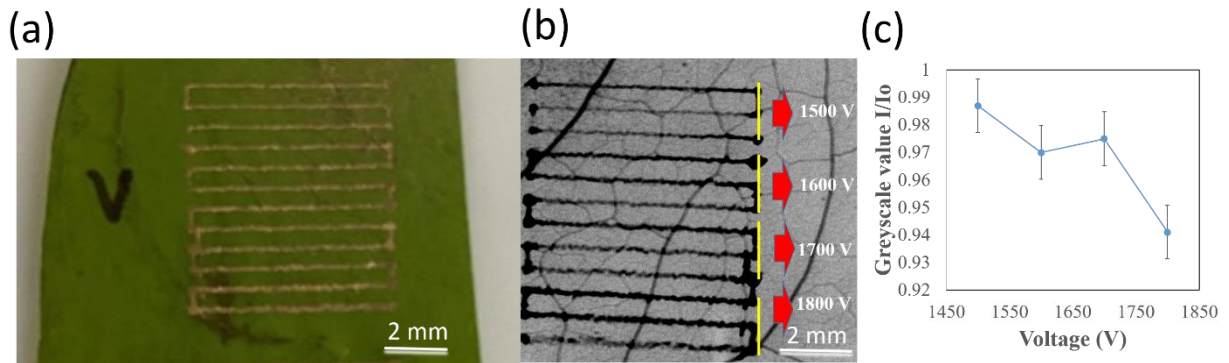


Figure 15. (a) Print marker on leaf substrate under different voltage (b) X-ray image (c) Plotting of the greyscale value trend under the influence of different voltage values

Conclusion

In this research work, the E-jet printing of silver nanoink material was proposed to fabricate functional microstructures. The X-ray characterization of silver nanoink and bulk silver was conducted and compared to present the difference in X-ray absorption rate. The influence of different printing parameters on the dimension of printed patterns was proved. Meanwhile, patterns were printed on bio-substrate to test the potential of application in the biomedical area. Here are the main findings of the e-jet printing and X-ray radiation experiments:

- The e-jet printing system demonstrated the effectiveness of fabricating sub- $30\mu\text{m}$ silver nanoink microstructures on the insulating glass substrate and flexible PET substrate.
- Silver microstructures were fabricated under different printing parameters such as plotting speed, frequency, voltage amplitude, and standoff distance to obtain the optimized parameters.
- The silver nanoink material has the same XRD response as bulk silver.

- The experiment results have shown that nanoink silver printed microstructures presented different X-ray absorption rate to the bulk silver under the same radiation condition and thickness.
- The fabrication of patterns using silver nanoink was successfully conducted on leaf substrate, while the X-ray radiation technique could characterize the pattern. The greyscale value was found to near linearly grow with the increase of voltage amplitude.

In conclusion, the e-jet printing system was demonstrated to be capable of fabricating delicate silver nanoink microstructures. The X-ray characterization of silver nanoink could provide a reference for the design and manufacture of a customizable X-ray marker, which may be used in biomedical diagnostic imaging. In future applications, the research work could pave the way for developing silver nanoink microstructures such as in-vivo embedded biosensors in the biomedical area.

References

- Ahn, B.Y., Duoss, E.B., Motala, M.J., Guo, X., Park, S.I., Xiong, Y., Yoon, J., Nuzzo, R.G., Rogers, J.A. & Lewis, J.A., 2009. Omnidirectional printing of flexible, stretchable, and spanning silver microelectrodes, *Science*. 323(5921), pp. 1590-1593.
- Bearden., 1967. X-ray wavelengths. *Reviews of Modern Physics*. 39(1), pp. 78.
- Bukhtiyarov, V. I., Hävecker, M., Kaichev, V.V., Knop-Gericke, A., Mayer, R.W. & Schlögl, R., 2011. X-ray absorption and photoemission studies of the active oxygen for ethylene epoxidation over silver. *Catalysis letter*, 74(3-4), pp. 121-125.
- Bunker, G., 2010. *Introduction to XAFS: a practical guide to X-ray absorption fine structure spectroscopy*. Cambridge University Press.
- Coppola, S., Vespini, V., Grilli, S. & Ferraro, P., 2011. Self-assembling of multi-jets by pyro-electrohydrodynamic effect for high throughput liquid nanodrops transfer. *Lab on a chip*, 11(19): pp. 3294-3298.
- Gniotek, K., Frydrysiak, M., Zięba, J., Tokarska, M. & Stempień, Z., 2011. Innovative textile electrodes for muscles electrostimulation. *IEEE International Symposium on Medical Measurements and Applications*, pp. 305-310.

- Han, Y., 2018. High-Resolution Electrohydrodynamic (EHD) 3D Printing of Function Materials. Ph.D. thesis, North Carolina State University library.
- Han, Y., Wei, C. & Dong, J., 2014. Super-resolution electrohydrodynamic (EHD) 3D printing of micro-structures using phase-change inks. *Manufacturing Letters*, 2(4): pp. 96-99.
- Han, Y., Wei, C. & Dong, J., 2015. Droplet formation and settlement of phase-change ink in high resolution electrohydrodynamic (EHD) 3D printing. *Journal of Manufacturing Processes*, 20: pp. 485-491.
- Kim, J. & Kim, W.S., 2014. Stretching silver: printed metallic nano inks in stretchable conductor applications. *IEEE Nanotechnology Magazine*, 8(4), pp. 6-13.
- Klaus, T., Joerger, R., Olsson, E. & Granqvist, C.G., 1999. Silver-based crystalline nanoparticles, microbially fabricated. *Proceedings of the National Academy of Sciences*, 96(24), pp. 13611-13614.
- Lee, H., Seong, B., Kim, J., Jang, Y. & Byun, D., 2014. Direct alignment and patterning of silver nanowires by electrohydrodynamic jet printing. *Small*, 10(19): pp. 3918-3922.
- Lee, H.H., Chou, K.S. & Huang, K.C., 2005. Inkjet printing of nanosized silver colloids. *Nanotechnology*, 16(10), pp. 2436.
- Lee, S.J., Heo, D.N., Heo, M., Noh, M.H., Lee, D., Park, S.A., Moon, J.H. & Kwon, I.K., 2017. Most simple preparation of an inkjet printing of silver nanoparticles on fibrous membrane for water purification: Technological and commercial application. *Journal of Industrial and Engineering Chemistry*, 46, pp. 273-278.
- Levinson, H.J., 1999. *Lithography process control*. SPIE Press.
- Mao, H., Bell, P. & Shaner, J., 1978. Specific volume measurements of Cu, Mo, Pd, and Ag and calibration of the ruby R 1 fluorescence pressure gauge from 0.06 to 1 Mbar. 49(6), pp. 3276-3283.
- Mishra, S., Barton, K.L., Alleyne, A.G., Ferreira, P.M. & Rogers, J.A., 2010. High-speed and drop-on-demand printing with a pulsed electrohydrodynamic jet. *Journal of Micromechanics and Microengineering*, 20(9): pp. 095026.
- Moqrich, A., Hwang, S.W., Earley, T.J., Petrus, M.J., Murray, A.N., Spencer, K.S., Andahazy, M., Story, G.M. & Patapoutian, A., 2005. Impaired thermosensation in mice lacking TRPV3, a heat and camphor sensor in the skin. *Science*, 307(5714), pp. 1468-1472.
- Onses, M. S., Sutanto, E., Ferreira, P.M., Alleyne, A.G. & Rogers, J.A., 2015. Mechanisms, capabilities, and applications of high-resolution electrohydrodynamic jet printing. *Small*, 11(34): pp. 4237-4266.

- Park, J. & Hwang, J., 2014. Fabrication of a flexible Ag-grid transparent electrode using ac based electrohydrodynamic Jet printing. *Journal of Physics D: Applied Physics*, 47(40): pp. 405102.
- Park, J., Kim, B., Kim, S.Y. & Hwang, J., 2014. Prediction of drop-on-demand (DOD) pattern size in pulse voltage-applied electrohydrodynamic (EHD) jet printing of Ag colloid ink. *Applied Physics A*, 117(4): pp. 2225-2234.
- Park, S.R., Peng, H. & Ling, X.S., 2007. Fabrication of nanopores in silicon chips using feedback chemical etching. *Small*, 3(1): pp. 116-119.
- Perelaer, J., De Gans, B.J. & Schubert., 2006. Ink-jet printing and microwave sintering of conductive silver tracks. *Advanced materials*, 18(16), pp. 2101-2104.
- Prieto, P.M., Vargas-Martin, F., Goelz, S. & Artal, P., 2000. Analysis of the performance of the Hartmann–Shack sensor in the human eye. *JOSA A*, 17(8):1388-1398.
- Qin, H., Cai, Y., Dong, J. & Lee, Y.S., 2017. Direct printing of capacitive touch sensors on flexible substrates by additive E-jet printing with silver nanoinks. *Journal of Manufacturing Science and Engineering*, 139(3).
- Qin, H., Dong, J. & Lee, Y.S., 2017. Fabrication and electrical characterization of multi-layer capacitive touch sensors on flexible substrates by additive e-jet printing. *Journal of Manufacturing Processes*, 28, pp. 479-485.
- Qin, H., Wei, C., Dong, J. & Lee, Y.S., 2014. AC-pulse modulated electrohydrodynamic (EHD) direct printing of conductive micro silver tracks for micro-manufacturing. *Flexible Automation and Intelligent Manufacturing*.
- Reed, J., Eisenberger, P., Teo, B.K. & Kincaid, B.M., 1977. Structure of the catalytic site of polymer-bound Wilkinson's catalyst by X-ray absorption studies. *Journal of the American Chemical Society*, 99(15), pp. 5217-5218.
- Schift, H., 2008. Nanoimprint lithography: An old story in modern times? A review. *Journal of Vacuum Science & Technology B: Microelectronics and Nanometer Structures Processing, Measurement, and Phenomena*, 26(2): pp. 458-480.
- Sun, Y. & Wang, Y., 2011. Monitoring of galvanic replacement reaction between silver nanowires and H₂AuCl₄ by in situ transmission X-ray microscopy. *Nano letters*, 11(10), pp. 4386-4392.
- Vimala, K., Sivudu, K.S., Mohan, Y.M., Sreedhar, B. & Raju, K.M., 2009. Controlled silver nanoparticles synthesis in semi-hydrogel networks of poly (acrylamide) and carbohydrates: a rational methodology for antibacterial application. *Carbohydrate polymers*, 75(3), pp. 463-471.

- Wei, C., Qin, H., Chiu, C.P., Lee, Y.S. & Dong, J., 2015. Drop-on-demand E-jet printing of continuous interconnects with AC-pulse modulation on highly insulating substrates. *Journal of Manufacturing Systems*, 37: pp. 505-510.
- Wei, C., Qin, H., Ramirez-Iglesias, N.A., Chiu, C.P., Lee, Y.S. & Dong, J., 2014. High-resolution ac-pulse modulated electrohydrodynamic jet printing on highly insulating substrates. *Journal of Micromechanics and Microengineering*, 24(4): pp. 045010.
- Wendel, M., Kühn, S., Lorenz, H., Kotthaus, J.P. & Holland, M., 1994. Nanolithography with an atomic force microscope for integrated fabrication of quantum electronic devices. *Applied physics letters*, 65(14): pp. 1775-1777.
- Yang, S.M., Lee, Y.S., Jang, Y., Byun, D. & Choa, S. H., 2016. Electromechanical reliability of a flexible metal-grid transparent electrode prepared by electrohydrodynamic (EHD) jet printing. *Microelectronics Reliability*, 65: pp. 151-159.
- Ye, J., Pease, R. F. & Chen, X., 2004. System and method for lithography process monitoring and control. United States patent US 6,828,542.
- Yeo, J.C., Yap, H.K., Xi, W., Wang, Z., Yeow, C.H. & Lim, C.T., 2016. Flexible and stretchable strain sensing actuator for wearable soft robotic applications. *Advanced Materials Technologies*, 1(3), pp. 1600018.
- Zhang, F., Wu, X., Chen, Y. & Lin, H., 2009. Application of silver nanoparticles to cotton fabric as an antibacterial textile finish. *Fibers and Polymers*, 10(4), pp. 496-501.

CHAPTER 4. FABRICATION OF MICRO-SCALE RADIATION SHIELDING STRUCTURES USING TUNGSTEN NANOINK THROUGH ELECTROHYDRODYNAMIC INKJET PRINTING

Authors and Affiliations

Modified from a manuscript to be published in Journal of Micromechanics and Microengineering. This research work is published by Hao Lyu, Xiao Zhang, Fei Liu, Yanhua Huang, Zhan Zhang, Shan Jiang, and Hantang Qin in the Journal of Micromechanics and Microengineering (2019), volume 19, number 1.

Hao Lyu was a visiting scholar in the Industrial and Manufacturing Systems Engineering Department at Iowa State University.

Xiao Zhang, Yanhua Huang, Hantang Qin are from the Industrial and Manufacturing Systems Engineering Department at Iowa State University.

Zhan Zhang is from the Center for Nondestructive Evaluation. Drs. Fei Liu and Shan Jiang are from Material Science and Engineering Department.

Hao Lyu and I have contributed to the definition of the research problem, experiment design, conduction of e-jet printing experiments, X-ray experiments data collection, and analysis throughout this research work. Zhan Zhang has provided the X-ray equipment, theoretical analysis of X-ray imaging, and review for this paper. Dr. Fei Liu and Yanhua Huang have supported the theoretical knowledge of tungsten ink, synthesis of nanoink, and some X-ray experiments during this study. I want to acknowledge my advisor, Dr. Hantang Qin, and Dr. Shan Jiang's support throughout this research work.

Abstract

Electronics components used in space and strategic missions are exposed to harsh radiation environments, which could cause operational malfunction of the system through lattice displacement or ionization effects. One potential solution is to use tungsten as radiation shielding. Tungsten is a very effective material in shielding electronic components and manufacturing gratings for X-ray imaging. However, intrinsic properties of tungsten (e.g., density, chemical/thermal inertness and hardness) post a significant challenge of fabricating the

material into micro-scale and delicate structures, especially in electronic device fabrication. To address the problem, we designed a new tungsten nanoink and developed a straightforward approach to create tungsten micro-structures by 3D printing. Various microstructures down to 10 μ m resolution have been patterned and fabricated by electrohydrodynamic inkjet (e-jet) printing using tungsten nanoink. By optimizing process parameters (voltage modality) and materials properties (ink formulation), the dimension and morphology of the structures can be precisely controlled. An AC-modulated voltage was employed during the e-jet printing process to make the patterns much more controllable and stable. Multi-layer tungsten lines were characterized by X-ray imaging and exhibited excellent absorption of X-ray radiation. With the same thickness, printed lines showed nearly 1/3 absorptivity of X-ray radiation of bulk tungsten, leading to significant radiation attenuation effectiveness. Tungsten nanoink is a new material used in e-jet printing that has not been reported in the literature to the best of authors' knowledge. The study establishes a new methodology of manufacturing micro-nano scale shielding components for electronic devices and rapid prototyping of gratings and collimators in radiography for medical and inspection applications. The research also provides practical guidance to fabricate high melting-point metals via nanoink and micro/nano scale 3D printing.

Introduction

Electrohydrodynamic inkjet (e-jet) printing (Park 2007), a method combining electrohydrodynamic and inkjet printing, has attracted much interest recently in fabricating submicron-to-micron sized structures, including dots, lines, and films (Prasetyo 2013; Jang 2013; Tekin 2006). E-jet printing has certain advantages over the traditional lithography based techniques, such as direct-writing capabilities without the need of complex fabrication processes, extra masks, etching, or developing. In addition, e-jet printing is low-cost and highly versatile with a variety of selections of printable materials on diverse substrates (Han 2018; Brossard

2017; Yudistira 2013). Many metal inks were employed to generate different structures, including silver nanoparticles (Lee 2007), silver nanowires (Cui 2018), quantum dots (Kim 2015), carbon nanotube (Jeong 2016) and graphenes (An 2015). In e-jet printing, printed patterns were deposited onto the substrate layer by layer via nano-scale control of platform movement. After solidifying, the patterns could form reliable and diverse structures as designed (Li 2018). Based on the flexibility and precision of programmable platform movement, both regular patterns and discrete patterns could be fabricated using e-jet printing on various substrates, which has led to unique application in particular fields (Kim 2015; Li 2018), including radiation shielding patterns on electronic components. However, it is still challenging to determine the ink formulations to achieve precise and delicate printing structures.

Electronic components used in strategic and space missions are exposed to harsh radiation environments, which could cause operational malfunction of the system through lattice displacement and ionization effects. Current radiation-hardening techniques for electronics, such as using radiation-resistant materials in standard semiconductor manufacturing or adopting radiation tolerant logical designs, require specially tailored electronic design or manufacturing processes. At present, most radiation-shielding techniques require the use of heavy and thick enclosures for effective shielding, which significantly increases the structural mass of the system. One possible solution is to use precisely printed tungsten structures as radiation shielding. Tungsten, one of the most effective radiation shielding materials, has remarkable properties of density, robustness, chemical inertness, hardness, and thermal-resistivity (Lee 1981; Shemelya 2015). However, it is a significant challenge to manufacture designed tungsten structures due to such intrinsic properties, especially in electronic device fabrication. To overcome the challenge, we developed a new method to fabricate microstructures using with tungsten nanoparticles,

which is much easier to control and manufacture compared with bulk modality (Nersisyan 2005; Lei 2007). More importantly, nanoparticles could be formulated into nanoink with the help of appropriate additives (Ghosh 2015), which has enabled micro/nano manufacturing based on inkjet printing and e-jet printing.

In this paper, we reported the use of e-jet printing method to fabricate micro-scale radiation shielding structures of different shapes and thicknesses using tungsten nanoink. The printed patterns showed excellent morphology and resolution, as well as good absorption of X-ray radiation. To the best of our knowledge, the tungsten nanoink used in our e-jet printing is a novel formulation that has not been reported in the literature yet. This technology paves the way for manufacturing tungsten in micro/nano scale to generate customized patterns for radiation shielding and radiography in space mission, medical, and inspection applications.

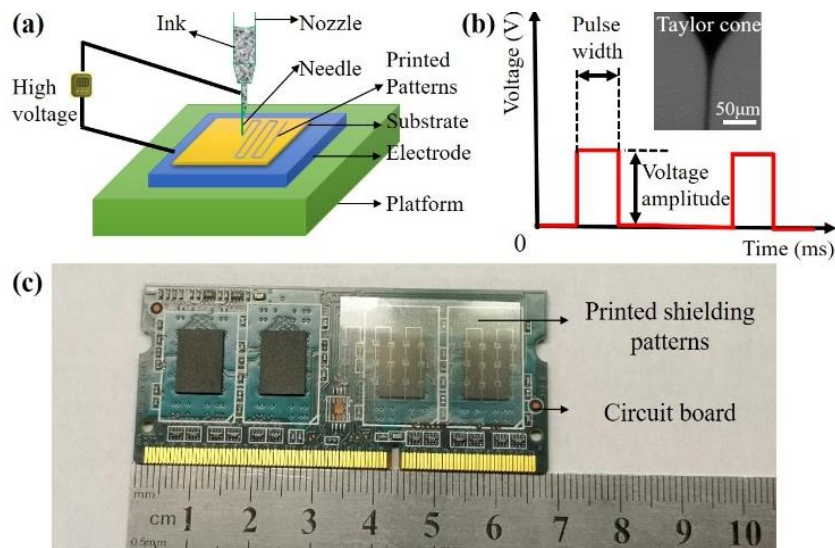


Figure 16. (a) Schematic of e-jet printing. A high voltage is applied between the needle and plate electrode. (b) Voltage modality and a machine vision of e-jet printing process. (c) A typical circuit board partially covered by printed patterns for the radiation shielding concepts

Methods and materials

E-jet printing system

To print the tungsten micro-patterns, an e-jet printing system was employed, shown in Figure 16(a). A plate electrode was set on the nano-positioning platform, which was controlled precisely by programs. A high voltage was applied between the plate electrode and needle, generating a large electric field to jet out droplets for depositions and printing. The ink was printed on the substrate attached on the plate electrode. With the moving of the platform, various patterns could be fabricated via given programs. There were several parameters affecting printing structures (Qin 2017), including needle size, stand-off distance, voltage modalities, and plotting speed. By optimizing these parameters, tungsten structures with different patterns were achieved. A charge coupled device (CCD) camera, as well as a lens system, were employed to monitor the needle and printed patterns (Qin 2017). The needle with diameter $\sim 30\mu\text{m}$ in the printing process was captured in Figure 16(b) with optical images by CCD. With the real-time testing, we could observe the printed pattern quality, Taylor cone, droplet size, and the changes of stand-off distance. After printing, a microscope (Hirox RH-2000) was employed to characterize the patterns and morphology of printed results. Many substrates were good candidates for e-jet printing, such as flexible films, which could be used for radiation shielding by covering on the circuit board. Figure 16(c) showed our printed metal patterns on flexible PET film covered on the circuit board. Different substrates have different surface roughness and surface energy, which leads to different wetting profile during the printing process. The 1.5 mm thick glass slides were used for calibration of the nanoink (Fisher Scientific, Waltham, MA). The printing on PET films and 36mm Kodak photo films have also been conducted to demonstrate the versatility of e-jet printing. This demonstrated that our method could be applied to common photography film that requires X-ray protection or marking (e.g., barcode) applications.

Nanoink fabrication

The raw materials used in the ink were tungsten nanoparticles with average particle size ~70nm (from US research nanomaterial, Inc), solvent Triethylene Glycol Monomethyl Ether (TGME, from Sigma-Aldrich), and Polyvinylpyrrolidone (PVP, from Sigma-Aldrich). TGME was applied as the solvent in nanoink, and PVP was used as the surfactant and thickener to facilitate the dispersing of nanoparticles in the solvent. The mass ratio of PVP to tungsten nanoparticles was 1:25, and the concentration of tungsten in TGME was 50% in mass. Because of heterogeneous-sized tungsten nanoparticles, PVPs with different molecular weights were employed as surfactants for better dispersion of tungsten nanoparticles, including 55K and 360K with a mass ratio of 1:1. In the study, fresh nanoinks with tungsten nanoparticles dispersed were prepared for printing after mixing. After the patterns were fabricated by e-jet printing, curing was not provided for most of the printed samples. Instead, the tungsten nanoink evaporates and dries on the substrate. The curing on printed parts does not influence the X-ray absorption performance because the presence of tungsten particles is the key to absorb X-ray energy under exposure to radiation. Currently, the fabrication is limited to 2D planar feature fabrication. A future research direction would be the fabrication of 3D tungsten structures, which will require the elevated temperature to increase evaporation rate and instant curing during printing.

Characterization

The commercial tungsten nanoparticles were characterized by the transmission electron microscopy (TEM, JEOL 2100), and energy dispersive spectroscopy (EDS, Oxford Aztec). In order to investigate the tungsten components contained in printed dots which were applied for radiation shielding, X-ray diffraction (XRD) with monochromatic $\text{CuK}\alpha$ radiation (Rigaku MiniFlex 600) was performed to identify the printed tungsten dots. The scan speed and step width were $10^\circ/\text{min}$ and 0.02° , respectively.

X-ray imaging of printed patterns

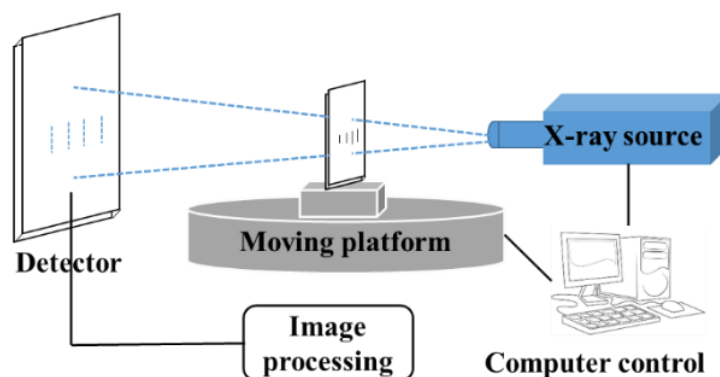


Figure 17. Schematic of the lab-built X-ray imaging system

The radiation characteristic of printed tungsten patterns was taken with a lab-built X-ray radiography system setup, including X-ray source, moving stage, a signal detector, control system, and analysis system, shown in Figure 17. A 50kV, 1000 μ A X-ray source was employed for scanning of printed tungsten samples, where the exposure time was 6500ms to get a high-quality image. The detector with resolution 3072 \times 3888 was used in the X-ray imaging system to obtain the X-ray transmitted data passing through the sample. Once the X-ray transmitted the sample with tungsten patterns, parts of them were absorbed, then the left arrived at the detector to form images with different grayscale values (John 1997).

Results and discussion

The EDS results (Figure 18(a)) indicate that the commercial nanoparticles are mainly pure tungsten. There is a small peak in 0.5keV, which suggests that oxidation exists in the nanoparticles. TEM image (Figure 18(b)) of tungsten nanoparticles used in the study shows a polydisperse size distribution of nanoparticles. The smallest dimension of tungsten nanoparticles is about 20nm. In order to uniformly disperse particles with such size range, two PVPs of different molecular weights (55K and 360K) were added into the tungsten nanoink to tune the rheology and stability of the ink formulation for e-jet printing.

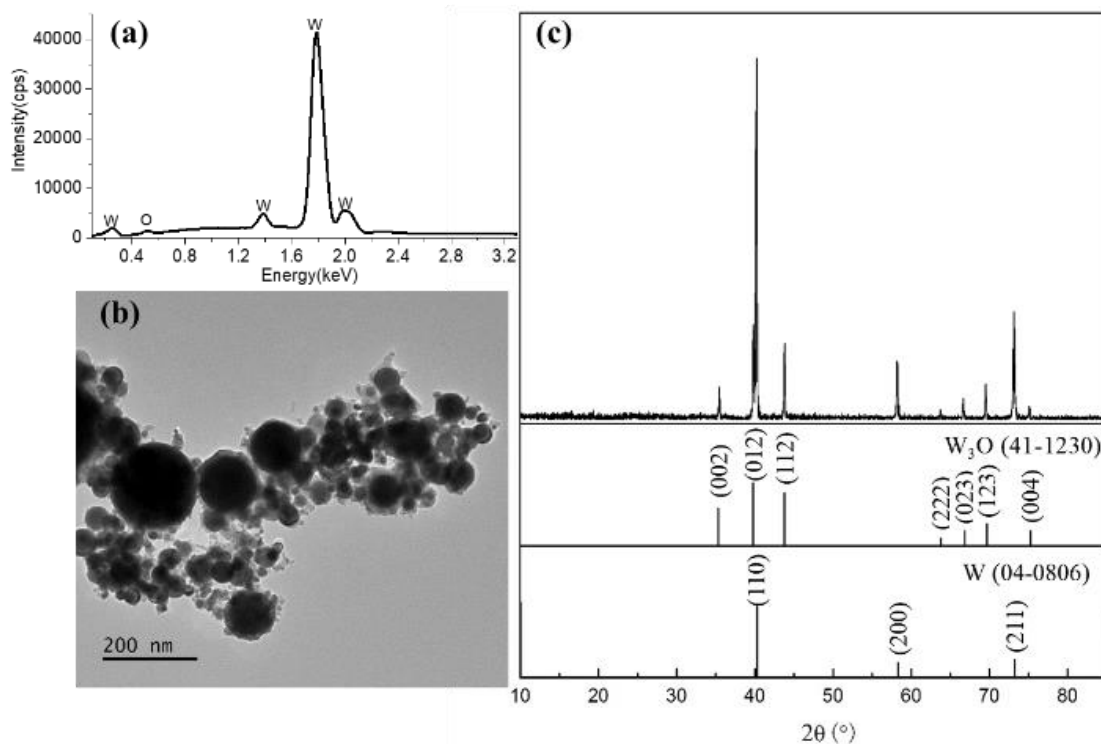


Figure 18. (a) Energy dispersive spectroscopy (EDS) and (b) Transmission electron microscopy (TEM) images of tungsten nanoparticles. (c) X-ray diffraction (XRD) results of printed tungsten dots

The XRD was taken to confirm the crystal structures of tungsten in the printed dots (Figure 18(c)). The XRD peaks demonstrate that the peaks with (110) (200) (211) have high intensities. The peak values match with tungsten peaks W (04-0806), which suggests our printed tungsten has a bcc crystalline structure (Ghosh 2015; Maille 2003). The XRD peaks corresponding to W_3O were also observed as (002) (012) (112) (222) (023) (123) (004), which further confirmed the oxidation states of tungsten nanoparticles in the nanoink. The XRD results strongly indicate that the printed tungsten is in the crystalline form, which can benefit the X-ray absorption analysis in the following part.

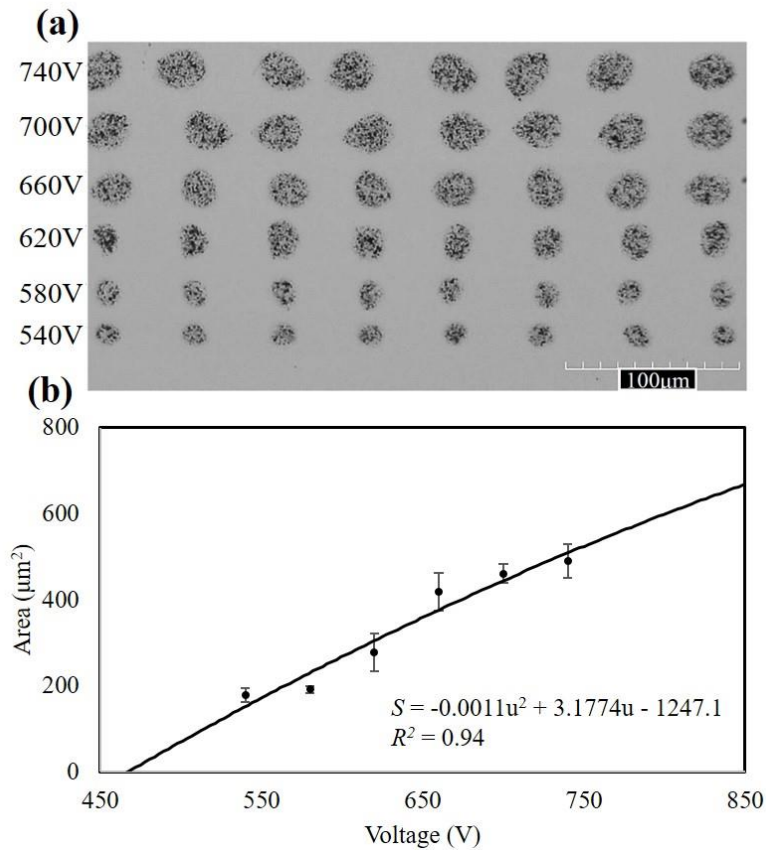


Figure 19. Printed tungsten dots with e-jet printing in different voltages. (a) Optical microscope image, (b) Dots area as a function of printing voltage

The mechanism of the e-jet printing process was extremely complicated and difficult to control, due to the facts that numerous variables are coupled with each other for the printing process (Qin 2007). Presented in this work, the control of needle dimension, stand-off distance, voltage amplitude, frequency, pulse width, and plotting speed will all affect printing quality of designed patterns. Different from thermal/acoustic pressure driven inkjet printing (Sirringhaus 2000), e-jet printing employs high voltages to drive the metal ink ejection, utilizing the electrical force working at Taylor cone mode, and achieve higher resolution. The changes of voltage modalities play a significant role in printed patterns morphology, especially the dimensions of the features. Figure 19(a) shows a variation of tungsten dots printed at different

printing voltages. An explicit size decrease can be observed with the reduction of voltage. With higher voltage, a large electric field force was applied to the droplet, resulting in the jet being ejected and printed onto the substrate. As the curve shown in Figure 19(b), higher voltage yielded dots with a larger size. The trend was fit linearly with the equation $S = -0.0011U^2 + 3.1774U - 1247.1$, where S is the dotted area in micrometer² and u is the voltage in volt, respectively. The area of the dot is determined by the volume of the droplet in e-jet printing, which indicates the gradual changes of droplet volume with altering voltage. Under constant needle diameter and stand-off distance, the accumulation of charges in Taylor cone increases with higher voltage, generating droplets which have increased volumes and higher speeds to the substrate. Dots with a larger size can also be printed. With a $\sim 30\mu\text{m}$ diameter needle, a small size dot with diameter $\sim 10\mu\text{m}$ can be printed, which serves as the prior control of e-jet printing by high voltage (Han 2018).

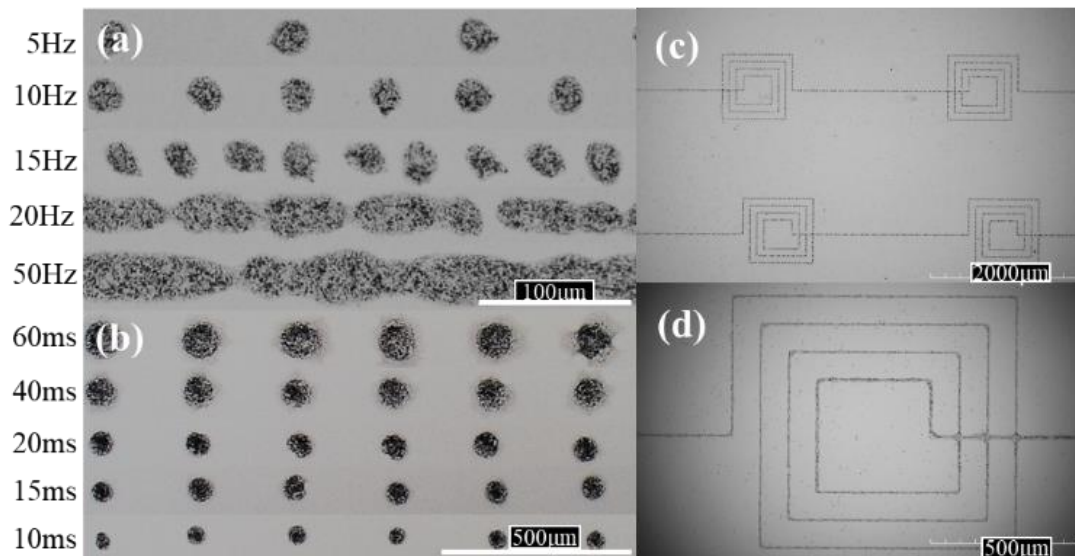


Figure 20. Optical microscope images of tungsten dots under different (a) Frequencies and (b) Pulse widths of high voltage; Optical microscope images of tungsten shaped lines with (c) Low and (d) Large magnification

The morphology of printed patterns is closely related to the printing parameters. Instead of using direct current (DC) voltage (Zou 2019) between electrode and needle which could generate many single-size dots, an amplified alternating current (AC) with variable voltage, frequency and pulse width was applied for printing in our study. Different parameters resulted in different dimensions of dots or lines. Figure 20 shows optical images of printed tungsten dots under various frequencies and pulse widths. With high frequency, the increase in jetting frequency and spray speed leads to closer separations between two adjacent droplets and line coalescence. The distance between two contiguous dots changed from $100\mu\text{m}$ at 5Hz to $31\mu\text{m}$ at 15Hz. Further increasing the frequency produced the dots overlapping with the previous ones, which eventually resulted in coupled dots and wide lines, as shown in Figure 20(a). The pulse width (Holtz 1992) is the open status of the voltage switch, which allows the supply of high voltage for printing. The length of pulse width affects the electrical field force of the ink, such that the dots can be printed in different sizes, as shown in Figure 20(b). The diameter of the dot decreases from $83\mu\text{m}$ to $33\mu\text{m}$ with a pulse width change from 60ms to 10ms. The dot sizes are much larger than those in Figure 20(a), since the pulse width of Figure 20(a) was tens of microseconds. Larger pulse width resulted in larger dot size. If the pulse width is too small, the nanoink could not come out from the needle due to the failure of nanoink forming the fine Taylor cone. With the selected parameters, group lines in patterns of excellent fidelity were acquired, as shown in Figure 20 (c) and (d). Because of AC voltage application, the droplet can be controlled precisely, which produces good patterns even in the turning corner. The line width is about $6.5\mu\text{m}$, shown in Figure 20(d), much smaller than the needle diameter $30\mu\text{m}$. It is the result of well-defined printing droplet generated by high voltage and optimized frequency (Mishra 2010) and speed (Phung 2017). However, there were still several imperfect dots at the cross-points of

two lines since the printed nanoinks did not dry immediately. The AC voltage used in e-jet printing provided a convenient adjusting method for generating different size and morphology dots or lines. As a proof of concept, the capability of patterning is demonstrated here, which can be further optimized for future applications in manufacturing radiation shielding components for electronics.

Several interesting patterns were obtained by altering printing parameters, as shown in Figure 21. Violent droplets flying behavior was observed when printing using DC voltage. For example, the patterns like tadpoles in Figure 21(a) were printed under a pre-programmed pattern shown as the dashed lines. The DC voltage was applied between the needle and electrode, and the nanoink came out consistently. We observed that due to charges in e-jetted droplets, plotting speed, and high viscosity of the ink, a disturbance was generated with the in-flight droplets. At a particular plotting speed, a small tip left behind the dot. Large pulse width with AC voltage can also lead to tips in the dots, shown in Figure 21(b). While the ink was not fresh (aged ink after several days), there were some random patterns emerging in the printing, seen in Figure 21(c). This could be due to the particle aggregation so that the nanoink was no longer homogeneous. Some particles and solvent came from the needle non-continuously, demonstrating electrospinning behavior with a high level of uncertainty. Some narrow lines, as well as large dots, could be generated. At this condition, when a high voltage applied, the irregular patterns were observed. Enlarged images show structures similar to diffusion-limited aggregation (Figure 21(d)) (Onses 2015). When the nanoink was not uniform and ejected randomly at high voltage, such random drops and curved lines occurred.

By adjustment pulse width, oscillate frequency and spacing, diameters of printed dots were precisely controlled by adjusting the pulsed signal for excitation. Printed line width was

controlled by cooperating with printing head moving velocity, excitation voltage, pulse width, and oscillate frequency (Nguyen 2009). Once the liquid ink was charged enough by the electrical potential to overcome the surface energy, a new surface will facilitate the resulting formation of the droplet. With controlled pulse width and amplified voltage, the electron prudential energy delivered to the ink liquid were controlled; therefore, a means of controlling droplet mass results in high printing quality (Zheng 2014). Simulation work on the droplet generation has been reported in e-jet printing (Pan 2019). There were several areas with a relatively large quantity of tungsten nanoink in Figure 21 (c) and (d). They were high tungsten density patterns and could play an important role in radiation shielding. Due to the complication of ink properties and interaction with electric fields, the overall mechanisms of pattern formation and line coalescence in Figure 21 have not been fully understood yet. A future research direction would be correlated with ink formulation and droplet dynamics under the electrical fields. More details of the relationship between tungsten pattern quality and printing parameters will be further investigated.

Generally, line patterns with 50-200nm thick have been obtained with e-jet printing after multi-layer stackup (Qin 2017). For better radiation shielding application of tungsten, multi-layer lines were also required and printed layer by layer. Figure 22(a) showed the optical image of printed multi-layer tungsten lines, where a round trip was designed to realize layer-by-layer printing. Since the nanoink did not solidify immediately during the printing process, there were some outflows of the line, leading to several bulge formation in multi-layer lines. When the printing layers increased to 50 layers, the solvent and tungsten regions were clearly observed in the magnified optical image Figure 22(c). The dark line represented the tungsten line as marked in the picture, while there were also some overflowing solvents with multi-layer printing. With a

3D imaging optical system, a general 3D picture was obtained in Figure 22(d). The thickness of the line was about $9.5\mu\text{m}$, which resulted from the multi-layer printing.

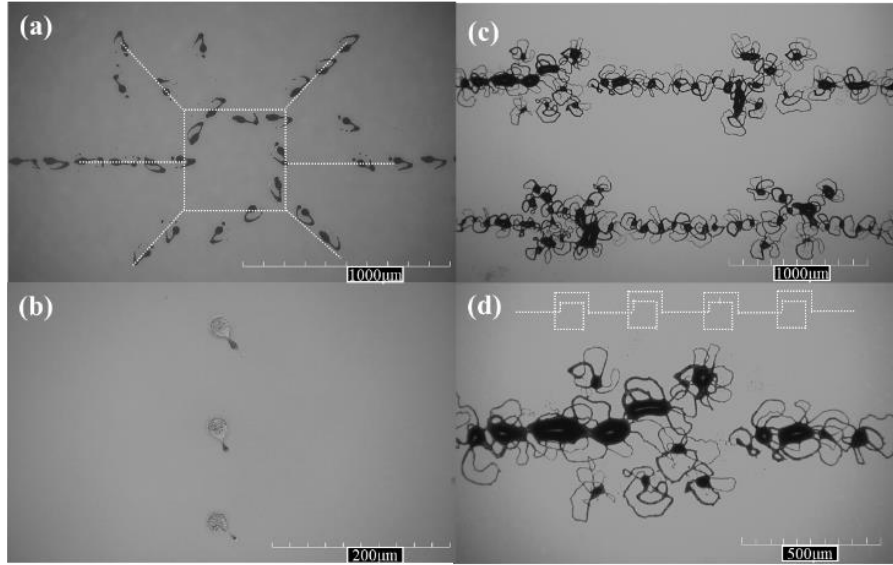


Figure 21. Optical microscope images of tungsten patterns at different conditions: (a) DC voltage and the dashed lines were the designed pattern; (b) Large pulse width with AC voltage; (c) and (d) are non-fresh ink with normal and high voltage at the designed patterns as dashed lines in inset. The dashed lines denote designed printing path

Figure 22(b) showed the X-ray radiography imaging results, where the designed patterns with 20 and 50 printed layers were observed. The pictures were analyzed by Matlab and X-ray absorption was calculated. In the study, a grayscale was used to estimate the absorption of X-ray. $G = I_z/I_0$, where G was the grayscale of printed tungsten patterns, I_z and I_0 was the gray value of the tungsten pattern at a thickness z and background of the sample, respectively. The gray value of each pixel of the patterned area and background by coordinate recognition was obtained, and the mean values of them were calculated. The calculated grayscale of the patterns in Figure 22(b) were 0.99 and 0.97 for the top (20layer) and bottom (50layer) pattern, respectively.

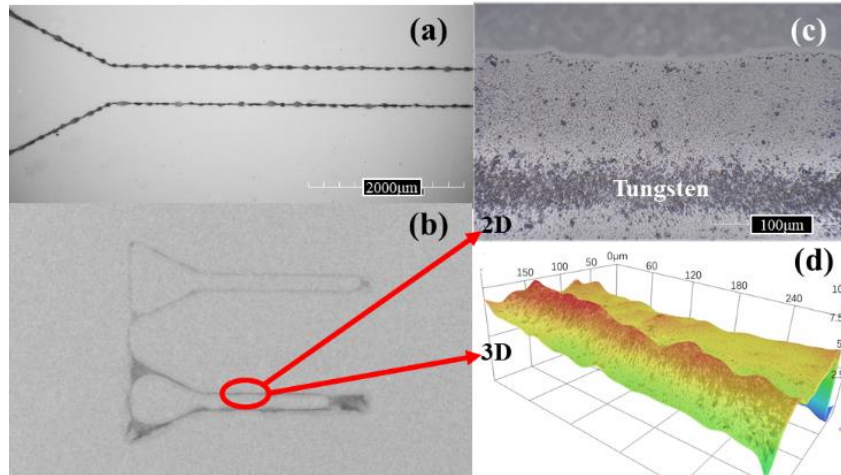


Figure 22. (a) Optical image; (b) X-ray radiography image of printed tungsten lines with 20 layers (top) and 50 layers (bottom); (c) and (d) are magnified 2D and 3D images of the 50 layers tungsten line, respectively

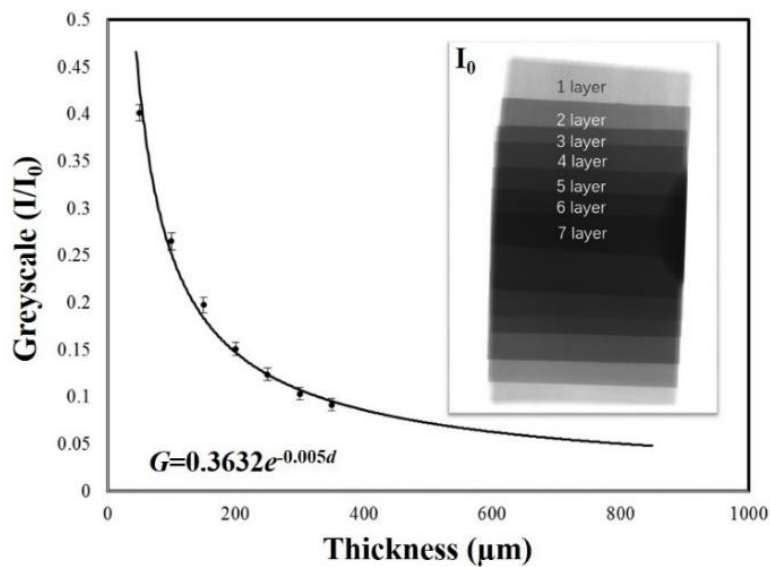


Figure 23. Grayscale of bulk tungsten sheet as a function of its thickness. The inset is an X-ray radiography image of tungsten sheets with different layers

The X-ray radiography patterns in the image were the area filled with printed tungsten nanoparticles rather than the solvent. The absorption efficiency was affected by tungsten atoms thickness and density (Zhou 2014), which was determined by line layers. In order to compare the

radiation shielding effect between bulk tungsten and nanoparticles, a group of standard bulk tungsten sheets (Eagle Alloys, Co.) was also used for X-ray radiation with the same system. The thickness of each sheet was 50 μm , and different layers were used to adjust various thickness, shown in the inset of Figure 23. Thus, the grayscale under different thickness tungsten sheets was calculated in Figure 23. The change rule was matched exponentially of the equation = $0.3632e - 0.005d$, where G was the calculated grayscale and d was the thickness of tungsten sheets, respectively.

Table 2. The comparison of grayscale between bulk and printed tungsten at the same thickness.

| Printed Lines | Thickness | Thickness | Grayscale Ratio | | Bulk Tungsten |
|----------------|----------------------|----------------------|-----------------|----------------|---------------|
| | Avg. / μm | Std. / μm | I_z/I_0 Avg. | I_z/I_0 Std. | I_z/I_0 |
| 50-Layer Print | 12.5329 | 0.1154 | 0.9700 | 0.0031 | 0.4333 |
| 20-Layer Print | 3.6071 | 0.1642 | 0.9913 | 0.0008 | 0.3461 |
| 1-Layer Print | 0.0971 | 0.0269 | 0.9917 | 0.0007 | N/A |

The printed lines consist of tungsten nanoparticles. The presence of tungsten function as attenuation elements, but attenuation effects cannot be as good as bulk tungsten due to porosity existing in the printed structures. The study is in the range of micro/nano scale detection and X-ray intensity is evaluated by the grayscale of the resulting images. 50-layer, 20-layer and 1-layer samples were printed three times each. The thickness of each sample was measured five times to calculate the average thickness and its standard deviation for multi-layer printing. The acceleration voltage was set at 50 kV considering wide linear mass attenuation response (Hubbell 2004) and sufficient energy for high resolution X-ray contrast at micro-scale (20 μm). The bulk tungsten at the same thickness of printed sample was calculated using the prediction curve in Figure 23. In Table 2, with different printed thickness, the grayscale ratios of printed tungsten comparing to bulk tungsten required to provide the same X-ray shielding efficiency were calculated. It shows that as the printed tungsten thickness increase, the shielding efficiency

is close to bulk tungsten sheet. The grayscale of 20-Layer printed lines was 2.77 times smaller than bulk tungsten sheet at the same thickness, and 2.26 times smaller for 50-Layer printed lines.

The small grayscale means low transmittance and high blocking rate of an X-ray through the samples. The grayscale results indicate that the printed tungsten lines have good performance of X-ray radiation absorption, which is about 1/3 absorptivity of bulk tungsten. The grayscale is affected by both particle density and layer width. More radiation absorption and patterns of lower grayscale values can be obtained when there are more tungsten layers and higher density of tungsten on the substrate. The X-ray radiography imaging results indicate that our printed tungsten lines can indeed prevent X-ray radiation in high efficiency. However, it was still lower than bulk materials, most likely due to the packing density of tungsten nanoparticles.

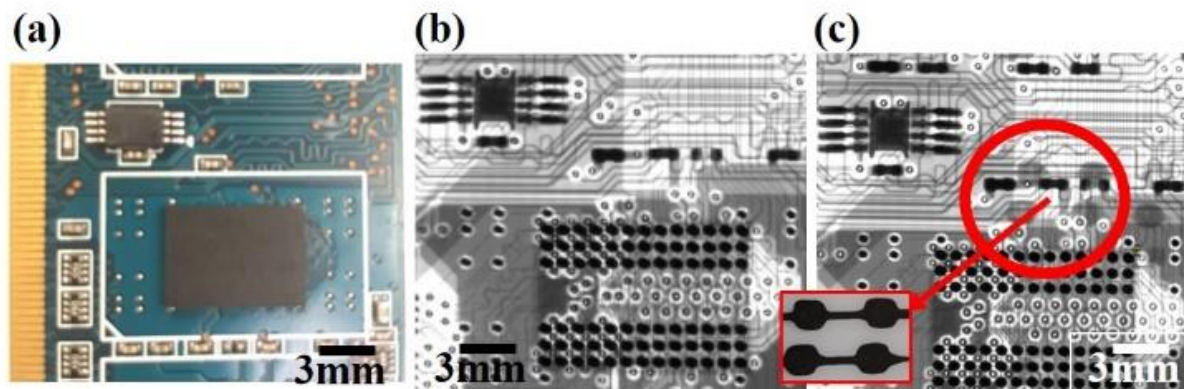


Figure 24. (a) Optical image of circuit board. (b) X-ray radiography image of the circuit board .

(c) Printed capacitor and cover patterns on the circuit board under X-ray imaging

Figure 24(a) presented the physical appearance of a circuit board from a central server. Flexible substrate (PET film) with printed tungsten ink was placed upon the circuit board to mimic two scenarios: 1) a shielding, and 2) marker in CT applications. Before the printed pattern was placed on top of the board, we can observe the X-ray image under radiation in Figure 24(b). After the tungsten pattern was placed on it, four pad patterns could be clearly detected in Figure

24(c). In this way, the electronic components in the circuit board (e.g., screen printed conductive lines) were covered by the tungsten components, such that shielding function can be achieved or X-ray marker (e.g., barcodes) can be detected. The micro/nano e-jet printing based strategy can create radiation shielding enclosures for electronics in a highly tailorable manner. More importantly, our method can potentially enhance the radiation attenuation effectiveness with a lower structural weight.

Conclusion

We have successfully developed a new tungsten nanoink for e-jet printing and demonstrated different printing patterns, including dots and lines. By adjusting the printing parameters (e.g., voltage, frequency, pulse width, and ink formulation), the dimension and morphology of printed dots can be precisely controlled. The printed tungsten patterns exhibited excellent absorption of X-ray radiation under direct exposure. With the same thickness, printed lines showed about 1/3 absorptivity of X-ray radiation of bulk tungsten, exhibiting good potential applications for radiation-shielding of electronic components. This work presented a novel and convenient path to manufacturing radiation-shielding patterns with tungsten nanoparticles, which may find useful applications in the development of micro-nano electronic device for shielding protection.

References

- An, B. W., Kim, K., Kim, M., Kim, S. Y., Hur, S. H. & Park, J. U., 2015. Direct Printing of Reduced Graphene Oxide on Planar or Highly Curved Surfaces with High Resolutions Using Electrohydrodynamics. *Small*, 11, pp. 2263-2268.
- Brossard, F. S. F., Pecunia, V., Ramsay, A. J., Griffiths, J. P., Hugues, M. & Siringhaus, H., 2017. Inkjet-Printed Nanocavities on a Photonic Crystal. *Template Adv Mater*, 29, pp. 1704425.
- Cui, Z., Han, Y., Huang, Q., Dong, J. & Zhu, Y., 2018. Electrohydrodynamic printing of silver nanowires for flexible and stretchable electronics. *Nanoscale*, 10, pp. 6806-6811.

- Ghosh, S., Khamarui, S., Saha, M. & De, S. K., 2015. Fabrication of tungsten nanocrystals and silver-tungsten nanonets: a potent reductive catalyst. *Rsc Adv*, 5, pp. 38971-38976.
- Han, Y. & Dong, J., 2018. Fabrication of self-recoverable flexible and stretchable electronic devices. *J. Manuf. Syst*, 48, pp. 24-29.
- Holtz, J., 1992. Pulsewidth modulation-a survey. *IEEE T. Ind. Electron*, 39, pp. 410-420.
- Hubbell, J. H., 2004. <https://physics.nist.gov/PhysRefData/XrayMassCoef/ElemTab/z74.html>.
- Jang, Y., Kim, J. & Byun, D., 2013. Invisible metal-grid transparent electrode prepared by electrohydrodynamic (EHD) jet printing. *J. Phys. D Appl. Phys*, 46, pp. 155103.
- Jeong, Y. J., Lee, X., Bae, J., Jang, J., Joo, S. W., Lim, S., Kim, S. H. & Park, C. E., 2016. Direct patterning of conductive carbon nanotube/polystyrene sulfonate composites via electrohydrodynamic jet printing for use in organic field-effect transistors. *J. Mater. Chem. C*, 4, pp. 4912-4919.
- John, M. & Boonea, J. A. S., 1997. An accurate method for computer-generating tungsten anode x-ray spectra from 30 to 140 kV. *Med. Phys*, 25, pp. 1661-1670.
- Kim, B. H., 2015. High-Resolution Patterns of Quantum Dots Formed by Electrohydrodynamic Jet Printing for Light-Emitting Diodes. *Nano Lett*, 15, pp. 969-973.
- Kim, K., Kim, G., Lee, B. R., Ji, S., Kim, S. Y., An, B. W., Song, M. H. & Park, J. U., 2015. High-resolution electrohydrodynamic jet printing of small-molecule organic light-emitting diodes. *Nanoscale*, 7, pp. 13410-13415.
- Lee, D. Y., Shin, Y. S., Park, S. E., Yu, T. U. & Hwang, J., 2007. Electrohydrodynamic printing of silver nanoparticles by using a focused nanocolloid jet. *Appl. Phys. Lett*, 90, pp. 081905.
- Lee, P. A., Citrin, P. H., Eisenberger, P. & Kincaid, B. M., 1981. Extended X-ray Absorption Fine-Structure - Its Strengths and Limitations as a Structural Tool. *Rev. Mod. Phys*, 53, pp. 769-806.
- Lei, H., Tang, Y. J., Wei, J. J., Li, J., Li, X. B. & Shi, H. L., 2007. Synthesis of tungsten nanoparticles by sonoelectrochemistry. *Ultrasound. Sonochem*, 14, pp. 81-83.
- Li, X., Lee, G. S., Park, S. H., Kong, H., An, T. K. & Kim, S. H., 2018. Direct writing of silver nanowire electrodes via dragging mode electrohydrodynamic jet printing for organic thin film transistors. *Org. Electron*, 62, pp. 357-365.
- Li, X., Park, H., Lee, M. H., Hwang, B., Kim, S. H. & Lim, S., 2018. High resolution patterning of Ag nanowire flexible transparent electrode via electrohydrodynamic jet printing of acrylic polymer-silicate nanoparticle composite overcoating layer. *Org. Electron*, 62, pp. 400-406.

- Maillé, L. C., Sant, C., Le Paven-Thivet, C., Legrand-Buscema, C. & Garnier, P., 2003. Structure and morphological study of nanometer W and W3O thin films. *Thin Solid Films*, 428, pp. 237-241.
- Mishra, S., Barton, K. L., Alleyne, A. G., Ferreira, P. M. & Rogers, J. A., 2010. High-speed and drop-on-demand printing with a pulsed electrohydrodynamic jet. *Journal of Micromech & Microeng*, 20, pp. 095026.
- Nersisyan, H. H., Lee, J. H. & Won, C. W., 2005. A study of tungsten nanopowder formation by self-propagating high-temperature synthesis *Combust. Flame*, 142, pp. 241-248.
- Nguyen., V. D. & Byun, D., 2009. Mechanism of electrohydrodynamic printing based on ac voltage without a nozzle electrode. *Appl. Phys. Lett*, 94(17), pp. 173509.
- Pan, Y. & Zeng, L., 2019. Simulation and Validation of Droplet Generation Process for Revealing Three Design Constraints in Electrohydrodynamic Jet Printing. *Micromachines*, 10(2), pp. 94.
- Park, J. U., Hardy, M., Kang, S. J., Barton, K., Adair, K., Mukhopadhyay, D. K., Lee, C. Y., Strano, M. S., Alleyne, A. G., Georgiadis, J. G., Ferreira, P. M. & Rogers, J. A., 2007. High-resolution electrohydrodynamic jet printing. *Nat. Mater*, 6, pp. 782-789.
- Phung, T. H., Kim, S. & Kwon, K. S., 2017. A high speed electrohydrodynamic (EHD) jet printing method for line printing. *Journal of Micromech. Microeng*, 27, pp. 095003.
- Prasetyo, F. D., Yudistira, H. T., Nguyen, V. D. & Byun, D., 2013. Ag dot morphologies printed using electrohydrodynamic (EHD) jet printing based on a drop-on-demand (DOD) operation. *J. Micromech. Microeng*, 23, pp. 095028.
- Qin, H. T., Cai, Y., Dong, J. Y. & Lee, Y. S., 2017. Direct printing of capacitive touch sensors on flexible substrates by additive e-jet printing with silver nanoinks. *Journal of Manuf. Science*, 139, pp. 031011.
- Qin, H. T., Dong, J. Y. & Lee, Y. S., 2017. AC-pulse modulated electrohydrodynamic jet printing and electroless copper deposition for conductive microscale patterning on flexible insulating substrates *Robot. Cim-Int. Manuf*, 43, pp. 179-187.
- Qin, H. T., Wei, C., Dong, J. Y. & Lee, Y. S., 2017. Direct Printing and Electrical Characterization of Conductive Micro-Silver Tracks by Alternating Current-Pulse Modulated Electrohydrodynamic Jet Printing *J. Manuf. Sci E-T Asme*, 139, pp. 021008.
- Shemelya, C. M., Rivera, A., Perez, A. T., Rocha, C., Liang, M., Yu, X., Kief, C., Alexander, D., Stegeman, J. & Xin, H. J., 2015. Mechanical, electromagnetic, and X-ray shielding characterization of a 3D printable tungsten-polycarbonate polymer matrix composite for space-based applications *J. Elect. Mater*, 44, pp. 2598-2607.

- Sirringhaus, H., Kawase, T., Friend, R., Shimoda, T., Inbasekaran, M., Wu, W. & Woo, E. J. S., 2000. High-resolution inkjet printing of all-polymer transistor circuits. *Science*, 290, pp. 2123-2126.
- Tekin, E., Wijlaars, H., Holder, E., Egbe, D. A. M. & Schubert, U. S., 2006. Film thickness dependency of the emission colors of PPE-PPVs in inkjet printed libraries. *J. Mater. Chem*, 16, pp. 4294-4298.
- Witten, T. & Sander, L. M. J., 1981. Diffusion-limited aggregation, a kinetic critical phenomenon *Phys. Rev. Lett*, 47, pp. 1400-1403.
- Yudistira, H. T., Tenggara, A. P., Nguyen, V. D., Kim, T. T., Prasetyo, F. D., Choi, C. G., Choi, M. & Byun, D., 2013. Fabrication of terahertz metamaterial with high refractive index using high-resolution electrohydrodynamic jet printing. *Appl. Phys. Lett*, 103, pp. 211106.
- Zheng, G. F., Liu, H. Y., Xu, R., Wang, X., Liu, J., Wang, H. & Sun, D. H., 2014. Alternating current electrohydrodynamic printing of microdroplets. *Journal of Nanomater*, pp. 1-7.
- Zhou, Z., Kong, B., Yu, C., Shi, X., Wang, M., Liu, W., Sun, Y., Zhang, Y., Yang, H. & Yang, S., 2014. Tungsten oxide nanorods: an efficient nanoplatform for tumor CT imaging and photothermal therapy. *Sci. Rep*, 4, pp. 3653.
- Zou, W. H., Yu, H. B., Zhou, P. L. & Liu, L. Q., 2019. Tip-assisted electrohydrodynamic jet printing for high-resolution microdroplet deposition *Mater. Design*, 166, pp. 107609.

CHAPTER 5. IN-SITU REAL-TIME CHARACTERIZATION OF MICRO-FILAMENTS FOR ELECTROHYDRODYNAMIC INK-JET PRINTING USING MACHINE VISION

Authors and Affiliations

Modified from a manuscript to be published in *Procedia Manufacturing*. This research work is published by Rahul Singh, Xiao Zhang, Yongxin Chen, Junxin Zheng, and Hantang Qin in the *Procedia Manufacturing* (2018), 17 (2018): 45-52.

Rahul Singh was a Ph.D. student in the electrical engineering department at Iowa State University. Xiao Zhang and Hantang Qin are from the Industrial and Manufacturing Systems Engineering Department at Iowa State University. Dr. Yongxin Chen is from the Electrical Engineering Department at Iowa State University. Dr. Junxin Zheng is from the Construction and Environment Engineering Department.

The idea is proposed by our research group of monitoring the e-jet printing process. I am leading the e-jet printing experiment design, image data collection, part of the data analysis and writing. Rahul has contributed to the image data processing and analysis in the results section. I want to acknowledge my advisor, Dr. Hantang Qin, Dr. Yongxin Chen, and Dr. Junxin Zheng's support throughout this research work.

Abstract

Electrohydrodynamic ink-jet printing (e-jet printing) is one of micro/nano scale 3D printing techniques that automatically deposit functional materials to form 3D structures on the substrate. Unlike traditional thermal or acoustic inkjet printing, e-jet printing utilizes high electrical forces that enable the ink to overcome surface tension at the tip of micro needles. The filaments/droplets coming out from the needle have dimensions much smaller than the dimensions of the nozzle, thus printing geometries in micro and nano scale. Process parameters in e-jet printing could affect the final quality attributes of fabricated constructs. Currently, assessment of these critical geometries and attributes must be performed offline using optical microscopy or scanning electron microscopy. This drawback affected the efficiency of micro/nano printing from translation into industrial practice. The research in this paper focused

on fundamental research to enable in-situ monitoring of e-jet printing using a real-time image characterization technique. In conclusion, the study in this paper investigated using machine vision for real-time monitoring of micro scale 3D printing. The method worked well for characterization of micro-filaments, and may be further implemented into feedback control system of complicated e-jet printing. However, the optical machine vision was limited to micro scale detection. One of the future research topic is to develop nano scale in-situ characterization mechanism for e-jet printing.

Introduction

With the rapid development of the additive manufacturing (AM) industry, highly flexible, accurate, and low-cost designs can better satisfy the future requirements of the product which are diverse, of high quality, and cheap. E-jet printing is one branch of the promising additive manufacturing (AM) technology which has the potential to revolutionize the AM industry (Qin 2017). A variety of applications, from flexible electronics to high resolution biosensors, can be fabricated using e-jet printing (Sutanto 2014). Conventional ink-jet printing faces multiple challenges in high resolution surface printing because the dimension of printed patterns is limited to tens or even hundreds of micrometers for reliable ink-jet printing (Kuang 2014). E-jet printing technique applies electrical field to force conductive material out the nozzle to fabricate even smaller characteristic on substrate (Onses 2015; Park 2007; Kim 2015; Wei 2013). In comparison, e-jet printing can achieve the printed feature size of as low as hundreds of nanometers (Kim 2015; Rogers 2010; Park 2010).

Although e-jet printing has the ability to fabricate high resolution patterns, automation of e-jet printing process has not been realized yet. Therefore, the printed parts are often uneven and inaccurate. Moreover, multiple challenges such as inconsistency in the printed material, process modeling, and process control, have hindered e-jet printing to be accepted by a wider range of

corporations in the AM industry (Mani 2014). Multiple quality control systems for different manufacturing methods have been developed in the last decade. For example, ac-pulse modulated e-jet printing solved the slow charge decay rate of the substrate problem to achieve high resolution continuous features (Wei 2014). Process monitoring systems are well developed in the subtractive manufacturing, however, AM being a relatively new technology lacks such well-developed methods for process monitoring and control. Everton et al. reported that the in-situ inspection approach can be utilized in the AM method (Everton 2016). In the research, the infrared temperature sensor detection helps to monitor the fused filament fabrication failure in real-time and the required adjustment can be made to correct it (Rao 2015). SK Everton et al. found that metal AM with in-situ method was widely used in process monitoring control (Everton 2016).

In order to realize the automated in-situ control over e-jet printing process, optical system is a potential solution to ensure the quality control. There exist multiple optical sensing techniques including time of flight techniques, interferometric techniques, and diffraction techniques (Strand 1985). The optical system captures numerous images of the filament and printing parts during the printing process and subsequently, these images are used to extract useful information about the filament. This information is fed to the feedback control system and the necessary tuning is made. In the real-time feedback system, the main obstacle is the timely processing of the data as there are 160 images captured every second which means efficient algorithms are sought that can match the time constrain. Notably, Nakabo et al. developed 1 ms visual feedback system based on massively parallel processing as well as fast image processing algorithms (Nakabo 1997). Moreover, Barton et al. through the adjustment of the e-jet printing system, used sensing and feedback system to get high resolution printed parts (Barton 2011).

Multiple challenges are faced in processing of images due to the background noise in form of the printed material and other sources such as dust particles. In order to extract the filament information, such as diameter and tilt-angle, there are two main methods: converting the images into binary form or applying edge detection algorithm to get the corresponding edge images. To convert the images into binary form, the main challenge is the variations in the binary threshold values due to the variations in the lighting and changing position of the nozzle relative to the edges of the substrate. Yi et al. optimized the procedure to decide the light source position and get a good measure performance (Yi 1995). Tsugawa et al. found the configurations, driving control systems, and the machine vision systems contribute to the whole structure of closed-loop intelligent system (Tsugawa 1994).

In this research, the optical system is utilized to collect the material flow information in order to monitor the surface quality of the parts being printed. The material flow, in form of the filament, can indicate the defects and material property in the printing parts. The complete machine vision system as well as the detailed mechanism of e-jet printing is introduced in Section 2. In order to prove the effectiveness of the real-time system, experiments of the e-jet in-situ system were conducted. In section 3, image processing algorithm is described followed by the experimental results. It is worth noting that extra benefits will be obtained from the data collected during the process that enables us to reconstruct the 3D model of the printing parts. In the future, the modeling technology may also be used in the e-jet simulation software for the non-destructive evaluation of the printed part which can help the factory to save time and cut cost. This work is an effort in the direction of providing a more reliable and controllable e-jet printing system.

Methodology

Machine vision theory

From the appearance of the machine vision system, it is widely applied in manufacturing industry. In e-jet printing process, prediction of all the situations by calculation based on material, mechanical, and electrical theories is difficult. Machine vision system is an important approach to stabilize and control over the system in a random and dynamic environment (Lee 2002). Even if one can predict the manufacturing process, there are still system and accidental errors. The machine vision system can contribute to spot the anomaly during printing process, upgrade the traditional manual operation to automatic operation, and enable the measurements to be flexible and accurate (Kurada 1997). There are many applications for machine vision system: quality and safety detection, process automation, classification and sorting (Chen 2002). Quality is one of the most important characteristics of a success product. Surface roughness detection can help improve the quality of the product, machine vision system can evaluate and facilitate the measurement through non-contact image processing software (Shahabi 2010). Automation helps to cut the cost, stabilize the quality, and reduce the labor. Machine vision assisted algorithms can automatically accomplish the analysis and the correct identification rate is rather high (Choi 2015). Meanwhile, constant monitoring also helps to control the quality of product. Excessive tool wear and abnormal tool condition will decrease the accuracy of the parts during micromachining process, a machine vision system was created to monitor and control the quality of the part (Dai 2017). In industry, the versatility is important for a variety of products to be manufactured, the machine vision system has been tested for a satisfactory result (Yachida 1997). Overall, the integration of vision system over ink-jet printer simplifies the printing process, improves the accuracy of part, cuts the cost, and makes this technology flexible (Sitthi-Amorn 2015).

However, the benefits of machine vision system accomplishes with difficulties. Harsh environment, such as the external illumination (Berger 2016), poses severe influence on the machine vision system. To monitor the printing process involving pattern of very small dimension is a great challenge. Feature of the products can be used for identification, and thus the recognition accuracy rate can be raised (Luo 1999). The machine vision system can work on multi features to investigate the quality and result in 100% yield rate (Abdulah 2006). Threshold can be used to divide the product into several grades to evaluate the quality is effective (Heinemann 1994). Since in real-time e-jet printing, camera can only achieve two-dimensional image, computer vision system has been proven to be able to correlate two-dimensional images with three dimensional objects (Lowe 1987). Therefore, three dimensional object can be constructed through machine vision system. In this paper, we aim to apply machine vision system to inspect and control the e-jet printing production. Also, the machine vision system will help to reconstruct 3D model for the nondestructive evaluation of e-jet printing parts.

Experiment setup

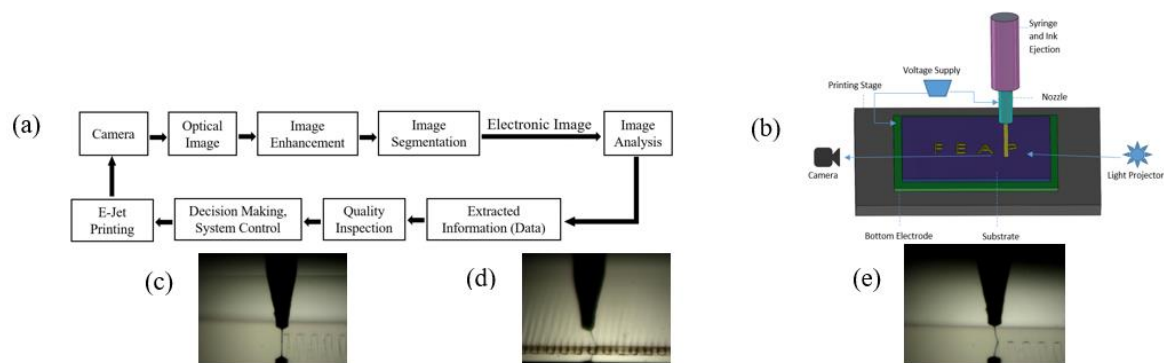


Figure 25. (a) Mechanism of image processing; (b) System setup; (c) Working condition; (d) Multi-layer printing; (e) Different orientations

With the development of machine vision monitoring system, adoption of e-jet printing can be greatly promoted in the AM industry. The automation of this system is key to improve the

quality of the printed product. One way to capture the surface roughness of the product is to capture the real-time image. With high speed camera, we can set the camera to a fixed position where it is available to take picture during the printing. However, taking picture is the first step for the establishment of the system. Then, we need to process the picture. At the same time, the feedback system will analysis the information captured by the camera and calibrate the printer's parameter to optimize the printing process. With this system, the e-jet printing process is automatic and flexible. The feedback system can not only automatically help to improve the quality of the printing product but also the engineer to set the program to control the system. What's more, for quality analysis, the final dimensional parameter of the printing part is required most of the time by engineer. By collecting the images of the whole process, we are able to use those images to reshape the real printed shape and roughness of the part.

Figure 25(a) introduces the basic principle and mechanism of the vision-based monitoring system. E-jet printer fabricates micro/nano meter scale features during printing process which is detected by a CMOS camera with a high magnification zoom lens. The camera captures images at a speed of 168 frames per second and subsequently, image processing algorithms are utilized to extract the dimensional parameters of filaments recorded in real time. The information extracted is then fed to the control system that calibrates the parameters of the e-jet printer to maintain a uniform diameter of the filament. Additionally, the images captured can be used to reconstruct 3D models of the printed part. The E-jet printer set-up is shown in Figure 25(b). Figure 25(c) shows an image of e-jet printing in a typical working condition, in this system images which are associated without too much noises can be easily processed. However, the captured images are not always perfect as shown in Figure 25(c). There are also bad images like Figure 25(d): multi-layer printing and Figure 25(e): different orientations. Not only the

images with too much noise are difficult to analyze, there are also images which are tricky to set up a threshold for binarization of images. In the following section, the algorithm for image processing are presented to measure image parameters under sophisticated situations

Processing algorithm and results

Image analysis

Figure 26 (a) shows a typical real-time image to be processed. As can be observed, two main difficulties arise which prevent accurate measurements of the filament properties such as diameter and tilt-angle. The first difficulty is the background noise in form of the printed material and the second difficulty is the image quality in terms of the number of pixels representing the filament in the image.

If we try to threshold the image using Otsu's method (Otsu 1979) without any preprocessing, we obtain the binary image as shown in Figure 26 (b). It can be observed that the filament information is not captured in the binary image. Moreover, if we apply Canny edge detection algorithm (Canny 1986), we obtain the image shown in Figure 26 (c), which is also not very useful to extract the required information about the filament.

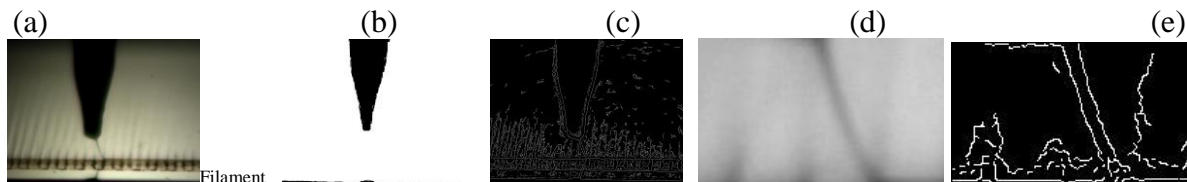


Figure 26. (a) Typical image to be processed; (b) Binary image obtained using Otsu's method; (c) Edge image using Canny edge detector; (d) Typical cropped image; (e) Edge image using Canny edge detector

We also performed the edge detection and thresholding operations on the cropped image containing only the filament part. The results are shown in Figure 26 (d) and (e). It can be

observed that the edge image is still not appropriate for diameter and tilt-angle calculations due to the unwanted noise.

The procedure for the diameter and tilt-angle calculation is depicted in Figure 28. Figure 28(a) shows a typical edge image of the filament obtained using Canny edge detector. For computation of tilt-angle and diameter of the filament, the edge image can be approximated as the image shown in Figure 28(b).

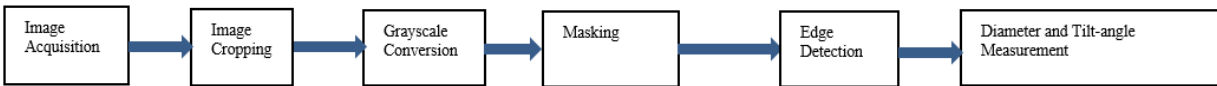


Figure 27. Proposed algorithm for information extraction from images



Figure 28. (a) A typical edge image of the tilted filament; (b) Approximate edge image; (c) Diameter and tilt-angle calculations; (d) Piecewise approximate edge image

Diameters and tilt-angle calculations are illustrated in Figure 28(c). The tilt-angle θ is measured with respect to the negative vertical direction and can be found using

$$\theta = \arctan(w / h) \quad (1)$$

where w and h are measured in terms of number of pixels. Moreover, the diameter d can be computed as

$$d = x * \cos(\theta) \quad (2)$$

where θ is the tilt-angle given by Equation (1) and x is the average number of pixel between two white pixels measured along the horizontal direction. For better accuracy, the edge

image can also be approximated as shown in Fig. 4(d), where the edge image is broken into three pieces. We can compute the diameters and tilt-angles for each of the three segments and then find the average angle and diameter. Note that increasing the number of pieces (segments) in the edge image will further increase the accuracy of diameter and tilt-angle calculations.

Results and discussion

In this section, the image processing results for multiple scenarios are presented. We have used MATLAB for the processing of images. The scenarios considered in our experiments are: (1) normal printing, (2) change of filament dimensions, (3) tilted micro-filament, and (4) multi-layer printing. Representative images for each of these scenarios are shown in Figure 29. The pixel pitch of the camera set up is $4.8\mu\text{m} \times 4.8\mu\text{m}$. First, we present the results which contain the processed images for each scenario and then tabulate the diameter and tilt-angle calculations in Table 3.



Figure 29. Representative images for different scenarios: (a) Normal printing (Scenario 1); (b) Change of filament dimensions (Scenario 2), (c) Tilted micro-filament (Scenario 3); (d) Multi-layer printing (Scenario 4)

Scenario 1: normal printing. One representative image for this scenario is shown in Figure 29(a) and image processing in the first row of Figure 30. This is a relatively simple scenario where the tilt-angle is zero and there is not a significant noise in form of the printed material. First, the image is cropped and converted to grayscale as shown in Fig. 6 column (a). Then the image is masked using a mask shown in Figure 30 column (b) and the resulting masked image is shown in Figure 30 column (c). When we apply Canny edge detection algorithm in the

ROI represented by the mask, the resulting edge image is shown in Figure 30 column (d), which can be used for diameter and tilt-angle calculations of the filament.

Scenario 2: change of filament dimensions. When the voltage is increased during printing process, the dimensions of the filament also increases. A representative image for this scenario is shown in Figure 30(b). The processed images for this scenario, the grayscale cropped image, the masked image, and the edge image are shown in Fig. 6 second row.

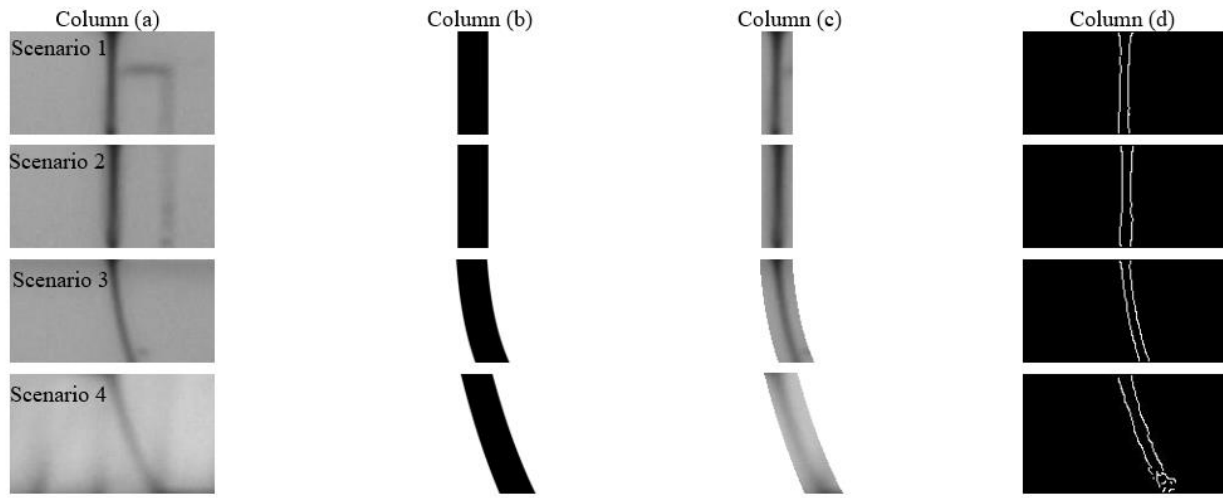


Figure 30. Scenario 1-4: (a) Cropped grayscale image; (b) The mask; (c) Masked image; (d) Edge image

Table 3. Diameter and tilt-angle for scenarios 1-4

| | Tilt-angle (degrees) | Diameter (pixels) | Diameter (μm) |
|---|----------------------|-------------------|----------------------------|
| 1 | 0 | 7.5422 | 36.2026 |
| 2 | 0 | 8.2530 | 39.6144 |
| 3 | 10.5392 | 7.0122 | 33.6586 |
| 4 | 20.8068 | 9.2416 | 44.3597 |

Scenario 3: tilted micro-filament. A representative image for this tilted filament scenario is shown in Figure 30(c). As opposed to the vertical filament in Scenarios 1 and 2, the filament in most of the images is tilted from the vertical direction due to the movement of the nozzle as the ink comes out. When the ink makes contact with the substrate, the filament in the air is lagged and dragged as the movement of the nozzle continues. The tilt-angle of the filament is an

important parameter because it might affect the printing process at different working speeds. The tilt-angle is also used to compute the diameter of the filament from the width of the tilted filament along the horizontal direction.

Scenario 4: multi-layer printing. As the printing continues, multiple layers of the printed material are also captured in the image. A representative image for this scenario is shown in Figure 30(d). In this scenario, the printed material in the image imposes a great challenge in extracting the filament information. The masking of the cropped grayscale image plays a crucial part by removing most of the background noise in form of the already printed material. The filament part of the image is extracted using the mask shown in Figure 30 column (b). The resulting masked image is shown in Figure 30 column (c). The resulting edge image after Canny algorithm applied in the ROI represented by the mask is shown in Figure 30 column (d), which is used for the diameter and tilt-angle calculations of the filament. An image of a human hair captured by our new camera set up is shown in Figure 31(a). The corresponding edge image after the masking operation is shown in Figure 31(d). The hair diameter is represented by almost 30 pixels, which will result in more accurate measurements.

Table lists the calculated diameter and tilt-angle values for different scenarios described before. Note that the diameter values reported here are the average diameters of the corresponding filaments in the air and we have used the approximate edge image shown in Fig. 4(b) for our calculations. Depending on the requirements, the diameter at a specific distance from the nozzle can also be calculated from the edge image. Tilt-angles for scenarios 1 and 2 are zero. On the other hand, tilt-angles for scenarios 3 and 4 were found to be approximately 10 and 21 degrees, respectively. We can also observe that the diameter for scenario 2 is greater than that of

the scenario 1, which is due to the higher input voltage in scenario 2. For scenario 4, the average diameter was found to be 9.2416 pixels which is maximum among the four scenarios considered.

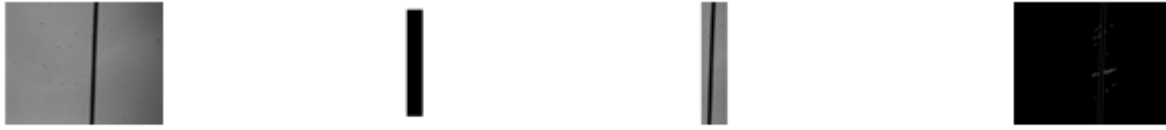


Figure 31. (a) Image of human hair; (b) The mask; (c) Masked image; (d) Edge image

If we use the piecewise approximate edge image (shown in Figure 29(d)), the tilt-angles and diameters for scenario 1 and 2 will be same as listed in Table 1. When using the piecewise approximate edge image for scenario 3, the tilt-angle is found to be 10.7441 degrees and the average diameter is computed as 6.9827 pixels. Moreover, for scenario 4, the tilt-angle value is computed as 18.4208 degrees and the average diameter is found to be 9.5292 pixels when piecewise approximate edge image is used. For better accuracy, we can use piecewise approximate image with large number of pieces (segments).

In our experiments, different masks are used for the processing of images of different scenarios presented in the previous section. The selection of a particular mask for an image is challenging task and we leave this for our future work. Moreover, the pixel pitch for the camera set up used in our experiments is $4.8\mu\text{m} \times 4.8\mu\text{m}$, which is not very large. Usually, the filament diameter varies in the range of $30\mu\text{m}$ to $60\mu\text{m}$. As a result of that, the filament width is represented by only 6 to 12 pixels range, which is not enough for extracting the filament information in a precise manner. Therefore, we are planning to upgrade our camera set up so that the filament information is captured with a large number of pixels and we can compute the useful parameters of the filament more accurately.

Conclusion

In this paper, a real-time monitor system for e-jet printing was established. The image processing results in e-jet printing for the purpose of assessment and quality control. The information contained in the filament such as the diameter and tilt-angle are required as the feedback in order to control the printing process. The main difficulties in the image analysis were identified as the background noise consisting of the printed material and the limited number of pixels representing the filament. Although the filament part could be extracted from the image using masking and Canny edge detection algorithm, there is a need of better camera set up for precise measurements.

This research not only established a real-time monitor system for printing detection but also provided a basis for the automatic fabrication approach for E-jet printing. With the feedback information provided by the monitor system, the future e-jet printer system will process and send signal to calibrate parameters like the jet speed, jet head distance from the substrate, even jet materials to ensure the quality of printing pattern. In order to realize this target, the feedback signal processing and transforming to control the printing procedure as well as the mechanical system will be further developed to support the automatic printing system. Another benefit from this research will be the nondestructive inspection of printed part. This real-time system can monitor and capture the images of the part, the images will be used to construct the real shape and roughness of the printed part. The constructed models have the same exact parameters of the printed parts which will contribute to simulations in finite element software. The achievement of this research in the future will help the cost cut, quality improvement, efficiency raising and automation of high resolution e-jet printing process which means the large scale industrialization manufacture using e-jet technique is possible.

References

- Abdullah, M. Z., Mohamad-Saleh, J., Fathinul-Syahir, A. S. & Mohd-Azemi, B. M., 2006. Discrimination and classification of fresh-cut starfruits (*Averrhoa carambola* L.) using automated machine vision system. *Journal of Food Engineering*, 76(4): pp. 506-523.
- Barton, K., Mishra, S., Alleyne, A., Ferreira, P. & Rogers, J., 2011. Control of high-resolution electrohydrodynamic jet printing. *Control Engineering Practice*, 19(11): pp. 1266-1273.
- Berger, S., Biehle, P., Villarroel, M., Brückmann, N., Richter, C. & Reinhart, G., 2016. Identification of Influence Parameters and Dependencies on the Illumination of Machine Vision Systems for Robots. In *Advanced Materials Research*, 1140, pp. 408-415.
- Canny, J., 1986. A computational approach to edge detection. *IEEE Transactions on pattern analysis and machine intelligence*, (6): pp. 679-698.
- Chen, Y. R., Chao, K. & Kim, M. S., 2002. Machine vision technology for agricultural applications. *Computers and electronics in Agriculture*, 36(2): pp. 173-191.
- Choi, D., Lee, W. S., Ehsani, R., Schueller, J. K. & Roka, F., 2015. Machine vision system for early yield estimation of citrus in a site-specific manner. *American Society of Agricultural and Biological Engineers*, pp. 1.
- Dai, Y. & Zhu, K., 2017. A machine vision system for micro-milling tool condition monitoring. *Precision Engineering*.
- Everton, S. K., Hirsch, M., Stravroulakis, P., Leach, R. K. & Clare, A. T., 2016. Review of in-situ process monitoring and in-situ metrology for metal additive manufacturing. *Materials & Design*, 95: pp. 431-445.
- Everton, S.K., Hirsch, M., Stravroulakis, P., Leach, R. K. & Clare, A. T., 2016. Review of in-situ process monitoring and in-situ metrology for metal additive manufacturing. *Materials & Design*, 95: pp. 431-445.
- Heinemann, P. H., Hughes, R., Morrow, C. T., Sommer, H. J., Beelman, R. B. & Wuest, P. J., 1997. Grading of mushrooms using a machine vision system. *Transactions of the ASAE*, 37(5): pp. 1671-1677.
- Kim, B. H., Onses, M. S., Lim, J. B., Nam, S., Oh, N., Kim, H., Yu, K.J., Lee, J. W., Kim, J. H., Kang, S. K. & Lee, C. H., 2015. High-resolution patterns of quantum dots formed by electrohydrodynamic jet printing for light-emitting diodes. *Nano letters*, 15(2): pp. 969-973.
- Kim, K., Kim, G., Lee, B. R., Ji, S., Kim, S. Y., An, B. W., Song, M. H. & Park, J. U., 2015. High-resolution electrohydrodynamic jet printing of small-molecule organic light-emitting diodes. *Nanoscale*, 7(32): pp. 13410-13415.

- Kuang, M., Wang, L. & Song, Y., 2014. Controllable printing droplets for high-resolution patterns. *Advanced Materials*, 26 (40), pp. 6950-6958.
- Kurada, S. & Bradley, C., 1997. A machine vision system for tool wear assessment. *Tribology International*, 30(4): pp. 295-304.
- Lee, J. W., 2002. A machine vision system for lane-departure detection. *Computer vision and image understanding*, 86(1): pp. 52-78.
- Lowe, D. G., 1987. Three-dimensional object recognition from single two-dimensional images. *Artificial intelligence*, 31(3): pp. 355-395.
- Luo, X., Jayas, D. S. & Symons, S. J., 1999. Identification of damaged kernels in wheat using a colour machine vision system. *Journal of cereal science*, 30(1): pp. 49-59.
- Mani, M., Lyons, K. W. & Gupta, S. K., 2014. Sustainability characterization for additive manufacturing. *Journal of research of the National Institute of Standards and Technology*, 119: pp. 419.
- Nakabo, Y., Ishii, I. & Ishikawa, M., 1997. 1ms Target Tracking System Using Massively Parallel Processing Vision. *Journal of the Robotics Society of Japan*, 15(3): pp. 417-421.
- Onses, M.S., Sutanto, E., Ferreira, P. M., Alleyne, A. G. & Rogers, J., A., 2015. Mechanisms, capabilities, and applications of high-resolution electrohydrodynamic jet printing. *Small*, 11(34), pp. 4237-4266.
- Otsu, N. A., 1979. Threshold selection method from gray-level histograms. *IEEE transactions on systems, man, and cybernetics*, 9(1): pp. 62-66.
- Park, J. U., Lee, S., Unarunotai, S., Sun, Y., Dunham, S., Song, T., Ferreira, P. M., Alleyne, A. G., Paik, U. & Rogers, J. A., 2010. Nanoscale, electrified liquid jets for high-resolution printing of charge. *Nano letters*, 10(2): pp. 584-591.
- Park, J.U., Hardy, M., Kang, S.J., Barton, K., Adair, K., kishore Mukhopadhyay, D., Lee, C. Y., Strano, M. S., Alleyne, A. G., Georgiadis, J. G. & Ferreira, P. M., 2007. High-resolution electrohydrodynamic jet printing. *Nature materials*, 6(10): pp. 782-789.
- Qin, H., Dong, J. & Lee, Y.S., 2017. Fabrication and electrical characterization of multi-layer capacitive touch sensors on flexible substrates by additive e-jet printing. *Journal of Manufacturing Processes*.
- Rao, P. K., Liu, J. P., Roberson, D., Kong, Z. J. & Williams, C., 2015. Online real-time quality monitoring in additive manufacturing processes using heterogeneous sensors. *Journal of Manufacturing Science and Engineering*, 137(6): pp. 061007.
- Rogers, J. A. & Paik, U., 2010. Nanofabrication: Nanoscale printing simplified. *Nature nanotechnology*, 5(6): pp. 385-386.

- Shahabi, H. H. & Ratnam, M. M., 2010. Noncontact roughness measurement of turned parts using machine vision. *The International Journal of Advanced Manufacturing Technology*, 46(1-4): pp. 275-284.
- Sitthi-Amorn, P., Ramos, J. E., Wang, Y., Kwan, J., Lan, J., Wang, W. & Matusik, W., 2015. MultiFab: a machine vision assisted platform for multi-material 3D printing. *ACM Transactions on Graphics (TOG)*, 34(4), pp. 129.
- Strand, T. C., 1985. Optical three-dimensional sensing for machine vision. *Optical engineering*, 24(1): pp. 240-253.
- Sutanto, E., Tan, Y., Onses, M.S., Cunningham, B.T. & Alleyne, A., 2014. Electrohydrodynamic jet printing of micro-optical devices. *Manufacturing Letter*, 2(1), pp. 4-7.
- Tsugawa, S., 1994. Vision-based vehicles in Japan: Machine vision systems and driving control systems. *IEEE Transactions on industrial electronics*, 41(4): pp. 398-405.
- Wei, C. & Dong, J., 2013. Direct fabrication of high-resolution three-dimensional polymeric scaffolds using electrohydrodynamic hot jet plotting. *Journal of Micromechanics and Microengineering*, 23(2): pp. 025017.
- Wei, C., Qin, H., Ramírez-Iglesias, N. A., Chiu, C. P., Lee, Y.S. & Dong, J., 2014. High-resolution ac-pulse modulated electrohydrodynamic jet printing on highly insulating substrates. *Journal of Micromechanics and Microengineering*, 24(4): pp. 045010.
- Yachida, M. & Tsuji, S., 1977. A versatile machine vision system for complex industrial parts. *IEEE Transactions on Computers*, 1(9): pp. 882-894.
- Yi, S. K., Haralick, R. M. & Shapiro, L. G., 1995. Optimal sensor and light source positioning for machine vision. *Computer Vision and Image Understanding*, 61(1): pp. 122-137.

CHAPTER 6. IN-SITU MONITORING OF ELECTROHYDRODYNAMIC INKJET PRINTING VIA SCALAR DIFFRACTION FOR PRINTED DROPLETS

Authors and Affiliations

Modified from a manuscript to be published in Journal of Manufacturing Systems. This research work is published by Xiao Zhang, Benjamin Lies, Hao Lyu, and Hantang Qin in the Journal of Manufacturing Systems, Volume 57, Pages 484.

Xiao Zhang, Benjamin Lies, Hantang Qin are from the Industrial and Manufacturing Systems Engineering Department at Iowa State University. Dr. Hao Lyu was a visiting scholar from the Industrial and Manufacturing Systems Engineering Department.

Ben and I are working together on the question formation, experiment design, data processing, writing, and analysis of this research. Ben worked more on the laser scalar theory. I focused on e-jet printing experiments, data processing, and corresponding analysis regarding the evaluation between the algorithm-predicted diameter and optical microscopy measured data. Dr. Lyu supported the optical system setup and paper review work. I want to acknowledge my advisor, Dr. Hantang Qin's support throughout this research work.

Abstract

Electrohydrodynamic inkjet (e-jet) printing is a technique which utilizes electrical forces to generate droplets in micro/nano scale using conductive inks. Currently, there is no procedure in place to measure the printed patterns without taking the sample away from the printer setup. Removal of the substrate from the printing stage during the e-jet printing process prevents any additional work from being performed on the sample. We investigated the application of scalar diffraction for the in-situ measurement and digital reconstruction of opaque material printed on transparent substrates. Measurement and characterization of the printed material can be achieved in-situ to alter printing condition in process for quality assurance. In order to accomplish the sample reconstruction, a digital recording of a scalar diffraction pattern in the image plane was employed in this paper with a magnification of 5x with the help of a combination of lenses. The reconstructed images were then compared to images captured by an offline high-resolution

microscope. The results indicated a submicron accuracy of the feature radii and the locations of feature centers. In addition to the quantitative measurements, this method also allows for the operator to view the overall form of the printed patterns. Our findings demonstrate an effective approach for in-situ monitoring of e-jet printing and printed patterns, which could pave the way for the industrial application in printing testing field.

Introduction

As the need for flexible electronics grows rapidly, the fabrication of small electronic components in micro and nano scale has been significantly necessary (Galliker 2012). Traditionally, etching and masks were used to fabricate these structures. These methods face drawbacks, however, namely poor customizability and high cost, which are difficult to overcome in order to achieve the high-resolution pattern (Onses 2015). Moreover, the requirement of a clean room environment further increases the difficulty of quick prototyping for electronic components and devices. Electrohydrodynamic jet (e-jet) printing is an emerging method for the fabrication of micro/nano structures in electronics and optical fields. This technique has the ability to print high-resolution patterns down to sub-micron with stable droplet generation in addition to fast fabrication for electronics (e.g., sensors) (Prasetyo 2013). With further development of the e-jet printing technique, advanced fabrication of electronics became possible. Dong fabricated self-recoverable and stretchable electronics by e-jet printing technique and further demonstrated the high-resolution capability of manufacturing these flexible electronics by finite element method (Han 2018). Rogers used e-jet printing to form patterns of quantum dots for light-emitting diodes (Kim 2015). Our group applied the e-jet printing technique to fabricate capacitive touch sensors and achieve sub-20 μ m conductive pattern on a flexible insulating substrate (Qin 2017). For better control of the e-jet printing process, many methods were proposed to improve the printing quality further. Dong used modulated ac-pulse voltage to

minimize the residual charge issue and overcame the long-predicted charge accumulation problem on highly insulating substrates (Qin 2017; Wei 2014; Wei 2015). With better voltage control strategy, Mishra demonstrated high-speed printing capability at 1 kHz with 3-5 μ m droplet size for an aqueous ink and 1-2 μ m for a photocurable polymer ink. High-speed e-jet printing method had the additional advantage of reducing the line-pattern width (Mishra 2010). Phung reported that the pattern width could be reduced from 20 μ m to 4 μ m by increasing the speed from 10 mm/s to 50mm/s (Phung 2017).

In order to improve reliability and quality control of e-jet printing process, many approaches were explored to investigate the influence of printing and material parameters. Lee investigated the effect of viscoelasticity of typical ink on Taylor cone formation using a two-model system (Yu 2016). Han applied the e-jet printing process for phase-change wax material; both experiment result and FEA models demonstrate agreement with each other (Han 2015). Ink characteristics played a large part in the final quality of printed patterns, and one such ink characteristic was the solvent used. Je used silver nanoink for printing, which contained a low boiling point solvent, and the results were dots and lines with superior quality (Shi 2011). However, it was difficult to monitor the results of these altered printing parameters. Many researchers focused on the image processing process to instruct the printing process such as Gardner reported the operation of optical coherence tomography in a selective laser sintering system to monitor the surface feature of the printed part (Gardner 2018). Similar research has been done by Grasso, a method was proposed for detection and recognition of spatial defects during the selective laser melting process, but challenges remain under different frame rates at the same experimental setup (Grasso 2017). During the ink-jet printing process of Liquid Metal Inkjet Printing (LMIP), Wang solved the uncertain factors by using vision-based closed-loop

control system which achieved stable jetting behavior (Wang 2018). Imani proposed image-based method to collect nonlinearity, irregularity during the manufacturing process, which link the process parameters with in-process images (Imani 2018). Wang applied in-situ droplet inspection based on image analysis for liquid metal jet 3D printing, but not for printed parts (Wang 2017). Liu developed image-based closed-loop system to diagnosis the fused filament fabrication system with captured images and provided the automatic adjustment of the parameters to detect the defects (Liu 2019). In previous works, we used machine vision to enable real-time monitoring of the e-jet printing process and the implementation of a feedback control system to achieve a higher quality pattern (Singh 2018). The quality of manufacturing process could be influenced by particle distribution, Kin analyzed the images of particle distribution to provide general guidelines to the manufacturing process in nanomanufacturing and biomanufacturing (Kin 2013). A similar machine vision system was used by Lee, who applied a vision algorithm to enable in-situ measurement of the e-jet printing process (Kwon 2013). Both of these vision processes monitored the Taylor cone formation, but they did not show the pattern printed on the substrate in real-time.

Currently, measurements of printed results are usually performed offline via an optical microscope or other similar metrology methods, which results in the removal of the substrate from the printing platform. Once the substrate has been removed, additional printing is impossible as realignment is difficult and most time is not feasible. An alternative new method for in-situ monitoring and characterization of such printed droplets is needed. Inkjet-based printing is a droplet driven process. The measurement of dot patterns (formed by droplets) is the key step before the realization of printing high quality patterns. Successful dot patterns could be used for micro/nano array patterning, and line patterns could contribute to the manufacture of

devices such as wearable sensors. Laser diffraction system is flexible for measurement in various environments and robust for in-situ characterization. In this contribution, we demonstrated an approach using scalar diffraction for the in-situ measurement and digital reconstruction of e-jet printing. A digital recording of a scalar diffraction pattern in the image plane was employed to evaluate the printed results in process. This approach could open a new way for in-situ monitoring and characterization of e-jet printing.

Methodology

E-Jet printing setup

The experimental setup of e-jet printing was shown in Figure 32(a). A commercial silver nanoink was used as the printing material for this experiment. A three-axis nano-positioning stage was used for the movement of the printer head and substrate. During the printing, the movement in x and y direction was programmed in the horizontal plane for printing on the substrate. The z direction was programmed to obtain a desired standoff distance from the nozzle tip to the substrate. The positional resolution along the x and y direction was 50 nm, and the speed of lateral directional movement could vary from 0.001 mm/s to 20 mm/s. The substrate used as the printing platform was transparent (e.g., glass slides or PET films) and the standoff distance was set to 20 μ m. A high electric potential was applied between the nozzle and substrate, with the voltage ranging between 500V to 1000V. The positive and negative electrodes of the voltage supplier were connected with the nozzle and the substrate, respectively. The diameter of the nozzle varied between 2 μ m to 30 μ m. With such small sizes, the surface tension of ink prevented droplet formation at the tip of the nozzle without a voltage supply.

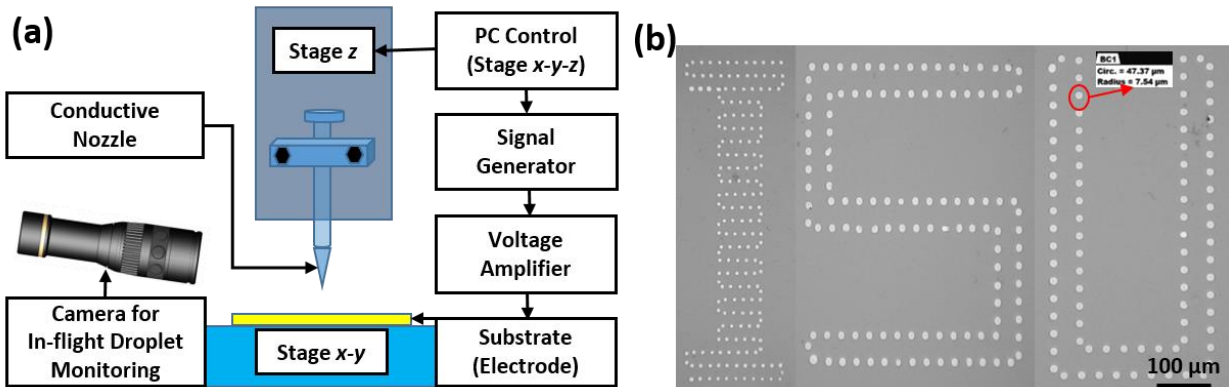


Figure 32. (a) Schematic of e-jet printing, and (b) Printed droplet patterns

The electrical force drove the silver nanoink out of the nozzle onto the substrate and served as the primary force for stable jetting the material. A camera was used to monitor the region between the nozzle and the substrate. After the settlement of the nozzle on the system, the positive and negative electrodes of the voltage supply were connected with the nozzle and the substrate, respectively. Via control of process parameters (e.g., voltages, plotting speed, etc.), different sizes of silver droplets, dots, and lines were achieved, as shown in Figure 32(b).

In a traditional setup of e-jet printing, the camera shown in Figure 32(a) was used to observe the region between the nozzle and the printing substrate, and to monitor the in-flight droplet behavior. The resolution of such optical zoom lens and camera could be as high as $2\mu\text{m}$. However, this in-situ setup could not observe the pattern being printed. Aligning additional zoom lens system on the z stage increased extra load and reduced control resolution of the z-axis. This means that the operator could only predict what the printed pattern would look like based on the printing parameters established beforehand using a traditional setup in Figure 32(a). These parameters included voltage, ink characteristics, standoff distance, translation speed, etc. Currently, the method to characterize the printed pattern was to remove the substrate from the printing stage and to conduct metrology offline using microscopy (SEM or optical). Removal

from the stage eliminated the possibility for any additional future printing as there was no longer any point of reference and the small scale of the printing made realignment very difficult.

Without an effective approach to recognize printed patterns in-situ or establish a point of reference for future alignment, quality control of e-jet printing would likely to remain difficult.

In this paper, a scalar diffraction vision system was developed to resolve the challenge.

Scalar diffraction vision system

The following scalar diffraction system was proposed to solve the challenges mentioned in previous sections regarding quality assurance and feature recognition for e-jet printing. Figure 33(a) demonstrated the optical equipment location as it would relate to the e-jet printing setup and Figure 33(b) showed the specifics of the components of the optical system setup.

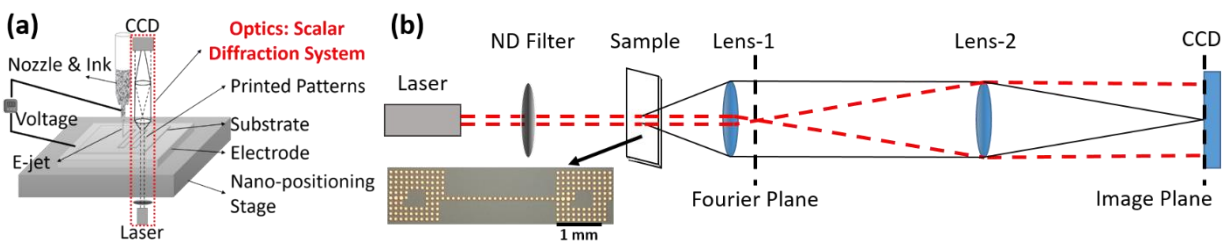


Figure 33. (a) Location of scalar diffraction system in e-jet printing setup, and (b) A schematic of the optical components for scalar diffraction: Laser, Step variable neutral density filter (ND), Sample, Lens-1, Lens-2, and Charge Coupled Device (CCD)

The laser as a light source used in this experiment was a 2 mW HeNe laser (wavelength 632 nm). The light then passed through a step neutral density (ND) filter. The magnitude of this filter was set such that the light incident on the CCD did not saturate the camera in order to preserve as much information as possible. The sample used in this experiment was silver nanoink printed on a transparent substrate via e-jet printing. The ink pattern was on the side opposite the incident light. Nemoto investigated the propagation of a Gaussian beam when passing through a dielectric material and determined that the waist size of the beam was unchanged when the light

was normal to the surface of the substrate (Nemoto 1989). Some of the incident beam was then diffracted by the sample pattern, and the unscattered light passed through the transparent substrate (reference beam). The light diffracted due to the sample was then collimated by Lens-1 while also focusing the reference beam such that it could be represented by a single point in the Fourier plane. The Fourier plane was located behind Lens-1 at a distance equal to the focal length of Lens-1. The second lens, Lens-2, focused the collimated diffraction pattern resulting in the formation of the original image multiplied by the magnification that resulted from the objective lens system. In this optical configuration, the digital sensor (e.g., charge coupled device CCD) could record an intensity pattern in either the Fourier plane or the image plane. Each of these planes had unique characteristics. The Fourier plane was observed after the incident light had been diffracted by the sample and the resulting pattern was observed in the far field. In order to satisfy this far field condition, the diffraction pattern resulting from the light incident to the sample was collimated by a lens. This collimated pattern effectively described the pattern at infinity. This far-field pattern was typically referred to as the Fraunhofer regime, which was often described in terms of frequency. An example of a pattern recorded in the Fourier plane was shown in Figure 34(a). The image plane contained the reconstruction of the target sample in the spatial domain. An example of a pattern recorded in the image plane was shown in Figure 34(b).

The Fraunhofer diffraction was described as the product of multiple approximations made in optics. Initially, the Huygens-Fresnel principle (Miller 1991) was used to describe the diffraction of an object through the summation of small wavelets around the contour of an object or through an aperture. Later, the Fresnel-Kirchhoff integral theorem (Kirchhoff 1883) expanded upon this theory through the implementation of Greens theorems (Green 1828). The resulting equations were then approximated and categorized into two fields, Fresnel (near field) and

Fraunhofer (far field) diffraction (Born 2013; Jenkins 1958). The integrals associated with Fresnel diffraction were computationally challenging to solve outside of several known configurations. Thus, the most straightforward approximation (computationally) was the Fraunhofer approximation, which utilized the Fourier transform to solve mostly due to the implementation of the Fast Fourier Transform (FFT) (Cooley 1965).

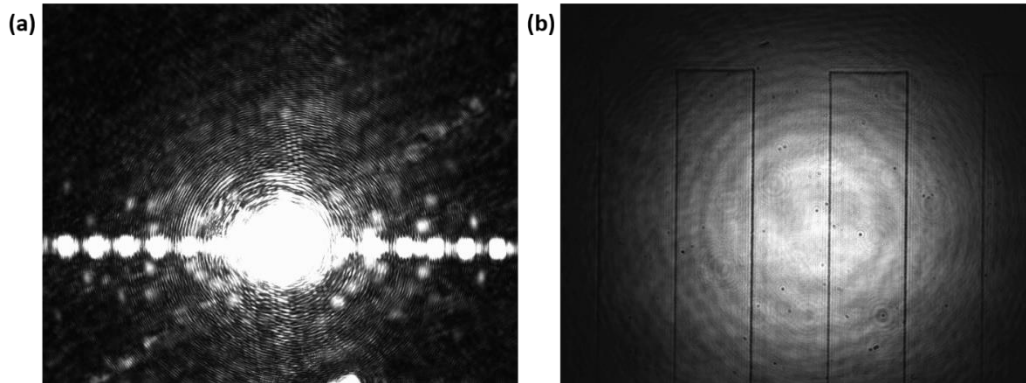


Figure 34. Intensity distribution resulting from the printed pattern in the (a) Fourier plane and (b) Image plane

In the Fourier plane, the intensity distribution was a continuous function describing the frequency domain, but the device used for digital recording was discrete, which indicated that an insufficient sampling rate could result in aliasing of the data. In order to accurately recreate the continuous signal, the Nyquist-Shannon Sampling Theorem (Shannon 1998) should be implemented, which described the resolution restrictions due to predefined sensor parameters and the bandwidth limitations of the system. In addition to resolution limits imposed by discrete sampling, the intensity distribution in the Fourier plane had a couple of unwanted components. These components were the twin image and zero order image. There have been many methods proposed to isolate and differentiate the useful information from the twin and zero-order images. These methods required additional processing time however and should be avoided if possible.

The alternative to the Fourier plane was the image plane. The resolution of the image plane was not restricted by the Nyquist-Shannon Theorem as another lens was added which acted as a continuous inverse Fourier transform (Coppola 2004). This resulted in an image of the sample plane multiplied by a magnification factor determined by the combination of lenses acting as the objective. As a result, recording in the image plane removed the need to experimentally or computationally remove the twin and zero-order image. The only calculations needed to interpret the image plane were the magnification due to the objective lens combination and the conversion from the image plane to the sample plane. The image resulting from the first lens was then used as the object for the second lens. The magnification of each lens depended on the distance at which the object was being observed.

The resolution in the image plane was determined as a function of effective magnification and the discrete sample sizing of the camera. The resolution of the camera and FOV regarding the sample plane could then be determined. There were several factors which may limit resolution in the system. The diffraction of light as it passed through a lens was an unavoidable problem. This resolution limit was typically calculated and used as an ideal case. In our study, the objective lens had a numerical aperture of 1/9.8. This resulted in a resolution limit of 3.096 μm in the sample plane. The camera pixel corresponded to an area of 0.92 μm in the sample plane. As a result, the resolution limitation was due to the diffraction. A resolution of 3 μm was small in comparison to the feature sizes of the sample. In this case, the limiting factor would be the camera itself.

Image processing

E-jet printing could generate droplet and dot patterns on flexible and transparent substrates as shown in Figure 32(b). In this study, in order to utilize scalar diffraction system for quality assurance of e-jet printing, we fabricated the patterns with certain common defects (e.g.,

non-circularity, line coalescence, droplets connection, etc.). Imaging processing algorithms were developed to perform feature recognition and quality control.

Background analysis

In the image plane, the unscattered light was magnified onto the camera in a Gaussian shaped intensity pattern. This Gaussian pattern was constant among all of the images, so it was essential to isolate and remove this pattern. Several images were taken when there was no printed silver dots on the substrate. The average between these images was used in order to reduce the noise caused by any dust that could be on the transparent substrate. The average was found using Equation 5,

$$B(x, y) = \frac{\sum_{i=0}^n b_i(x, y)}{n} \quad (5)$$

where $B(x, y)$ represented the average pixel intensity for a given pixel. Each individual background image was represented by b_i where the number of images averaged was n . There were several perturbations which were consistent throughout all of the background images which did not require to be removed as they would remain in the sample image as well. In Figure 35, a reducible disturbance has been circled in red for both images.

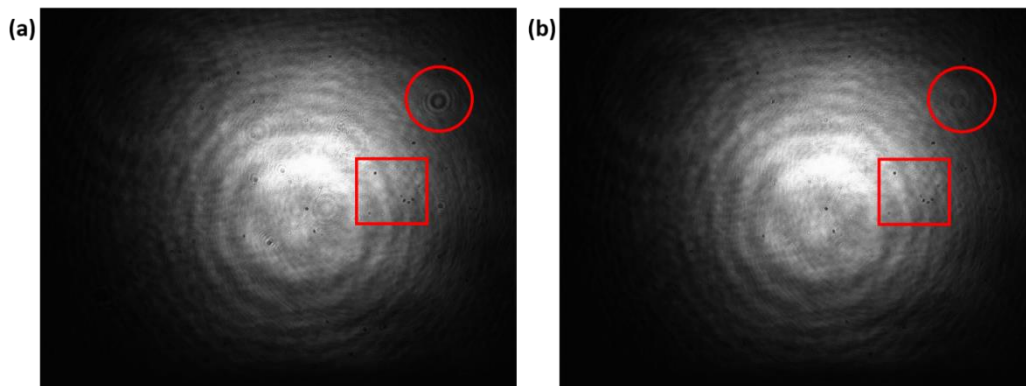


Figure 35. (a) Singular background images with a unique disturbance (red circle) and several consistent disturbances (red square), and (b) Average of several background images

This was an example of how the intensity of the noise, which was inconsistent in the images (unique), was reduced. The square indicated several dots which were constant among all of the background images taken. This was dust on a lens or the camera itself which would be consistent in every image, thus remaining during the average procedure. The sample image was then subtracted from the average background image. The sample produced a darker pattern in the shape of the sample. Thus any negative values resulting from the subtraction could be set to '0'. This reduced noise as well as errors caused by an imperfect background image. The result was a sample pattern in greyscale without the reference beam. This was shown in Figure 36(a). The mathematical representation of this subtractive process was depicted in Equation 6.

$$D(x, y) = \max(B(x, y) - S(x, y), 0) \quad (6)$$

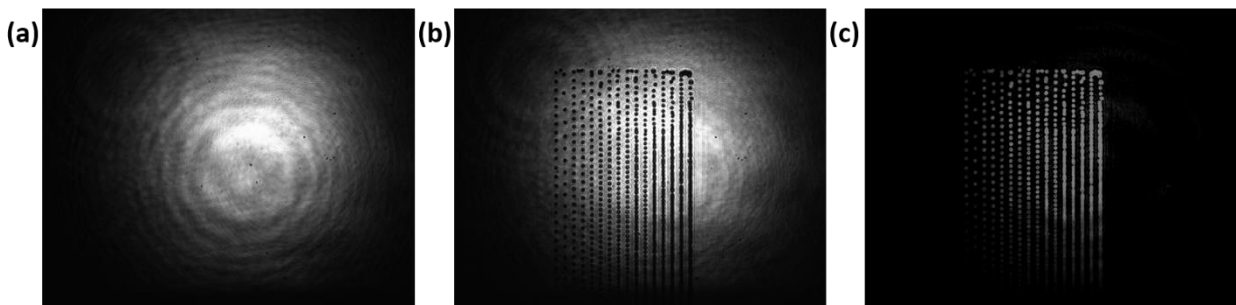


Figure 36. (a) The average background image described by Equation 1, (b) The sample image, and (c) The result of the subtractive process described by Equation 2

Binarization and filtering

This magnified sample image contained locational and dimensional information for identification of reference point and evaluation of printing quality. In order to achieve real-time image processing, a binarization technique was used to convert the image from a greyscale into a black and white. The black represented the background while the white represented the pattern printed on the substrate. The binarization technique used in this experiment utilized local adaptive thresholding (Bradley 200734), which created several smaller windows inside the main

image. Each neighborhood was approximately one eighth the size of the original image. In our algorithms, the mean of the neighborhood intensities was determined, and a sensitivity value was assigned by the user. The threshold for each neighborhood was a percentage of the mean value based on the sensitivity. The higher the sensitivity, the lower the threshold value resulting in more foreground pixels being identified. All of the intensity values of the pixels in the neighborhood were compared to this threshold. The greyscale image was then converted to black and white based on this threshold value. The value chosen for sensitivity was significant. For an image shown in Figure 36(c), a sensitivity that was too low could result in the loss of sample information Figure 36(a), and a sensitivity that was too high could result in amplification of noise or saturation of the sample Figure 37(b). It was also observed that by increasing the number of pixels above the threshold, the size of a feature varied slightly.

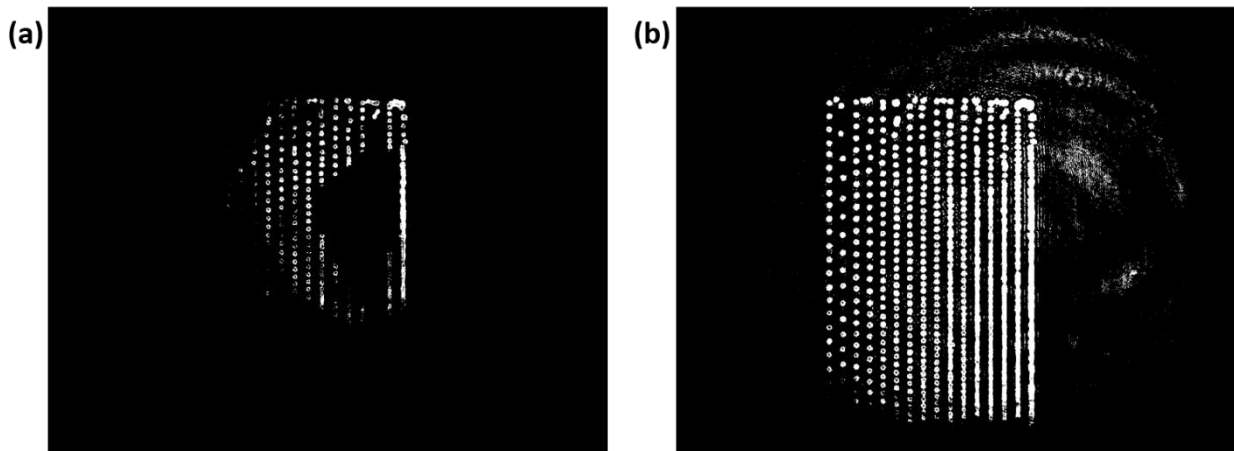


Figure 37. (a) Image binarization using a low sensitivity (0.05, assigned by the user) resulting in information loss, and (b) High sensitivity (0.55) resulting in the amplification of noise

Cropping and combining

The data from image plane could be binarized, but it has been observed that the areas with low contrast between the sample images and the background were not always reconstructed correctly, which limited the smart feature recognition of the system. In order to combat this, a

region of interest (ROI) case study was established. The ROI was positioned over the area with the most significant contrast, the center of the Gaussian light. The ROI did not move as the background light remains the same while the sample was moving during printing. In this work, the ROI has been established to be a 400 x 400 pixel region. The size was determined in order to maintain the high quality of information as well as a large physical area covered. The ROI of the sample that was used for further investigation was shown in Figure 38. As mentioned in the previous section, the patterns were designed to reflect potential defects and to present different printing conditions.

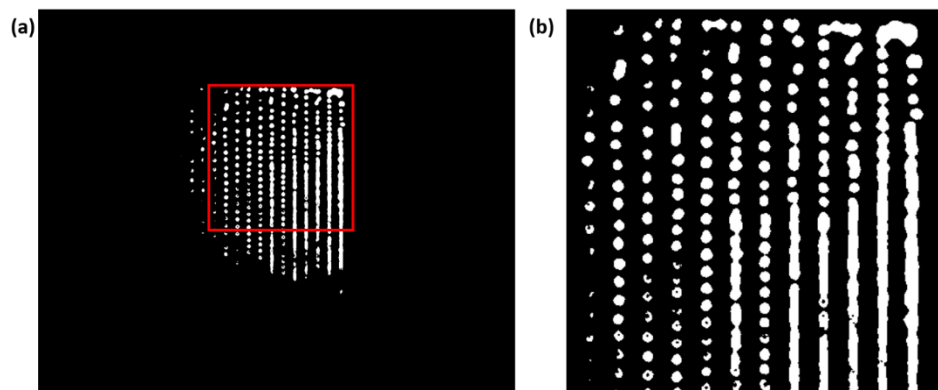


Figure 38. (a) The full binarized image with the ROI identified, and (b) Full view of the ROI

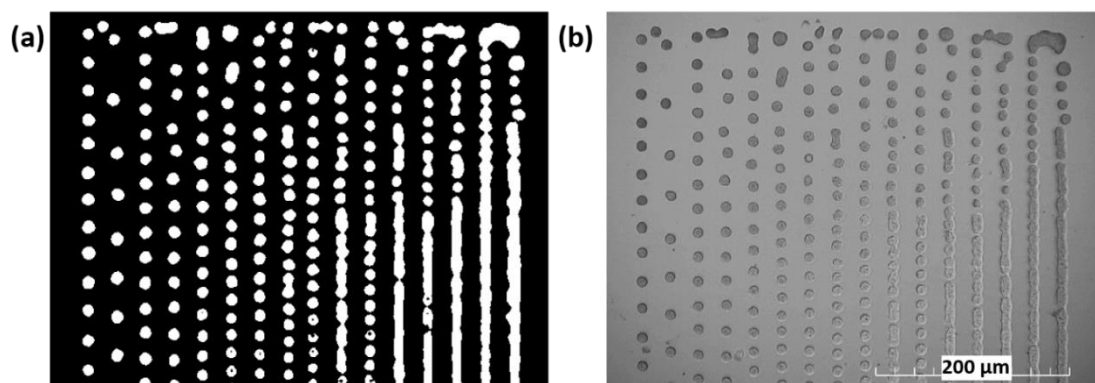


Figure 39. (a) Combination of two ROI with its counterpart captured by (b) The microscope

Once the region of interest has been established, several ROI could be combined in order to reconstruct the entire image. Currently, this was achieved through feature matching. An

example of a combination of two ROI was shown in Figure 39 in comparison to the same pattern under a digital microscope. As previously mentioned in the binarization and filter section, it could be seen that when the features were close to each other, some features were combined. This was caused by the selection of the binarization sensitivity or the work of the median filter.

Circle finding

After image reconstruction of the sample, the reconstructed images could then be analyzed to identify key features. The specific sample used in this study aimed to create a dot pattern so the feature identification approach will identify circles via circular “Hough” transform (Atherton 1999). The method utilized the boundaries of each connected body. A circle was then applied to those candidates. These circles corresponded to a cone in the 3D Hough parameter space. The theory for the space could be represented as:

$$(x - a)^2 + (y - b)^2 = r^2 \quad (7)$$

where (a, b) represented the circle center, and r represented the radius. The candidate pixels were represented by (x, y) . The intersections of the resulting cones in the Hough space were collected in an accumulator matrix. The area was determined by the accumulator matrix which counted the intersections. From this matrix, the most suitable circle parameters were determined (a, b, r) . This approach also required a sensitivity threshold that must be set by the user in addition to a radius range. With regards to the sensitivity, too low a sensitivity and the program would not be able to pick up a feature unless it was a near perfect circle, and too high a sensitivity and it would show false alarms (FA). An FA was determined to be anything that was identified as a circle by the program which was not determined by the operator to be a circle, typically when multiple droplets were deposited too close resulting in one large figure. The limitation was due to the unique capability of a circular Hough transform which was the ability

to find circles that were partially obscured by other objects or features. Examples of several sensitivity values were demonstrated in Figure 40.

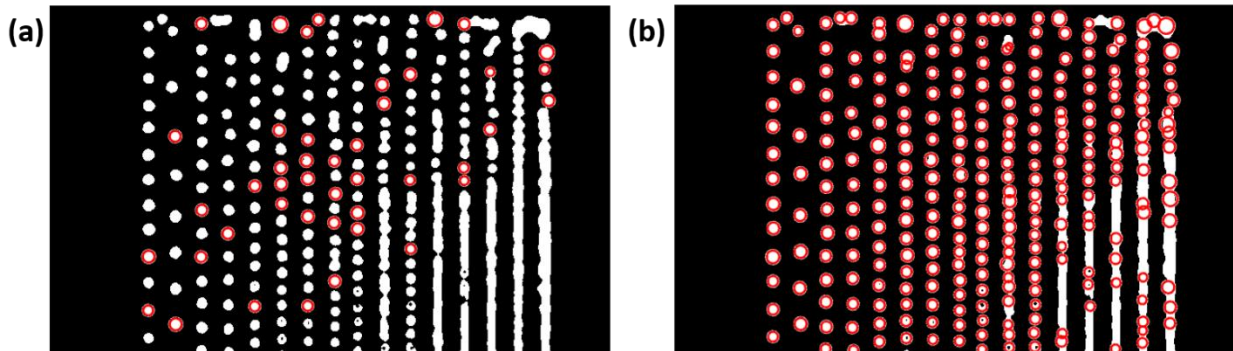


Figure 40. The images with user defined circle sensitivity which was (a) Too low, and (b) Too high

Once a circle has been identified, the radius and location of the circle were recorded. The accuracy, precision, and reliability of these location and size measurements would be compared with those measured by an optical microscope in the following section. In addition to the radius and location of the circle size, image processing could delete circles that overlapped.

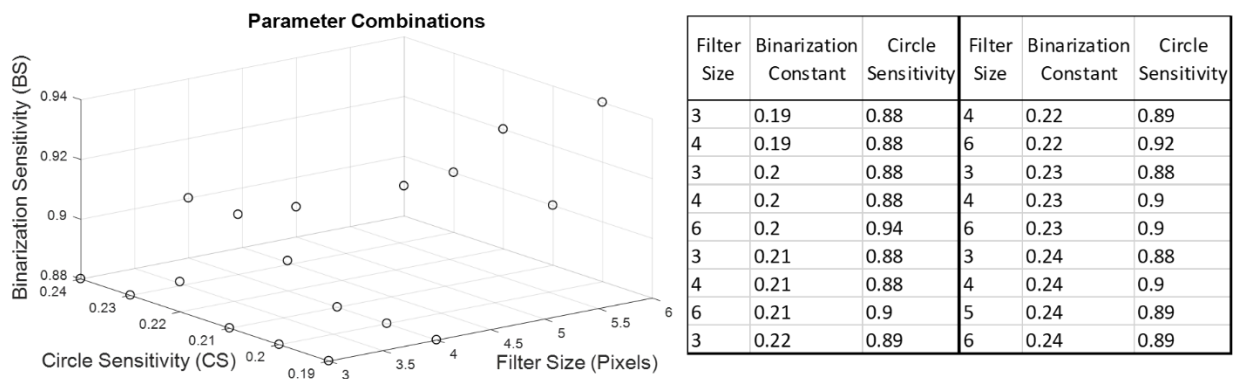
Overlapping circles can be seen in the top right corner of Figure 40(b). Depending on the preference of the operator, these could be removed in order to reduce the number of FA. Via the analysis of printed dots and image processing, the dot quality was easy to estimate, which could give direct guidance and feedback of printing parameter optimization.

Results and discussion

In the previous section, the selection procedure for the binarization sensitivity, median filter size, and the circle finding sensitivity have been discussed. These constants corresponded to the `imbinarize()`, `medfilt2()`, and `imcircularfind()` functions in Matlab. A range was set for each of these constants, and then each combination was processed and characterized. The binarization constant ranged from 0.15 to 0.25 in increments of 0.01. A smaller binarization constant resulted

in the loss of dots and a larger constant resulted in additional noise and inflation of the dots (as shown in Figure 37(a-b)). The median filter size ranged from 3 to 6 pixels in increments of 1. A smaller filter size resulted in poor noise reduction, and the larger filter size was more likely to combine dots and removed smaller dots entirely. The last constant, the circle finding sensitivity, ranged from 0.85 to 0.95 in increments of 0.01. Sensitivities smaller than 0.85 resulted in many “misses” and sensitivities higher than 0.95 resulted in a larger number of FA. In total, 484 combinations were tested. From these 484 variations, any combination which missed a dot was removed. In addition, the minimum circle sensitivity was used in order to reduce unnecessary false alarms. The result of these constraints were 18 different combinations as shown in Table 4.

Table 4. Different combinations of constants in imaging processing to test the scalar diffraction approach for identification of printed dot patterns



Utilizing the combinations in Table 4, size distributions were created which represented the size distribution of the dots. These image processing size distributions (IPSD) were then compared with the microscope measured size distributions (MMSD). When comparing the IPSD and the MMSD, it was noted that the distributions appeared relatively normal, as shown in the probability density function in Figure 41(a). Thus, modeling them under the assumption that they were normally distributed that allowed for the computation of the mean

and the standard deviation, both of which could be used to characterize the data as shown in Figure 41(b).

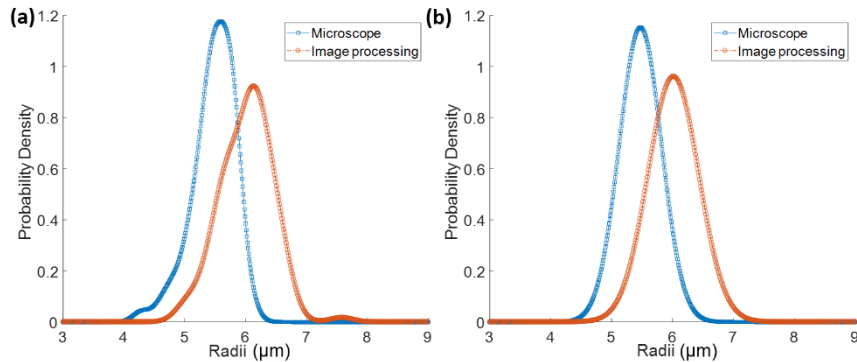


Figure 41. (a) Radii comparison between the microscope and image processing algorithm, and (b) After normalization

In addition, the number of false alarms could be easily determined as the remaining combinations have no “misses” and the number of “hits” was known. In the study, the defining characteristics were the absolute difference between the IPSD μ_1 and the MMSD μ_2 (denoted $\Delta\mu$), the absolute difference between the IPSD σ_1 and the MMSD σ_2 (denoted $\Delta\sigma$), and the number of false alarms. Each of these 18 combinations was then sorted 1-18 for each of these defining characteristics. The lower values being number 1, higher values being 18. Weight was given to each combination. The weight of each characteristic was subject to change depending on the needs of the operator and specific applications. As one example, Table 2 showed the results of an even weight applied to the $\Delta\sigma$, $\Delta\mu$ and the number of ‘false alarms’. The performance of each set of image processing parameters was then ranked for each sample group.

There were six different groupings of dots that were observed in this experiment. The first group was shown in the image processing section and can be entirely seen in Figure 40. The remaining five groups utilized the same image processing routine using the 18 combinations of Filter Size, Binarization Constant, and Circle Sensitivity described in Table 1. Each combination

of image processing parameters resulted in a $\Delta\mu$ and $\Delta\sigma$ for each of the six dot groups. From these, the average absolute difference in the mean could be calculated and that the standard deviation of this average was computed as well. This average $\Delta\mu$ could then be plotted as a function of the binarization sensitivity as well as the filter size as shown in Fig. 11a and Fig. 11b respectively. The circle finding sensitivity was excluded as the lowest value resulting in no misses was chosen.

Table 5. Results of an even weight applied to the $\Delta\sigma$, $\Delta\mu$ and the number of “false alarms” for optimization of coefficients and constants

| Filter Size | Binarization Constant | Circle Sensitivity | Group 1 | Group 2 | Group 3 | Group 4 | Group 5 | Group 6 | Total |
|-------------|-----------------------|--------------------|---------|---------|---------|---------|---------|---------|-------|
| 5 | 0.24 | 0.89 | 7 | 1 | 5 | 2 | 1 | 6 | 22 |
| 6 | 0.24 | 0.89 | 3 | 2 | 4 | 6 | 3 | 5 | 23 |
| 4 | 0.20 | 0.88 | 2 | 4 | 8 | 6 | 2 | 4 | 26 |
| 4 | 0.19 | 0.88 | 8 | 3 | 11 | 1 | 4 | 1 | 28 |
| 3 | 0.19 | 0.88 | 11 | 10 | 2 | 1 | 4 | 1 | 29 |
| 6 | 0.21 | 0.90 | 10 | 6 | 3 | 4 | 5 | 5 | 33 |
| 3 | 0.20 | 0.88 | 5 | 14 | 2 | 3 | 9 | 3 | 36 |
| 6 | 0.23 | 0.90 | 12 | 5 | 6 | 7 | 6 | 2 | 38 |
| 4 | 0.21 | 0.88 | 1 | 9 | 13 | 5 | 5 | 8 | 41 |
| 6 | 0.22 | 0.92 | 13 | 11 | 1 | 8 | 4 | 8 | 45 |
| 3 | 0.21 | 0.88 | 9 | 8 | 7 | 7 | 8 | 7 | 46 |
| 6 | 0.20 | 0.94 | 13 | 12 | 10 | 7 | 7 | 7 | 56 |
| 3 | 0.23 | 0.88 | 6 | 15 | 9 | 9 | 9 | 12 | 60 |
| 4 | 0.22 | 0.89 | 15 | 7 | 14 | 11 | 6 | 10 | 63 |
| 3 | 0.22 | 0.89 | 11 | 16 | 12 | 10 | 11 | 8 | 68 |
| 3 | 0.24 | 0.88 | 4 | 18 | 15 | 11 | 12 | 11 | 71 |
| 4 | 0.24 | 0.90 | 14 | 17 | 15 | 9 | 10 | 9 | 74 |
| 4 | 0.23 | 0.90 | 16 | 13 | 14 | 11 | 10 | 12 | 76 |

There were several trends in the values shown in Figure 42. The accuracy and precision were a function of the binarization sensitivity and filter size. The size of these error bars was representative of the standard deviation of the measured $\Delta\mu$ values, of the 18, with regards to binarization sensitivity and filter size respectively. The smaller the quantity, the more accurate the IPSD was to the MMSD. The smaller the error bars, the more consistent and therefore more

precise the IPSD was. The results shown in Figure 42 indicated that there was very little difference in the mean value of this distribution when selecting the binarization constant. When looking strictly at the binarization constant, it was only necessary that the operator chose a value that did not remove desired data points or generate too much noise when selecting the range. The constant should be large enough such that none of the dots were completely removed and small enough such that the noise was not an issue. In our study, a binarization constant of 0.19-0.24 were all sufficient with 0.2 being the most accurate. With regards to precision, 0.19 maintained the most similar standard deviation. When comparing the influence of the filter size, it should be noted that the smaller the filter size, the less accurate the resulting distribution was. When measuring the precision of the system, the largest filter size, 6, had the lowest precision. It was concluded that a filter size of 5 was best for the highest accuracy and precision combination. This filter size had the second highest accuracy and the best precision.

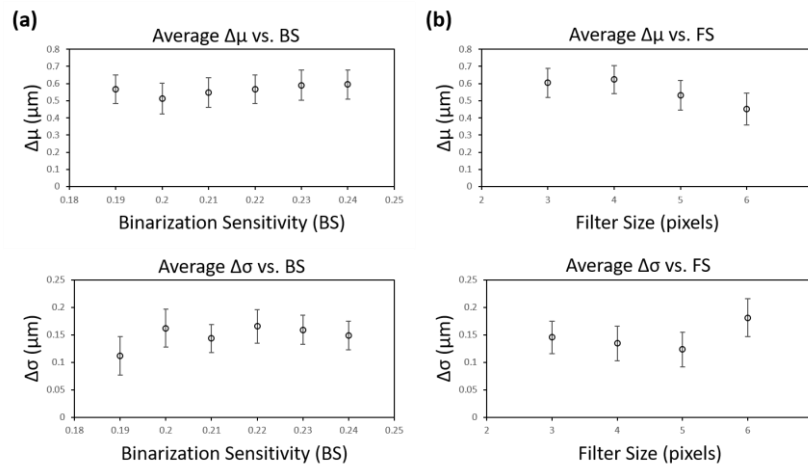


Figure 42. Average value of (a) Binarization sensitivity (BS), and (b) Filter size (FS) comparison

There were several ways that the data could be interpreted. First, the operator may be looking for settings which resulted in a particle size distribution most similar to the measurements given when measured via a microscope. It represented the most accurate settings

or the settings which resulted in the smallest deviation (on average) from the actual distribution, which can be represented by the smallest $\Delta\mu$ values. Second, another measure of the quality of this methodology was the consistency of results between multiple sample areas. The consistency and the grouping of the differences was referred to as the precision of the system, which was represented in this study, as the width of the curve, $\Delta\sigma$. This variability was not necessarily a negative factor as long as it was predictable and could be accounted for. Third, another measure was the number of false alarms present. In the case of feedback control for e-jet printing, false alarm measurement could be misleading and inconsistent systematically. Typically imperfections in this dot printing process were caused by the overlap of multiple dots. This circle detection method, by nature, found well-formed circles and those which were partially obscured, or in this study, overlapped. The operator could not tell if the dots were independent or connected as they were detected the same way in both cases. This made it difficult to draw a conclusion regarding the quality of the reproduction of the IPSP, with respect to the number of FA unless it was reviewed as it did not contain information regarding connectivity. The number of false alarms played a role in the mean and standard deviation of the size distribution; however, so it should not be ignored entirely. As a summary, it was ultimately up to the user and application to determine how each of these factors should be weighed when determining the “best” set of parameters to use for the image processing of scalar diffraction system.

The system has demonstrated good resolution. One of the advantages is the capability to measure sub-30 μm features to within several microns, but the overall performance is dependent on the parameters, not necessarily the system. The system is based on automated image processing with no differences among repeatable tests. We experimented with six different dot patterns and compared those to measurements collected via an optical microscope. The limitation

of this system is the requirement of a transparent substrate which may restrict the application of this system in a wider area. Other than that, there are also many advantages. Due to the application of laser source, it has a strong capability to get rid of environmental influences such as distance between object and laser source which enable the flexible setup of this system. The repeatability of this system could be ensured by the single wavelength of a stable laser source which supports the robustness of this laser diffraction system.

Conclusion

In this paper, a scalar diffraction system was developed for in-situ monitoring of printed patterns in e-jet printing. The approach had the capability to calculate the droplet size distribution of a sample without removal from the printing platform with magnification for micro/nano scale detection. The focus of this work is an in-process measurement technique, specifically for e-jet printing on transparent substrates. There are currently no such processes in use, which is an indication that this is the first application of such a system in this field. This work also has the capability to automate much/all of the inspection process. The measurements made during the image processing were consistent as long as the process parameters were chosen correctly. In addition to the measurements, the scalar diffraction system allowed an easy-setup and low-cost solution for the operator to monitor the quality of the printed sample, which was not currently feasible unless the sample was removed from the workspace and measured offline. The binarization constant should be chosen such that the noise was low while maintaining all of the feature data. The filter size should be chosen to remove the additional noise while maintaining the smaller features and avoiding the combination of dots. The circle finding sensitivity should be chosen such that the lowest number of false alarms were present. Several combinations of these parameters were demonstrated based on our printing setup, and the resulting difference in the size distributions was explained in details.

Our future work will be focusing on a digital twin system for e-jet printing based on metrology. Using the printing quality information as feedback control signals for e-jet printing, the approach could ensure dots were of the correct size for the correct feature and potentially spacing. Another significant contribution was that the approach enables the capability for easy system lineup with a reference dots on substrates when multiple layers of transparent substrates are required for higher dimensional fabrication.

References

- Atherton, T. J. & Kerbyson, D. J., 1999. Size invariant circle detection. *Image and Vision computing*, 17(11), pp. 795-803.
- Born, M. & Wolf, E., 2013. *Principles of optics: electromagnetic theory of propagation, interference and diffraction of light*. Elsevier: Chapter 8.
- Bradley, D. & Roth, G., 2007. Adaptive thresholding using the integral image. *Journal of graphics tools*, 12(2), pp. 13-21.
- Cooley, J. W. & Tukey, J. W., 1965. An algorithm for the machine calculation of complex Fourier series. *Mathematics of computation*, 19(90), pp. 297-301.
- Coppola, G., Ferraro, P., Iodice, M., De Nicola, S., Finizio, A. & Grilli, S., 2004. A digital holographic microscope for complete characterization of microelectromechanical systems. *Measurement Science and Technology*, 15(3), pp. 529.
- Galliker, P., Schneider, J., Eghlidi, H., Kress, S., Sandoghdar, V. & Poulikakos, D., 2012. Direct printing of nanostructures by electrostatic autofocussing of ink nanodroplets. *Nature communications*, 3, pp. 890.
- Gardner, M. R., Lewis, A., Park, J., McElroy, A. B., Estrada, A. D., Fish, S., Beaman, J. J. & Milner, T. E., 2018. In situ process monitoring in selective laser sintering using optical coherence tomography. *Optical Engineering*, 57(4), p. 041407.
- Grasso, M., Laguzza, V., Semeraro, Q. & Colosimo, B. M., 2017. In-process monitoring of selective laser melting: spatial detection of defects via image data analysis. *Journal of Manufacturing Science and Engineering*, 139(5), p. 051001.
- Green, G., 1828. *An essay on the application of mathematical analysis to the theories of electricity and magnetism*. Wezäta-Melins Aktiebolag.
- Han Y. & Dong, J., 2018. Fabrication of self-recoverable flexible and stretchable electronic devices. *Journal of Manufacturing Systems*, 48, pp. 24-29.

- Han, Y., Wei, C. & Dong, J., 2015. Droplet formation and settlement of phase-change ink in high resolution electrohydrodynamic (EHD) 3D printing. *Journal of Manufacturing Processes*, 20, pp. 485-491.
- Imani, F., Yao, B., Chen, R., Rao, P. & Yang, H., 2018. Fractal pattern recognition of image profiles for manufacturing process and control. *Proc. ASME 2018 13th International Manufacturing Science and Engineering Conference*, pp. V003T002A003.
- Jenkins, F. A. & White, H. E., 1958. Fundamentals of optics. *American Journal of Physics*, 26(4), pp. 272-272.
- Kam, K.M., Zeng, L., Zhou, Q., Tran, R. & Yang, J., 2013. On assessing spatial uniformity of particle distributions in quality control of manufacturing processes. *Journal of Manufacturing Systems*, 32(1), pp. 154-166.
- Kim, B. H., Onses, M. S., Lim, J. B., Nam, S., Oh, N., Kim, H., Yu, K. J., Lee, J. W., Kim, J.H. & Kang, S.K., 2015. High-resolution patterns of quantum dots formed by electrohydrodynamic jet printing for light-emitting diodes. *Nano letters*, 15(2), pp. 969-973.
- Kirchhoff, G., 1883. Zur theorie der lichtstrahlen. *Annalen der Physik*, 254(4), pp. 663-695.
- Kwon, K.S. & Lee, D.Y., 2013. Investigation of pulse voltage shape effects on electrohydrodynamic jets using a vision measurement technique. *Journal of micromechanics and microengineering*, 23(6), pp. 065018.
- Liu, C., Law, A.C.C., Roberson, D. & Kong, Z.J., 2019. Image analysis-based closed loop quality control for additive manufacturing with fused filament fabrication. *Journal of Manufacturing Systems*, 51, pp. 75-86.
- Miller, D. A., 1991. Huygens's wave propagation principle corrected. *Optics letters*, 16(18), pp. 1370-1372.
- Mishra, S., Barton, K. L., Alleyne, A. G., Ferreira, P. M. & Rogers, J. A., 2010. High-speed and drop-on-demand printing with a pulsed electrohydrodynamic jet. *Journal of Micromechanics and Microengineering*, 20(9), pp. 095026.
- Nemoto, S., 1989. Waist shift of a Gaussian beam by a dielectric plate. *Applied optics*, 28(9), pp. 1643-1647.
- Onses, M. S., Sutanto, E., Ferreira, P. M., Alleyne, A. G. & Rogers, J. A., 2015. Mechanisms, capabilities, and applications of high-resolution electrohydrodynamic jet printing. *Small*, 11(34), pp. 4237-4266.
- Phung, T. H., Kim, S. & Kwon, K.S., 2017. A high speed electrohydrodynamic (EHD) jet printing method for line printing. *Journal of Micromechanics and Microengineering*, 27(9), pp. 095003.

- Prasetyo, F. D., Yudistira, H. T., Nguyen, V. D. & Byun, D., 2013. Ag dot morphologies printed using electrohydrodynamic (EHD) jet printing based on a drop-on-demand (DOD) operation. *Journal of Micromechanics and Microengineering*, 23(9), pp. 095028.
- Qin, H., Cai, Y., Dong, J. & Lee, Y.S., 2017. Direct printing of capacitive touch sensors on flexible substrates by additive e-jet printing with silver nanoinks. *Journal of Manufacturing Science and Engineering*, 139(3), pp. 031011.
- Qin, H., Dong, J. & Lee, Y.S., 2017. AC-pulse modulated electrohydrodynamic jet printing and electroless copper deposition for conductive microscale patterning on flexible insulating substrates. *Robotics and Computer-Integrated Manufacturing*, 43, pp. 179-187.
- Shannon, C. E., 1998. Communication in the presence of noise. *Proceedings of the IEEE*, 86(2), pp. 447-457.
- Shin, K.Y., Lee, S.H. & Oh, J. H., 2011. Solvent and substrate effects on inkjet-printed dots and lines of silver nanoparticle colloids. *Journal of Micromechanics and Microengineering*, 21(4), pp. 045012.
- Singh, R., Zhang, X., Chen, Y., Zheng, J. & Qin, H., 2018. In-situ real-time characterization of micro-filaments for electrohydrodynamic ink-jet printing using machine vision. *Procedia Manufacturing*, 17, pp. 45-52.
- Wang, T., Kwok, T.-H. & Zhou, C., 2017. In-situ droplet inspection and control system for liquid metal jet 3D printing process. *Procedia Manufacturing*, 10, pp. 968-981.
- Wang, T., Kwok, T.H., Zhou, C. & Vader, S., 2018. In-situ droplet inspection and closed-loop control system using machine learning for liquid metal jet printing. *Journal of manufacturing systems*, 47, pp. 83-92.
- Wei, C., Qin, H., Chiu, C.P., Lee, Y.S. & Dong, J., 2015. Drop-on-demand E-jet printing of continuous interconnects with AC-pulse modulation on highly insulating substrates. *Journal of Manufacturing Systems*, 37, pp. 505-510.
- Wei, C., Qin, H., Ramirez-Iglesias, N. A., Chiu, C.P., Lee, Y.S. & Dong, J., 2014. High-resolution ac-pulse modulated electrohydrodynamic jet printing on highly insulating substrates. *Journal of Micromechanics and Microengineering*, 24(4), pp. 045010.
- Yu, M., Ahn, K. H. & Lee, S. J., 2016. Design optimization of ink in electrohydrodynamic jet printing: Effect of viscoelasticity on the formation of Taylor cone jet. *Materials & Design*, 89, pp. 109-115.

CHAPTER 7. DIMENSION PREDICTION OF ELECTROHYDRODYNAMIC INKJET PRINTED PATTERNS

Authors and Affiliations

Modified from a manuscript to be submitted in Journal of Additive Manufacturing.

This research work was accomplished by Xiao Zhang, Liangkui Jiang, and Hantang Qin. Xiao Zhang, Liangkui Jiang, and Hantang Qin are from the Industrial and Manufacturing Systems Engineering Department at Iowa State University.

Xiao Zhang was leading problem identification, experiment design, proposal of statistical models, conduction of experiment, data analysis, and writing work. Liangkui Jiang contributed to support the experiment, data analysis, and discussion. I want to acknowledge my advisor, Dr. Hantang Qin's support throughout this research work.

Abstract

Electrohydrodynamic inkjet (e-jet) printing is a novel high-resolution additive manufacturing technique for the fabrication of flexible micro and nanoscale electronics such as wearable sensors and devices. However, defects exist during e-jet printing, such as inconsistent quality (e.g., printed feature width) due to environment uncertainties (e.g., substrates may not be flat). This research aims to study multivariable modeling of e-jet printing to help resolve the challenge of depositing patterns with designated dimensions under uncertainties through the adjustment of printing parameters. The e-jet printing applies an electrical field between a conductive nozzle and a substrate to deposit silver nanoink material on the substrate. It was found that the dimension of the deposited pattern could be influenced by several printing parameters. In this study, four printing parameters were selected: frequency, standoff distance, voltage amplitude, and pulse width. The diameters of the deposited silver nanoink droplets were measured by optical microscopy and analyzed by image processing software. The statistical regression model was used to quantitatively analyze the influence of those parameters on the

printing results. The Multivariable E-jet Printing Supervision (MEPS) prediction model was established to predict the printing results with an average prediction accuracy of 87.15% after comparing the prediction and experimental results. In the future, if there is a dimension variation during the printing, an in-situ monitoring camera system could detect the abnormal situation, and the printer could choose corresponding parameters to compensate for this deviation. This research could pave the way to the development of a closed-loop control system.

Introduction

Electrohydrodynamic inkjet printing (e-jet printing) has the advantages of low-cost, high-flexibility, and high-resolution. In the e-jet printing, the electrical force was used to drag the fluid flow from microcapillary nozzles for inkjet printing functional devices with sub-micron resolution (Park 2007). Various functional inks could be used to print intricate patterns by e-jet printing, and this idea has envisioned depositing functional inks on the substrate to fabricate devices such as bio-sensor, electronics, and functional transistors. With years of development, the e-jet printing could enable the fabrication of high-resolution quantum dots light-emitting diodes process (Kim 2015). Transistors were printed with resolution down to $1.5\mu\text{m}$ on SiO_2/Si wafer (Lee 2012). In the electronics manufacturing industry, circuits were fabricated on the silicon-based substrate, which limited the flexibility of electronic products. Our group started to fabricate foldable electronics with the e-jet printing technique, and the multi-layer capacitive touch sensors were fabricated on polyethylene terephthalate (PET) film (Qin 2017). Ink material innovation provided the possibility of e-jet printing applications in the aerospace area. A new tungsten ink material was used to fabricate micro-scale radiation shielding structures by e-jet printing (Lyu 2019). E-jet printing has attracted attention in the biotechnology area due to the high-resolution and flexible operating conditions; functional protein microarrays are useful tools for modern research in medical and biology areas. For example, e-jet printing was used to print

micro/nanoscale patterns of proteins on different surfaces, such as structured plasmonic crystals (Shigeta 2012). E-jet printing was used to fabricate patterned hydrogel substrates for cell culture since cells were sensitive to the environment, such as the geometry of the substrate and stiffness of substrate (Poellmann 2011). E-jet printing was applied to fabricate 3D functional structures such as microcantilever (Pikul 2011), microlens (Sutanto 2014), polymeric scaffold (Wei 2013), tendon tissue (Wu 2014), etc. The most recent review paper has summarized the e-jet printing-related development on the processes, systems on micro/nanoscale manufacturing (Han 2018). Meanwhile, the growing applications required better control over the e-jet printing process.

To fabricate patterns with higher quality, our group used AC-pulse modulated e-jet printing to overcome the remained charge of the printed droplet and demonstrated reliable jet printing on highly insulated substrates (Wei 2015; Wei 2014; Qin 2017). The printed pattern's quality could be improved by changing the voltage type; sensing and controlling system is another approach. Iterative Learning Control algorithm was used as a feedforward voltage signal and applied feedback controller to compensate for uncertainty in the printing process (Barton 2011). Machine vision is another powerful tool to provide input information for controlling the inkjet printing process with a CMOS camera (Singh 2018; Zhang 2019). Although these methods could monitor the printing process, the influence of printing parameters on the dimension of deposited features has not been fully understood.

There are several known printing parameters which could influence the fabricated patterns, such as plotting speed (Ding 2017), standoff distance (Tse 2015), nozzle diameter (Graf 2011), voltage amplitude (Onses 2015), voltage frequency (Choi 2008) and pulse width (Qin 2016). The e-jet printing parameters' effect on the droplet size was studied, and a model was established to predict the droplet size (Laurila 2017). It was apparent that all these printing

parameters could influence the deposited pattern's size. The statistical relationship between all those parameters and the deposited patterns could enable the e-jet printing to fabricate patterns of controllable sizes. The restructured artificial bee colony optimizer was used to predict the droplet volume and velocity for the fabrication of high-resolution electronics in the piezoelectric drop-on-demand inkjet printing process (Jing 2018). Taguchi optimization approach and ANOVA method were used to find the best parameters in printing ceramic coatings on a glass substrate. It was found that increasing nanoparticle concentration could result in an improvement in the thickness of the layer (Rahul 2017). In the design and manufacturing process, statistical analysis of the fused deposition process could also contribute to optimization and prediction (Rayegani 2014). In the novel ultrasonic additive manufacturing process, statistical characterization of process parameters such as normal force, oscillation amplitude, weld speed, and the number of bilayers contributed to the establishment of a model to predict the bond strength (Hopkins 2010). A different statistical model was also applied in the prediction of printed results, such as spatial Gaussian process models (Tapia 2016).

In this research, voltage amplitude, pulse width, frequency, and standoff distance were selected as printing parameters to predict the diameter of printed silver nanoink. The statistical analysis was provided to present the mathematical relationship between printing variables and the dot diameter. A Multivariable E-jet Printing Supervision (MEPS) prediction model was established to predict the diameter of printed droplets. The understanding of the printing parameters and establishment of the prediction model could contribute to the feedback control of the e-jet printing system.

Experiment setup

Mechanism of e-jet printing

To fabricate intricate patterns on the substrate, the e-jet printer was designed based on the particular requirement of depositing liquid material by electrical force, such that it can print with high resolution and control the dimensions of the pattern. As shown in Figure 1, the e-jet printer has several main components: movement stage, ink supply subsystem, electrical field generation subsystem, printing substrate, camera subsystem, and central computer control. The printing platform has a resolution of 50 nm. The conductive ink material was stored in the ink supply subsystem. Conductive needles were manufactured with a tip diameter ranging from 1 μ m to 100 μ m according to the printing requirements. The signal generator was connected with the voltage amplifier to provide a digital voltage signal. In this study, the glass slide was glued on the platform as the printing substrate for samples. Thus, a camera with the lens was used to monitor the printing process. A central computer was deployed to control the camera, signal generator, and stage movement. During the printing, conductive ink started to form a Taylor cone shape at the needle tip under the electrical force. As the growing of electrical force, the Taylor cone shape was dragged into a long filament. Then the filament separated with the needle tip and formed a droplet in the air. The conductive ink material was deposited onto the substrate in one pulsed circle when pulsed AC voltage was applied. Voltage amplitude, pulse width, standoff distance, and printing frequency significantly influence the diameter of the printed droplet. The silver nanoparticle ink contained 50wt. % dispersion in tripropylene glycol, and was uniformly dispersed in the solvent for e-jet printing. The average diameter of silver nanoink particle is around 50nm.

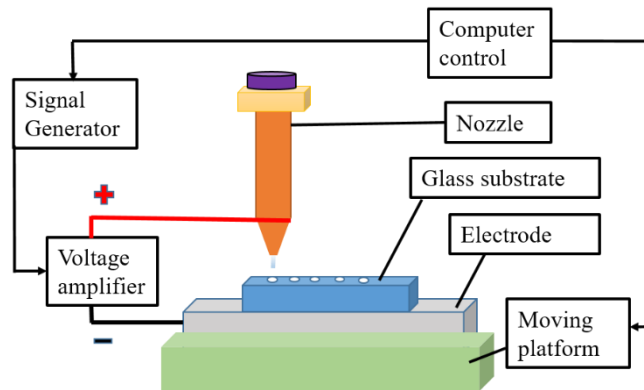


Figure 43. Schematic of e-jet printing system setup: droplets were deposited onto the glass substrate by the electrical force

Printing parameters and data collection

E-jet printing enables the flexible fabrication of electronics in various fields. It is crucial to control the dimension of the printed patterns. Accordingly to our group's previous research work: pulse width, voltage amplitude, printing frequency, and standoff distance. However, it is still unknown how these parameters are quantitatively influencing the dimension of printed results. The physical essence of e-jet printing has enlightened us on selecting major influential factors during the printing process. There are other influential factors such as ink properties, plotting speed, nozzle diameter, nozzle shape, the setup of the electrode, the printing substrate, the resolution of the moving platform, and the operator's human error. Plotting speed refers to the movement speed of the stage, which does not have a direct correlation with the size of the deposited droplet. A bigger nozzle diameter would tend to generate larger droplets. In this study, we selected influential factors to simplify the statistical model for the prediction of the dimension. All other variables (including nozzle diameter, nozzle shape, etc.) were already optimized. Silver nanoink was selected for in these experiments due to its wide application in the e-jet printing area, and the printing substrate is the glass slide for easy measurements of printed results. The same operator used the same movement platform in this study.

The preparation of e-jet printing, fabrication, and data collection process was presented in the flowchart of Figure 44. The ink was prepared and stored in the nozzle for printing. The droplet was then dragged by electrical force and deposited on the substrate. A camera with an amplification lens was used to observe the needle and printing. The camera was applied to monitor the droplet deposition process. After printing, substrates will be removed from the stage and observed by optical microscopy. The operating range for each of the printing parameters was identified first. After the selection of target parameters, the g-code was programmed for the printing. To ensure the repeatability of the experiment, multiple data collections have been conducted during measurement.

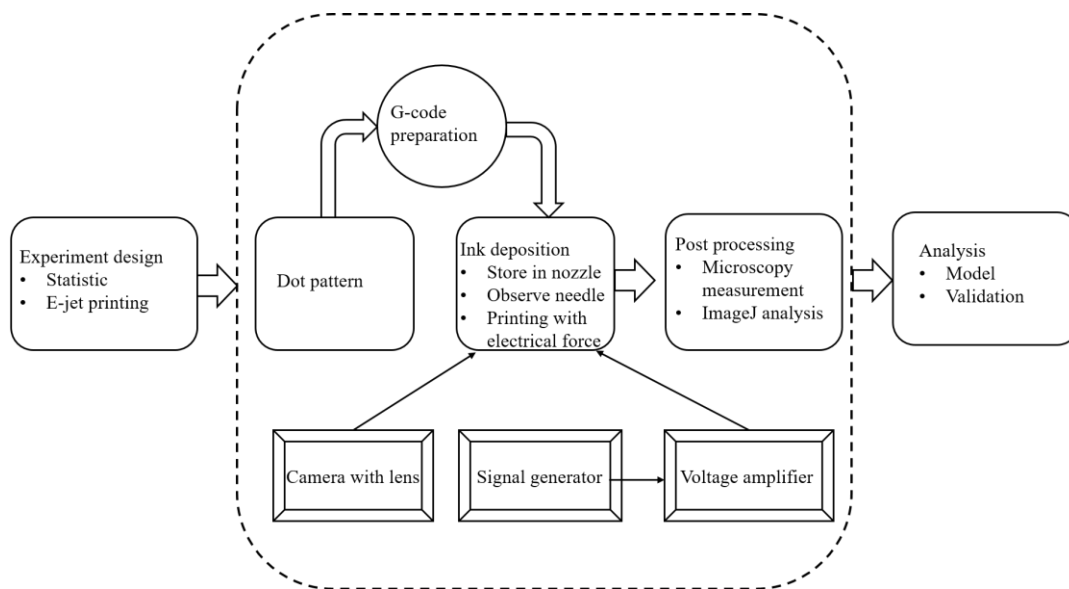


Figure 44. Chart of e-jet printing and data flow

Experiment design

The diameter of the deposited droplet was defined as the dimension of the printing result. A pulsed voltage was used in the experiments. Variables are defined as follows: voltage amplitude (VO), pulse width (PU), frequency (FR), standoff distance (SD), and diameter of the deposited droplet (D). Initial printing experiments were conducted to identify the proper working

range of the four key printing parameters. For example, an increase in voltage value could increase the dimension of the printed sample. The droplets started to generate when the voltage was at 600V. When the voltage reached an upper value (750V), excessive ink will flow out the nozzle, and the e-jet mechanism cannot be maintained. A 50V interval was set to be the difference between each voltage level until the voltage was 750V. Pulse describes the time of the voltage lasts during one cycle of the voltage signal. Pulse width has a similar effect on the e-jet printed results as voltage amplitude. When the voltage was 600V, the droplet could barely generate when the pulse width was 200 μ s. When the pulse width was higher than 400 μ s, too much conductive ink tends to flow out on the substrate. Then a 50 μ s interval was selected to ensure good quality of printing results (e.g., the circularity of the printed dots). The plotting speed was 10 mm/s. The diameter of the glass needle was 35 μ m. Table 6 has presented the values for each level of printing parameters. The design of experiment is a full factorial experiment that takes on all possible combinations of these four levels for each of the printing parameters.

Table 6. E-jet printing parameters

| Parameters/Level | L1 | L2 | L3 | L4 |
|------------------------|------|-------|-----|-------|
| Voltage (V) | 600 | 650 | 700 | 750 |
| Pulse width (μ s) | 200 | 250 | 300 | 350 |
| Frequency (Hz) | 20 | 30 | 40 | 50 |
| SD distance(μ m) | 52.5 | 61.25 | 70 | 78.75 |

After determining the range of the printing parameters, experiments considering all possible combinations of parameters were designed for statistical analysis. The 256 groups of experiments were performed based on all combinations of parameters in Table 6. Considering the repeatability of the experiment, each printing parameter combination needs to have three data points. 768 groups of experimental conditions were tested in this study.

Statistical design

The research question is how the printing parameters influence the dimension of deposited droplets. Statistical tools such as multiple regression were used to analyze the generated data. Multiple regression analysis could predict the value of one scalar variable based on one or multiple variables. The diameter of the droplet is the scalar variable in this study. The voltage amplitude, pulse width, frequency, and standoff distance are the multiple variables that could influence the dimension of the printed droplet. For each of these variables, there are four levels: level 1, level 2, level 3, and level 4. These four levels have covered the full range of selected printing parameters. For example, voltage values were selected from 600V to 750V, and four levels include the voltage values of 600V, 650V, 700V, and 750V. Theoretically, the highest range of droplet dimensions could be achieved under this setup because test experiments found the largest values and smallest values of each printing parameters. The multiple regression model is as shown as Equation (1).

$$y = a_1X_1 + a_2X_2 + \dots + a_nX_n + b \quad \text{Equation 1}$$

where a_i represents the coefficient of the variable, the value of the coefficient describes to what weight the variable would influence the y-value. R^2 value describes the square measurement of association between variable X_i and y value. The influence of each e-jet printing parameter does not necessarily have a linear impact on the dimension of the dimension. Multiple linear regression models did not consider the correlation influence between each parameter, and it did not include the square of the printing parameter's influence. Thus, the following equation was also studied:

$$y = a_1X_1 + c_1X_1^2 + d_1X_1X_2 + a_2X_2 + c_2X_2^2 + d_2X_2X_3 + \dots + a_nX_n + c_nX_n^2 + b \quad \text{Equation 2}$$

Results and discussion

The qualitative trend of printing parameters such as voltage amplitude, standoff distance has been investigated by our previous research. However, limited research has been conducted to provide statistical analysis for quality prediction. Droplets dimension was used in e-jet printing experiments (Laurila 2017). The printing quality in this article was relatively low and the dimension was defined as the prediction target since the printed droplet was not a round shape. It could be further improved by improving printing quality and defining the diameter of the droplet for prediction. To establish a close-loop e-jet printing system, it is crucial to know how the system could control the dimension of printed patterns. There are various variables in e-jet printing. The experiment data were fitted into the ANOVA to test whether to reject the null hypothesis that the model predicted diameter was the same as the experiment data for all of the printing conditions.

E-jet printing results

The waveform in this study is the pulsed signal, as shown in Figure 45. The pulse peak represented the voltage amplitude. The time length of one pulse is the pulse width of the signal. The number of pulses in one second is the frequency. Standoff distance is the distance from the nozzle tip to the glass substrate. Each printing condition was conducted on three lines, and each line was 5mm. The printed substrates were taken images by microscopy under the same light condition and the same scale to avoid the possible errors in the measurement. Then these images were analyzed in ImageJ for calculation of the diameter by using particle analysis function. Droplets would be averaged to represent the diameter at that data point.

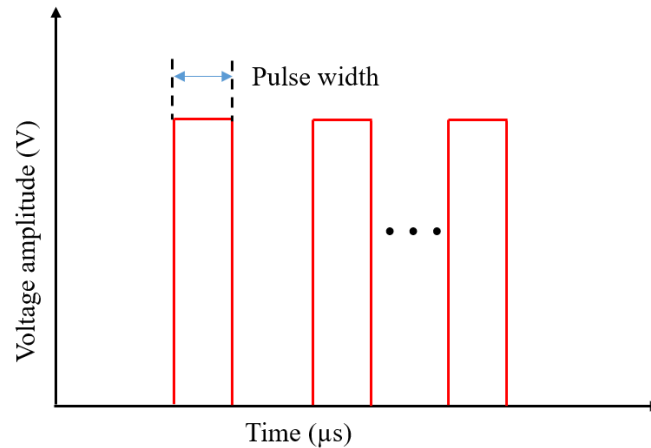


Figure 45. E-jet printing of signal waveform

Before finalizing the range of the printing parameters, pre-printing experiments were conducted to find the optimized data set. Previous research has provided the information that larger voltage amplitude, larger pulse width could generate a larger droplet on the substrate. If the frequency number is larger, the printed pattern tends to form the line pattern if the plotting speed is fixed. Larger standoff distance could generate smaller droplet diameter because the electrical force is weaker if the standoff distance is larger. It was necessary to figure out the balanced values of printing parameters, which could cover a larger range for each variable in this study. Based on the known mechanism of e-jet printing, several testing rounds of experiments were conducted to find both the small droplet and the big droplet. The primary judgment rule is that the droplet could still generate to form a dot pattern on the substrate to form a small droplet, and the droplet could still be controlled to form a big dot on the substrate without flushing. Thus before the printing experiment started, it could be possible to figure out the values for each of the printing parameters.

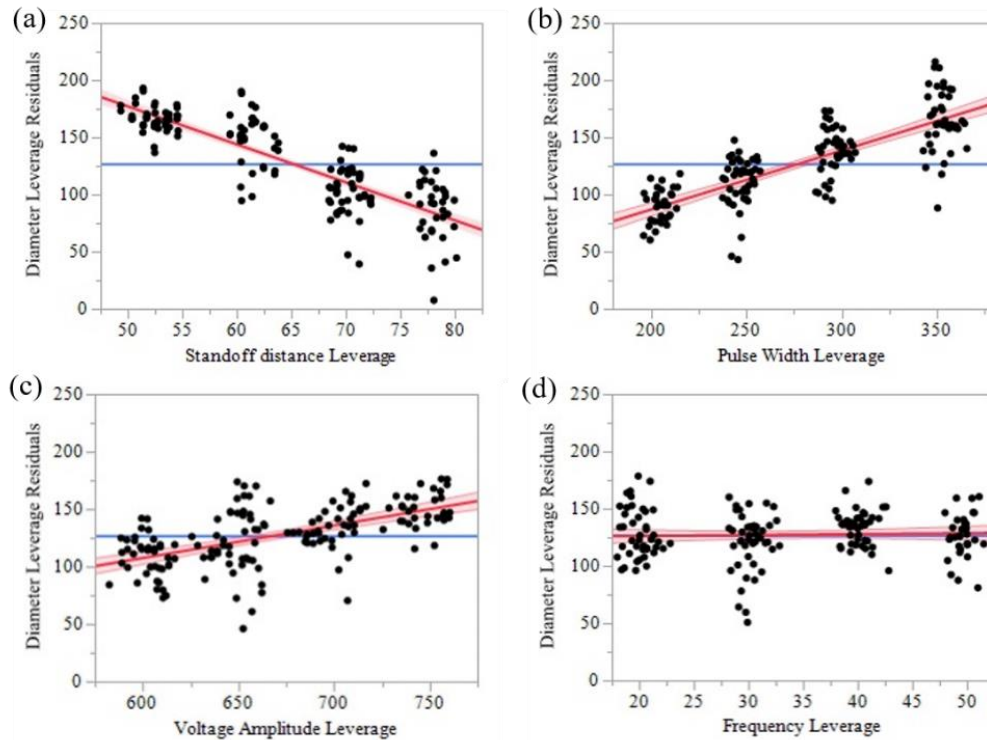


Figure 46. Leverage residual analysis considering the leverage of (a) Standoff distance, (b) Pulse width, (c) Voltage amplitude, (d) Frequency

After the collection and analysis of printed droplet, there were some data points which need to be removed. Firstly, there were specific printing parameter combinations that do not deposit materials. For example, when the printing happened at a considerable standoff distance and low voltage, there was no deposition at all due to low electrical forces. Secondly, some printed circle was not round shape. This phenomenon happened in circumstances where plotting speed and printing frequency were not tuned properly. There are 492 data points calculated and fitted into the multi regression model. Data was fed into the multi regression model and generated the leverage residual map for each of the printing parameters. The leverage residual reflects the sensitivity of the influence of the variable on the dimension of the deposited dots. The diameter of the printed dots was between $50\ \mu\text{m}$ and $200\ \mu\text{m}$, as shown in Figure 4.

From Figure 46, it could be observed that pulse width and standoff distance have a relatively larger influence on the dimension. The value of pulse width represents the time of voltage exerted on the electrode. A larger pulse width could result in a more extended electrical field existed in one signal cycle for printing, then more material would flow out of the nozzle. Standoff distance is the distance between the needle tip and the glass substrate. A larger standoff distance could influence the distribution of the electrical field. Ultimately, the electrical force will be significantly influenced due to the change in the electrical field. The voltage amplitude in Figure 46(c) presented a smaller slope, which results in a diameter ranging from 100 μm to 150 μm . From our previous experiments, voltage amplitude had a significant influence on the flowing of the ink material and could easily result in the Siphon phenomenon. However, to accomplish the prediction of the dimension, a balanced selection of values has to be determined. The frequency has little influence on the printing results. Frequency represents the number of signals sent to the voltage amplifier during one second. Theoretically, the larger frequency had more times of dragging on the material. However, the actual situation could be different due to the physical essence of e-jet printing. Because of the surface tension effect, sometimes, one signal may be able to form a Taylor cone, but it could not separate the material from the needle and print on the substrate. From these data sets, frequency is not sensitive to the dimension of the deposited dots.

Result of original data calculation

In Figure 47, the diameter mean and standard error of the diameter mean are plotted regarding different printing parameters (standoff distance, pulse width, voltage amplitude, and frequency). Depending on this study, a confidence level of 95% is used for the data presented below. The mean diameter decreases with the increase of standoff distance. The standoff distance determines the intensity of electrical force during e-jet printing. Thus, a higher standoff

distance will generate a weaker electrical force, resulting in less material deposited on the substrate. Voltage amplitude and pulse width have a positive influence on the electrical force. It could be observed that the diameter mean increases with bigger voltage amplitude and pulse width. The plotting frequency defined the number of signals sent in one second. When the plotting frequency continues to increase, the printed pattern will be a line pattern. The plotting frequency does not conduct an evident influence on the printed results, according to Figure 47 (d), when the plotting frequency is between 20 Hz to 50 Hz.

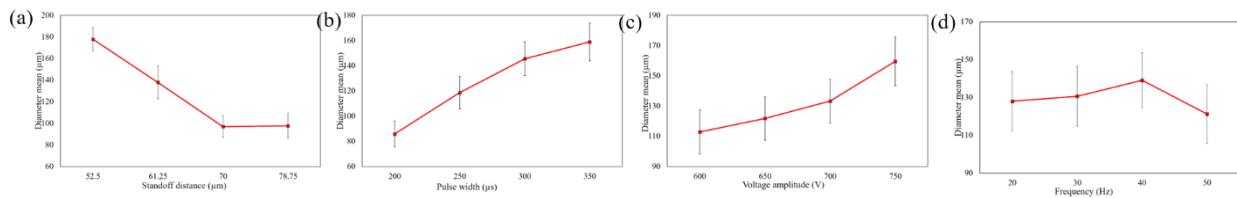


Figure 47. Diameter mean plotting of different printing parameters: (a) Standoff distance at 52.5 μm , 61.25 μm , 70 μm , 78.75 μm (b) Pulse width at 200 μs , 250 μs , 300 μs , 350 μs , (c) Voltage amplitude at 600 V, 650 V, 700 V, 750 V, (d) Frequency at 20 Hz, 30 Hz, 40 Hz, 50 Hz

Result of fitted data

The least square mean plots for each of the four printing parameters have been presented in Figure 48. Four plotting groups are sharing the same data set. It is assumed that there is a relationship between the printing parameters and the deposited dot diameter. The nature of least square mean defines the similar error range for each data point at the least square value. Each data point in the graph shows the most probable printed dot diameter under this parameter combination. The least-square means value of the diameter was around 100 μm when the voltage is 600V. The standard deviation error was around 15 μm for all other voltage values at 650V, 700V, 750V. The LS mean value of diameter becomes larger with the increase of voltage amplitude. A larger electrical field could generate a larger electrical force which will finally

deposit more ink material on the substrate. The pulse width has a similar effect on influencing the trend of the dot diameter. The pulse width defines the length of time used to drag the ink in one pulse cycle. The least-square mean value of diameter is similar when the frequency was ranging from 20Hz to 50Hz. The variation was in a small range for printing frequency from 20Hz to 50Hz. In Figure 48(a), the diameter decreases with the increase of standoff distance. A higher standoff distance will result in a weaker electrical force for dragging the metal ink. Less ink material could be deposited on the substrate, which will form a small dot. Frequency does not have an obvious influence on the dot diameter based on this data set.

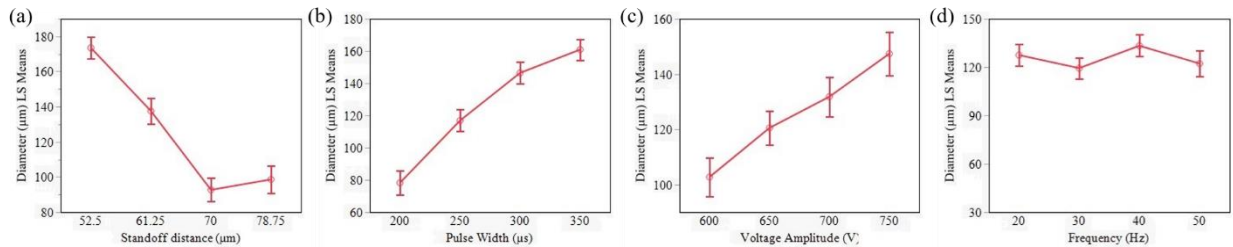


Figure 48. Least square mean plotting of different printing parameters: (a) Standoff distance at 52.5 μm , 61.25 μm , 70 μm , 78.75 μm (b) Pulse width at 200 μs , 250 μs , 300 μs , 350 μs , (c) Voltage amplitude at 600 V, 650 V, 700 V, 750 V, (d) Frequency at 20 Hz, 30 Hz, 40 Hz, 50 Hz

Multivariable e-jet printing supervision (MEPS) prediction model

Single parameter influence could assist the explanation of the dimension trend of printed patterns. But e-jet printing is a complex physical fabrication process that contains multiple influential printing parameters. In Figure 49, the correlation influence of each parameter on dimension was analyzed. In each grid, different colors gave the audience the different value of the y-axis. For example, the second grid on the first row, voltage amplitude is the y-axis, and the pulse width is the x-axis. The diameter of the dot increased when the voltage amplitude started to increase from 600V to 750V in Figure 49. From the observation of row 2, all different color lines are almost overlapped. This minor difference between each line means that different frequencies

of 20Hz or 50Hz did not influence the dimension of the droplet. The difference on the y-axis for each line indicates the influence of parameter on the y-axis. The pulse width has the highest variation when considering the standoff distance and the rest of the printing parameters. Voltage amplitude has a higher variation compared with the frequency if we observe the row 2 and row 4. The interval of pulse width was 50 μ s, and the interval of voltage amplitude was 50V. This variation of the diameter was measured under the selected working range. For example, the pulse with values was selected from 200 μ s to 350 μ s, and voltage amplitude values were selected from 600V to 750V. The bigger variation in pulse width could due to the absolute increase in pulse width value compared with voltage amplitude. When analyzing the second column of Figure 49, it could be seen that the voltage amplitude increase could near linearly increase the dot diameter. But it is not the same case for pulse width and standoff distance. The third column also reflected the trend for the voltage amplitude. On the other hand, if we observe this graph horizontally, it could be seen how the x-variable influence the dimension at different y-variable.

After fitting the data into the model in the JMP, the summary of the model was presented in Table 7. The Logworth value represented the effect each printing parameter contributed to the dimension. The p-value represents the evidence against the null hypothesis. The null hypothesis could provide the reference if the printing variable has a determining influence on the dimension of printed results when the p-value is smaller, the more substantial the evidence that should reject the null hypothesis. If the p-value is less than 0.05, then it means that there is a significant difference exists. R^2 value presents the proportion of variation in the dependent variable that is predictable from the independent variable. When the R^2 values are larger, the prediction function is more reliable for the calculation of the ink dimension.

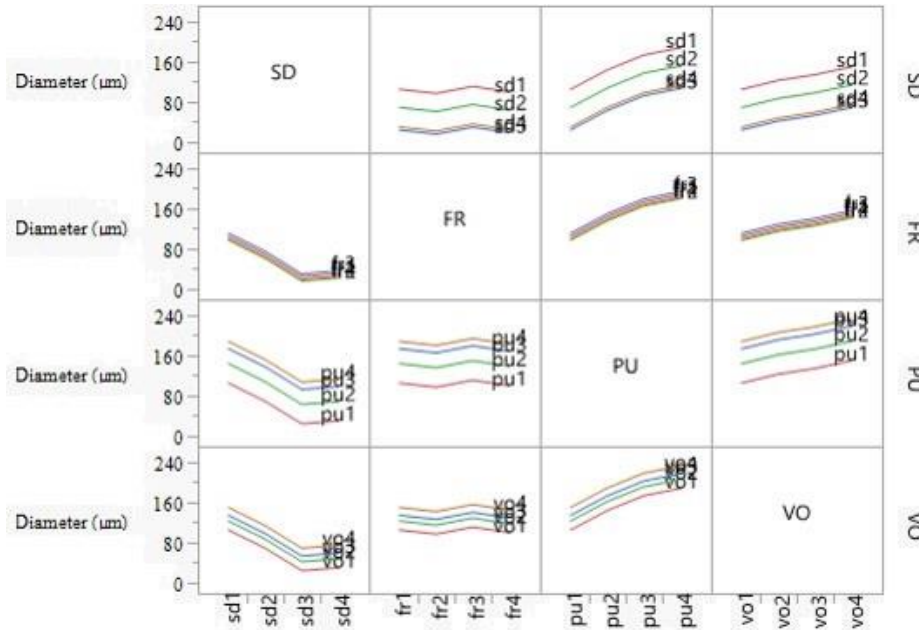


Figure 49. Interaction plot of pattern diameter versus different e-jet printing parameters

Table 7. Effect of e-jet printing parameter on the dimension and the square value of the function

| Effect summary | | | Summary of Fit | |
|----------------|----------|--------|--------------------|---------|
| Source | Logworth | Pvalue | R ² | 0.836 |
| SD | 45.516 | 0 | R ² Adj | 0.829 |
| PU | 36.672 | 0 | | |
| VO | 15.947 | 0 | | |
| PU*SD | 8.262 | 0 | Root Mean Square | 21.706 |
| SD*SD | 7.493 | 0 | Error | |
| PU*PU | 2.695 | 0 | Mean of Response | 129.895 |
| FR | 0.100 | 0.795 | | |

The multivariable E-jet Printing Supervision (MEPS) prediction model was established based on multiple printing parameters' effect on the dimension of fabricated patterns. The experiment was conducted based on various combinations of different values to set up example inputs for the prediction model. The first round of model fitting was prepared by JMP. There are four single variables (VO , PU , SD , FR), four square variables (VO^2 , PU^2 , SD^2 , FR^2), six correlate variables ($VO * PU$, $VO * SD$, $VO * FR$, $PU * SD$, $PU * FR$, $SD * FR$). After fitting into the model, it was found that only part of these variables has t-values lower than 0.05. Thus, another

round of fitting models, which considered the SD , PU , VO , $PU * SD$, $SD * SD$, $PU * PU$, and FR , were conducted. SD has a weight value of 45.516 from the statistical model analysis. This highest-value means that the standoff distance has the most significant influence on the diameter. It could be the selection of different standoff distances has a significant variation in the variation of dimension. The frequency has a large p-value; there is no significant relationship between the frequency and the predicted value of the printed dimension of patterns. If the plotting speed is higher, then there will still be a dot generated on the substrate. Thus, only pulse width and voltage amplitude influence on generating the droplets under the same standoff distance.

The data was fed into a variety of modes, which are considered a single parameter variable, correlated parameter variable, and the second order of the parameter variable. The results were compared and analyzed to reach the optimized fitting of the function. After the calculation, the MEPS mathematic function, as shown below:

$$D = 0.283 * VO + 0.517 * PU - 3.322 * SD + 0.083FR + 0.132 * (SD - 64.985) * (SD - 64.985) - 0.002 * (PU - 278.354) * (PU - 278.354) - 0.020 * (PU - 278.354) * (SD - 64.985)$$

Equation 3

Ten groups of random data points were randomly prepared for verification purposes. These data points were selected from the previous experiments. The values of voltage amplitude, standoff distance, pulse width, and frequency were calculated in Equation 3. The calculated value of the specific data point would be considered as the prediction diameter under that printing condition. All the data were demonstrated in Table 3 for comparison. The smallest error was around 0.5%. There were ten groups of data, which were shown in table 3 with a prediction number. The average prediction accuracy rate was 87.15% under the current e-jet printing setup. Previous research claimed to have a similar accuracy rate (Laurila et al. 2017). Still, as

mentioned, the printing conditions were not optimized in the previous article, and printing quality (circularity) was poor. Laurila et al. predicted based on the measurement of the width of the droplet that may cause significant measurement errors. In this study, there are four levels in each printing parameter, which have one more level than the study from Laurila et al. More levels of different printing parameters could provide more evidence for the understanding of the variable of dimension.

Table 8. Experiment and prediction data comparison

| Group No. | 1 | 2 | 3 | 4 | 5 | 6 | 7 | 8 | 9 | 10 |
|-----------------------------------|--------|--------|--------|--------|--------|--------|--------|--------|--------|--------|
| Experiment data (μm) | 205.79 | 184.59 | 137.05 | 208.06 | 201.48 | 213.40 | 197.34 | 175.33 | 109.05 | 86 |
| Prediction data (μm) | 206.88 | 178.70 | 133.97 | 236.84 | 209.37 | 188.98 | 161.51 | 142.09 | 149.02 | 109.05 |
| Difference (μm) | 1.09 | 5.89 | 3.08 | 28.78 | 7.88 | 24.41 | 35.83 | 33.245 | 39.974 | 23.05 |
| Percentage Difference (%) | 0.5 | 3.3 | 2.3 | 12.2 | 3.8 | 12.9 | 22.2 | 23.4 | 26.8 | 21.1 |
| Percentage average | 12.85 | | | | | | | | | |

Although multiple methods used the finite element method to simulate the e-jet printing process and predict the deposited material, the e-jet printing process's physical nature is highly complex. It is almost impossible to consider all factors such as the electrode, printing substrate, material, nozzle shape, dust in the air, control systems, human operation error, temperature, and humidity in the micro/nano-scale printing process. The statistical approach could still provide another aspect for the research to investigate the influence of printing parameters on deposited pattern dimension. However, the results are not very consistent for every prediction. For example, in table 8, the difference between prediction data and measured data is larger from group seven to group ten compare with the first few groups. Each data point was selected for verification purposes from group one to group ten in every 10 data points. So data point group one was selected when the e-jet printing just started during this full factorial experiment. The

data point in group ten was lastly printed out of all these selected data points. Random selection was ensured through this process. It has to be claimed that the whole experiment process was finished in around six hours.

The dust could influence the tip of the nozzle in the air. If any dust is attached to the nozzle tip, the ink deposition will be different. Usually, the metal is stored in a dark and encrypted container. The solvent material in the metal ink could evaporate and then change the status of the nozzle tip. The metal ink deposition is a microscale flow process. Thus any variation in the nozzle tip will result in a different amount of deposited ink on the substrate. While the error could be the claimed reasons, there are other factors, such as the electrode shape. The electrode used in this experiment is not parallel. The electrode shape can change the electrical field exerted on the metal ink. The linear model could not accurately predict the dimension, while the machine learning models would require a super larger data set that is challenging under the current e-jet printing experiment setup. The model in this research has revealed the nonlinear relationship between multiple printing parameters and the dimension based on a fair amount of data set. This research has presented the statistical approach to predict the e-jet printing printed patterns by conducting the full factorial experiment and four printing parameters. In the future, optimized experiments shall be conducted to improve prediction accuracy and consistency.

In this study, the prediction target was defined as the diameter of the printed droplet. The accuracy was as high as 87.15% under four levels of each printing parameter were considered in the conduction of e-jet printing experiments. The prediction of a dot could help calculate the amount of material deposited on the substrate if we assume the thickness of the deposited ink was constant. Once a defect was found during the fabrication process, the controller could send signals to reverse the trend and fix the problem. This setup of experiments could be used as a

reference to establish a statistical model for prediction purposes. For example, different ink types, substrate, electrode type, and signal type could be labeled as a different level in the model to establish a more comprehensive prediction system. Successful printing of dot patterns could contribute to the fabrication of patterns with a regular line width. These uniform lines are the necessary components of intricate electronic patterns. By utilizing the MEPS model, a closed-loop e-jet printing system could be established to print high-resolution, delicate, and defect-free patterns for the manufacturing of flexible electronics.

Conclusion

E-jet printing has the advantages of high-resolution, low-cost, and flexible characteristics. However, limited research was conducted to understand the quantitative influence of printing parameters on the dimension of fabricated patterns. The e-jet printing fabrication is a complex physical deposition process based on the electrical field to generate droplets. In this research, the dot diameter was predicted based on the establishment of a statistical regression model in the e-jet printing process. The pulse width, standoff distance, voltage amplitude, and frequency were selected with each printing parameter under four different levels of values in the e-jet printing process. After the analysis of printing results, the least square mean plotting presented the nearly linear increase relationship between voltage amplitude, standoff distance, pulse width, and dot diameter. The correlated influence of two printing parameters on the dimension was presented in the matrix map. A further calculation of the results contributes to the establishment of the MEPS function based on a multi-parameter regression model with an average accuracy of 87.15% compared with experimental data. In the future, the establishment of the closed-loop system is vital for the industrialization of the e-jet printing technique. This research could serve as the basic component of the closed-loop e-jet printing system by providing the instruction of feedback control.

References

- Barton, K., Mishra, S., Alleyne, A., Ferreira, P. & Rogers, J., 2011. Control of high-resolution electrohydrodynamic jet printing. *Control Engineering Practice*, 19(11), pp. 1266-1273.
- Choi, H., Park, J., Park, O., Ferreira, P., Georgiadis, J. & Rogers J., 2008. Scaling laws for jet pulsations associated with high-resolution electrohydrodynamic printing. *Applied Physics Letters*, 92(12), pp. 123109.
- Ding, H., Zhu, C., Tian, L., Liu, C., Fu, G., Shang, L. & Gu, Z., 2017. Structural color patterns by electrohydrodynamic jet printed photonic crystals. *ACS applied materials & interfaces*, 9(13), pp. 11933-11941.
- Graf, P., 2011. A 2nd generation electrohydrodynamic jet (e-jet) printing system, parametric studies of e-jet nozzles and integrated electrode e-jet deposition. Master thesis, <https://www.ideals.illinois.edu/handle/2142/24288>.
- Han, Y. & Dong J., 2018. Electrohydrodynamic printing for advanced micro/nanomanufacturing: current progresses, opportunities, and challenges. *Journal of Micro and Nano-Manufacturing*, 6(4).
- Hopkins, C., Dapino, M. & Fernandez, S., 2010. Statistical characterization of ultrasonic additive manufacturing Ti/Al composites. *Journal of Engineering Materials and Technology*, 132(4), pp. 041006.
- Jing, S., Ma, L., Hu, K., Zhu, Y. & Chen, H., 2018. A restructured artificial bee colony optimizer combining life-cycle, local search and crossover operations for droplet property prediction in printable electronics fabrication. *Journal of Intelligent Manufacturing*, 29(1), pp. 109-134.
- Kim, B., Onses, M., Lim, J., Nam, S., Oh, N., Kim, H., Yu, K., Lee, J., Kim, J., Kang, S. & Lee, C., 2015. High-resolution patterns of quantum dots formed by electrohydrodynamic jet printing for light-emitting diodes. *Nano Letters*, 15(2), pp. 969-973.
- Laurila, M., Khorramdel, B., Dastpak, A. & Mäntysalo, M., 2017. Statistical analysis of E-jet print parameter effects on Ag-nanoparticle ink droplet size. *Journal of Micromechanics and Microengineering*, 27(9), pp. 095005.
- Lee, S., Kim, J., Choi, J., Park, H., Ha, J., Kim, Y., Rogers, J. & Paik U., 2012. Patterned oxide semiconductor by electrohydrodynamic jet printing for transparent thin film transistors. *Applied physics letters*, 100(10), pp. 102108.
- Lyu, H., Zhang, X., Liu, F., Huang, Y., Zhang, Z., Jiang, S. & Qin, H., 2019. Fabrication of micro-scale radiation shielding structures using tungsten nanoink through electrohydrodynamic inkjet printing. *Journal of Micromechanics and Microengineering*, 29(11), pp. 115004.

- Onses, M., Sutanto, E., Ferreira, P., Alleyne, A. & Rogers, J., 2015. Mechanisms, capabilities, and applications of high-resolution electrohydrodynamic jet printing. *Small*, 11(34), pp. 4237-4266.
- Park, J., Hardy, M., Kang, S., Barton, K., Adair, K., Kishore, D., Lee, C., Strano, M., Alleyne, A., Georgiadis, J. & Ferreira, P., 2007. High-resolution electrohydrodynamic jet printing. *Nature materials*, 6(10), pp. 782.
- Pikul, J., Graf, P., Mishra, S., Barton, K., Kim, Y., Rogers, J., Alleyne, A., Ferreira, P. & King, W., 2011. High precision electrohydrodynamic printing of polymer onto microcantilever sensors. *IEEE Sensors Journal*, 11(10), pp. 2246-2253.
- Poellmann, M., Barton, K., Mishra, S. & Johnson, A., 2011. Patterned hydrogel substrates for cell culture with electrohydrodynamic jet printing. *Macromolecular bioscience*, 11(9), pp. 1164-1168.
- Qin, H., 2016. Development of High Resolution Rapid Prototyping Method for Flexible Electronic Devices Based on Electrohydrodynamic Inkjet Printing. Ph.D. thesis, <https://repository.lib.ncsu.edu/bitstream/handle/1840.20/33289/etd.pdf?sequence=1>.
- Qin, H., Cai, Y., Dong, J. & Lee, Y., 2017. Direct printing of capacitive touch sensors on flexible substrates by additive E-Jet printing with silver nanoinks. *Journal of Manufacturing Science and Engineering*, 139(3), pp. 031011.
- Qin, H., Dong, J. & Lee, Y., 2017. AC-pulse modulated electrohydrodynamic jet printing and electroless copper deposition for conductive microscale patterning on flexible insulating substrates. *Robotics and Computer-Integrated Manufacturing*, 43, pp. 179-187.
- Rahul, S., Balasubramanian, K. & Venkatesh, S., 2017. Optimizing inkjet printing process to fabricate thick ceramic coatings. *Ceramics International*, 43(5), pp. 4513-4519.
- Rayegani, F. & Onwubolu, G., 2014. Fused deposition modelling (FDM) process parameter prediction and optimization using group method for data handling (GMDH) and differential evolution (DE). *The International Journal of Advanced Manufacturing Technology*, 73(1-4), pp. 509-519.
- Shigeta, K., He, Y., Sutanto, E., Kang, S., Le, A., Nuzzo, R., Alleyne, A., Ferreira, P., Lu, Y. & Rogers, J., 2012. Functional protein microarrays by electrohydrodynamic jet printing. *Analytical chemistry*, 84(22), pp. 10012-10018.
- Singh, R., Zhang, X., Chen, Y., Zheng, J. & Qin, H., 2018. In-situ real-time characterization of micro-filaments for electrohydrodynamic inkjet printing using machine vision. *Procedia Manufacturing*, 17, pp. 45-52.
- Sutanto, E., Tan, Y., Onses, M., Cunningham, B. & Alleyne, A., 2014. Electrohydrodynamic jet printing of micro-optical devices, *Manufacturing Letters*, 2(1), pp. 4-7.

- Tapia, G., Elwany, A. & Sang, H., 2016. Prediction of porosity in metal-based additive manufacturing using spatial Gaussian process models. *Additive Manufacturing*, 12, pp. 282-290.
- Tse, L. & Barton, K., 2015. Airflow assisted printhead for high-resolution electrohydrodynamic jet printing onto non-conductive and tilted surfaces. *Applied Physics Letters*, 107(5), pp. 054103.
- Wei, C. & Dong, J., 2013. Direct fabrication of high-resolution three-dimensional polymeric scaffolds using electrohydrodynamic hot jet plotting. *Journal of Micromechanics and Microengineering*, 23(2), pp. 025017.
- Wei, C., Qin, H., Chiu, C., Lee, Y. & Dong, J., 2015. Drop-on-demand E-jet printing of continuous interconnects with AC-pulse modulation on highly insulating substrates. *Journal of Manufacturing Systems*, 37, pp. 505-510.
- Wei, C., Qin, H., Ramirez-Iglesias, N., Chiu, C., Lee, Y. & Dong, J., 2014. High-resolution ac-pulse modulated electrohydrodynamic jet printing on highly insulating substrates. *Journal of Micromechanics and Microengineering*, 24(4), pp. 045010.
- Wu, Y., Wang, Z., Ying, J., San, Y., Wang, W. & San, E., 2017. Direct E-jet printing of three-dimensional fibrous scaffold for tendon tissue engineering. *Journal of Biomedical Materials Research Part B: Applied Biomaterials*, 105(3), pp. 616-627.
- Zhang, X., Lies, B., Lyu, H. & Qin, H., 2019. In-situ monitoring of electrohydrodynamic inkjet printing via scalar diffraction for printed droplets. *Journal of Manufacturing Systems*, 53, pp. 1-10.

CHAPTER 8. GENERAL CONCLUSION

General Conclusion

This dissertation investigates the development of new material and control process for electrohydrodynamic inkjet manufacturing. This study individually discussed in five different parts: design to fabricate/characterize biomedical devices; develop and e-jet print new tungsten nanoink material for shielding massive radiation; monitor the e-jet printing process by machine vision; monitor the printed pattern's dimension; and establish a statistical model to predict the dimension based on printing parameters.

In Chapter 3, an approach has been developed to fabricate and characterize the silver nanoink printed biomarker. It is challenging to fabricate flexible patterns as a biomarker on various substrates for image diagnosis in the biomedical area. In this study, the silver nanoink was used to fabricate micro/nano-scale patterns such as the barcode. The X-ray characteristics of silver nanoink printed structures were studied and compared with commercial bulk silver. E-jet printing has been demonstrated to use silver nanoink material to print on flexible and bio-based substrates with a micro/nano-scale resolution. E-jet printing has enormous potential to provide biomedical applications by its direct-writing, low-cost, and high-resolution characteristics.

In Chapter 4, a new method to develop tungsten nanoink and e-jet print microstructures for shielding radiation in aerospace were presented. It is a problem to fabricate low-cost, low-weight, and flexible microstructures to protect critical electronics from damage by massive radiation in the spaceship. Tungsten material could be an ideal option to resolve this challenge. However, it is challenging to machine the bulk tungsten into the desired shape. The tungsten nanoink was proposed in this study for e-jet printing such structures in a highly controlled manner. Bulk tungsten was used to calibrate the X-ray characterization of tungsten nanoink. The

X-ray shielding performance of tungsten nanoink microstructures was excellent compared to bulk tungsten under the same thickness and radiation condition. This study resolved the aerospace's radiation challenge by providing a synthesized material and e-jet printing delicate protective shielding structures in a microscale resolution.

In Chapter 5, a machine vision monitoring system was proposed to observe the filament during the e-jet printing process. Random defects could happen during the e-jet printing process. The filament exists between the capillary glass nozzle tip and the conductive substrate. The filament dimension is supposed to be maintained at a specific size under the same printing parameters unless an abnormal situation happens. This study aims to collect and measure the filament's diameter in real-time to avoid possible defects during the e-jet fabrication process. Different modes of filament formation situation were studied. During the printing process, the filament's captured images were sent back to the central computer for image processing and calculation. Once an abnormal situation is detected, the e-jet printing system will input the new control signal to reverse the trend.

In Chapter 6, a laser scalar in-situ monitoring system for e-jet printing was discussed. Previously it was challenging to measure the dimension of e-jet printed patterns during the fabrication process. The printed samples will need to be removed from the substrate for measurement purposes. Thus it is impossible to find the defects or variation of the dimension during the e-jet printing process. This study proposed a laser scalar system to monitor and record images during the e-jet printing process. An image analysis algorithm was developed to calculate the dimension information of printed filament during the printing process. This new proposed approach could help detect dimension variation during the e-jet printing process with reduced labor effort, adequate accuracy, and high reliability.

In Chapter 7, a statistical model was proposed to predict the e-jet printed sample's dimension based on various printing parameters. However, there are promising futures of applying e-jet printing to address the challenge in the aerospace, biomedical, and electronic areas with the assistance of in-situ monitoring systems. But how does the e-jet printing system reverse the trend once a variation of the dimension is detected during the printing process remains a problem. This research has conducted a full factorial experiment considering many control printing parameters to predict the dimension by proposing a statistical model. In the proposed method, the dimension of printed patterns could be predicted based on input printing parameters. This study has proposed another aspect to control and predict the printed sample's dimension by establishing a statistical model. This research could contribute to the building of a closed-loop control system by providing the relationship between the printing parameters and dimension.

In summary, this dissertation has studied the new material development and process control for the e-jet printing manufacturing approach. E-jet printing has presented the enormous potential to be applied in the biomedical, aerospace, and electronics industries. This study has discussed using e-jet printing to address challenge in the fabrication of flexible biomarkers for image diagnosis and the challenge in manufacturing extremely low weight, high-resolution tungsten microstructures for shielding massive X-ray from critical electronics in aerospace. The in-situ monitoring systems were proposed in this study to measure the filament dimension and printed pattern's size in real-time. The exploration of using statistical methods to predict the dimension based on printing parameters was presented. This research could support developing a reliable, low-cost, automatic, and high accurate e-jet printing system in broader areas. The e-jet printing system's digitalization based on these studies could contribute to establishing the next-generation digital twin e-jet printing system.

Future Work

E-jet printing is a high-resolution, low-cost, and flexible micro/nanomanufacturing approach. It was presented as a critical tool to address the challenge in aerospace, biomedical, and electronics in this study. However, there are still many other problems in the medical areas that remain to be resolved. Now high-resolution patterns were mostly e-jet printed on flat and reflective substrates such as glass substrate in this field. Bio-substrate could not be reflective. Thus, it is not easy to control the capillary nozzle close to the substrate to fabricate high accuracy. For example, uneven substrate e-jet printing such as cloth material to develop different wearable devices for the human health industry is still challenging. E-jet printing is controlled by g-code based coordinate system, and the tool path planning could be an exciting research topic.

This study has envisioned the application of tungsten nanoink material to address the challenge in aerospace. Tungsten ink was synthesized to print microstructures for shielding the radiation in aerospace. The ink was used to fabricate 2D novel patterns to shield and protect the electronics. However, the fabrication of complex 3D microstructures still needs to be demonstrated. There are challenges such as the evaporation rate of the solvent material in tungsten nanoink. This question's possible solution could be a proposal of additional material in the nanoink or replacing the substrate with a temperature-controlled substrate for removing extra solvent material.

The in-situ monitoring system could observe abnormal printing conditions by checking the variation of filament dimension and printed pattern's size. Although the printing process could be monitored, the digital twin system will be required to provide quality control and nondestructive evaluation to enable the high-quality e-jet printing process. The collected image data and calculated dimension information could be combined with each deposited ink dot's coordinate information to reconstruct the 3D model of printed patterns. Finally, it could enhance

the reliability and automation of the e-jet printing approach. The proposed statistical model in this dissertation has contributed to predicting the dimension of fabricated patterns. However, both hardware subsystems and statistical methods could be optimized to predict the printed pattern's dimension. In hardware subsystems, the electrode could be redesigned as a parallel electrode to enable a uniform electrical field in the control system. Meanwhile, the simulation of e-jet printing could also predict the dimension based on the electrohydrodynamic mechanism's physical essence. Future research could focus on predicting the printed pattern's dimension considering both the finite element and machine learning methods under solid theory and modern statistical tools.

In summary, e-jet printing will be developed as an automated micro/nano-scale manufacturing process to target challenges in aerospace, biomedical, and electronics. This technique will be further recognized based on developing new materials, process control methods, hardware systems, and software control systems. It will combine other micro/nanomanufacturing methods such as laser drilling as a hybrid micro/nano-scale approach in the next 5-10 years. There will be numerous opportunities in the biomedical interdisciplinary research areas related to micro/nano-scale e-jet printing. I am motivated and interested in working in the academic area. Thus, my career plan would align with my understanding of this area. I will start to work on addressing challenges in e-jet printing wearable devices as the starting point. I would continue working in this area and hopefully establish my hybrid manufacturing lab shortly.